DEVELOPMENT OF POLYURETHANE SCAFFOLDS WITH CONTROLLED MECHANICAL STRENGTH AND INNER STRUCTURE AS POTENTIAL CELL/DRUG DELIVERY SYSTEM FOR TISSUE REGENERATION

By

Ruijing Guo

Dissertation

Submitted to the Faculty of the

Graduate School of Vanderbilt University

in partial fulfillment of the requirements

for the Degree of

DOCTOR OF PHILOSOPHY

in

Chemical Engineering

May, 2015

Nashville, Tennessee

Approved:

Professor Scott A. Guelcher

Professor Jeffrey M. Davidson

Professor Matthew Lang

Professor Jamey Young

DEDICATION

This dissertation is dedicated to my encouraging parents and

supportive friends

ACKNOWLEDGEMENT

I would like to start by gratefully acknowledging the different funding sources that have supported the work presented in this dissertation. This work would not have been possible without the financial support of the Orthopaedic Extremity Trauma Research Program (DOD W81XWH-07-1-0211), the National Institute of Arthritis and Musculoskeletal and Skin Diseases (AR056138), and the Department of Veterans Affairs, Vanderbilt University School of Engineering, the Vanderbilt Center for Bone Biology, and the US Army Institute of Surgical Research.

The first person I would like to express great gratitude to is my research advisor Professor Scott A. Guelcher for his invaluable guidance and support, and for giving me the freedom and autonomy to develop to an independent researcher. Dr. Guelcher's enthusiasm for scientific research inspired my own passion in the field of biomaterials and medical device design not only for the accomplishment of my Ph.D study but toward my future career. I want to acknowledge the help I have received from my committee members over the past years: Dr. Jamey Young, Dr. Matthew Lang, and Dr. Jeffrey Davidson. I would like to express my gratitude to their valuable advice and support.

I would like to thank the advisors of all the collaborating labs for their kind support: Dr. Julie Sterling at the Bone Center, Dr. Craig Duvall at Biomedical Department, and Dr. Joseph Wenke at Institute of Surgical Research. I also want to thank all my lab mates and collaborators for their help in my research and the active and energetic research environment they create. And finally, I want to thank my family and all the friends, who support me physically and mentally in every way.

TABLE OF CONTENTS

LIST OF TABLES

TABEL

LIST OF FIGURES

FIGURE

CHAPTER 1

INTRODUCTION

Cell therapy, which is a different therapeutic strategy compared to traditional medical treatment, has been rapidly developing recently. It comprises the transplantation of autologous or allogeneic cells through local delivery or systemic infusion to restore the viability or function of deficient tissues [[1]].For the application of cell therapy in tissue repair, there are generally two concerns: the delivered cell line and the cell carriers. The ability to regenerate tissues in their most robust form is not common for mammalian species. Fibrotic reactions are usually accompanied with tissue repair and result in the production of a scar [[2]]. However, mammalian tissues from the MRL mouse have been proven to have a profound capacity for regeneration without scarring [2] [[3]], indicating the possibility to fully restore dysfunctional tissues. Therefore, regenerative cells such as mesenchymal stem cells are considered to be a potential solution for cell therapy for tissue repair. However, introducing cells directly into the body will cause large-scale death and loss of control over the fate of the transplanted cells, as well as the migration of cells from the injection site (Fig. 1.1A) [[4]]. Therefore, for the application of cell therapy in tissue repair, there is a compelling need for the development of suitable cell carriers that function as synthetic analogs of the extracelluar matrix (ECM) and provide a substrate for transplanted cell adhesion, control the localization of the cells *in vivo*, and serve as a template for the formation of new tissue masses from the combination of transplanted cells and interfacing host cells [4] as is shown in Fig 1.1B.

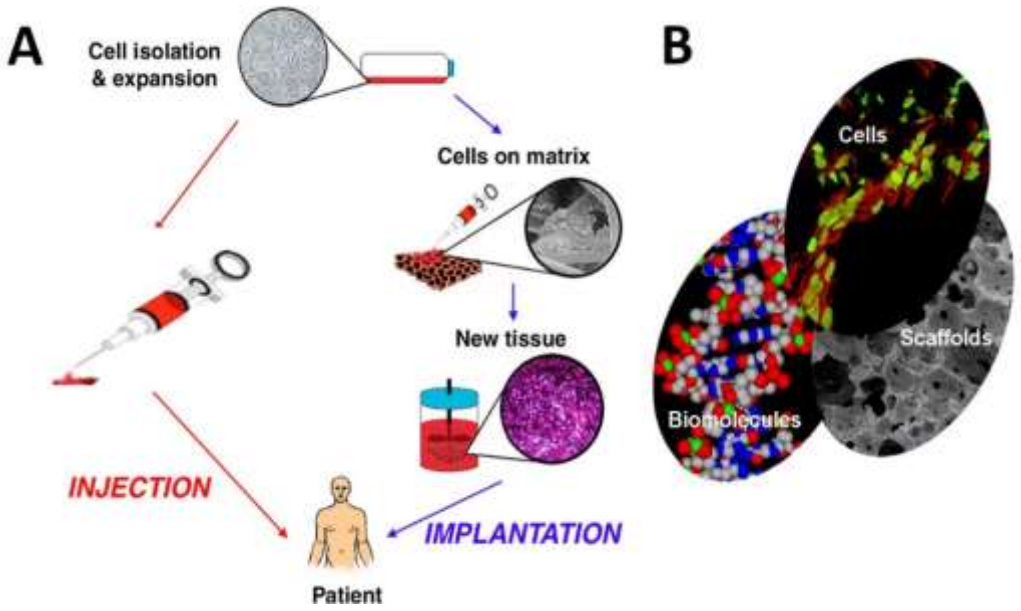

Figure 1.1 A. Current strategies for cell transplantation[4]; B. Conceptual designing of cell therapy by tissue engineering

Scaffolds have been widely applied in wound regeneration studies before the concept of cell delivery . In order to temporarily replace the damaged ECM[5], synthetic scaffolds were developed to create a suitable physiological environment and biological microenvironment for repair of damaged tissues due to trauma, disease, or other injury[6]. Scaffolds have been widely applied for bone, cartilage, and skin regeneration, and have also be used as vehicles for the controlled delivery of bioactive molecules, such as growth factors, proteins and DNA[7],[8],[9]. To better restore the dysfunctional tissues, the design of scaffolds for synthetic ECM application is important in tissue regeneration, as the ingrowth of host cells and their ultimate fate are influenced by the properties of the scaffolds [6]. After decades of study for the development of scaffolds, several key criteria have been identified: (1) promote cell-material interactions, cell adhesion, and ECM deposition; (2) support transport of gases, nutrients, and biomolecules to enable cell growth; (3) be non-toxic to

the host tissues and provoke a minimal degree of inflammation *in vivo*; and (4) biodegrade at a controlled rate to breakdown products that can be cleared *in vivo* [7] [10]. Generally, two major categories of biomaterials have been used for scaffold formation: natural polymeric materials, such as collagens[11], and synthetic polymeric materials, such as PLGA[12]. Compared to the natural biomaterials, synthetic polymeric scaffolds can be fabricated at large scales, and the physical properties as well as degradation time can be controlled [12].

Among the synthetic polymeric materials, lysine-derived polyurethane scaffolds, which are porous, biodegradable, and biocompatible, have been reported to support the migration of cells and ingrowth of new tissue *in vitro* and in subcutaneous, cardiovascular, and bone models and degrade to non-toxic breakdown products [[13]] [[14]]. Moreover, polyurethane scaffolds have also been shown to support cell differentiation under conditioned medium *in vitro* and *in vivo*, indicating similar cell-matrix interaction between the scaffold and seeded cells [[15]] [[16]] [[17]]. Furthermore, the physical and mechanical properties such as pore size, porosity, modulus, and strength can be tuned by varying the structure of the polymer. Therefore, polyurethanes can function as a polymer carrier with adjustable characteristics for use as a cell delivery system. The influence of physical properties of polyurethane scaffolds on cell growth and engraftment in the wounded sites must be clarified by understanding the molecular mechanisms mediating cell-biomaterial interactions, which will enable greater control over the wound healing process by modifying the properties of the polyurethane scaffolds.

Table 1.1 Characteristics of commonly used polymeric biomaterials for tissue regenerations (modified from Ref. [[18]])

Polymers		Biocompatibility	Biodegradability	Application
naturally-derived polymers	Collagen	Minimal cytotoxicity, Mild foreign body reaction, Minimal inflammation	Bulk, Controllable	Skin; cartilage; bone; ligaments; tendons; vessels; nerves; bladder; liver
	Hyaluronic acid	Minimal foreign body reaction, No inflammation	Bulk, 1 h to 1 month	Skin; cartilage; bone; ligaments; nerves; vessels; liver
	Chitosan	Minimal foreign body reaction, No inflammation	Bulk, 3 days to 6 months	Skin; cartilage; bone; nerves; vessels; liver; pancreas
synthetic polymers	Poly(lactic acid)	Minimal cytotoxicity, Mild foreign body reaction, Minimal inflammation	Bulk, 24 months	Skin; cartilage; bone ligaments; tendons; vessels; nerves; bladder; liver
	Poly(lactic acid-co-glycolic acid)	Minimal cytotoxicity, Mild foreign body reaction, Minimal inflammation	Bulk, 1–6 months	Skin; cartilage; bone ligaments; tendons; vessels; nerves; bladder; liver
	Poly(caprolactone)	Minimal cytotoxicity, Mild foreign body reaction, Minimal inflammation	Bulk, 3 years	Skin; cartilage; bone; ligaments; tendons; vessels; nerves

The goal of this dissertation was to develop a cell carrier system with tunable physical properties for mesenchymal stem cell delivery to restore tissue function by supplying the multiple factors required for healing from the regenerative stem cells. Two-component polyurethanes were used as the cell carrier and scaffold to support peripheral tissue infiltration into the defect sites. Polyurethane scaffolds can provide an environment as an extracellular matrix to support cellular

infiltration and tissue ingrowth, and thus the regenerative mesenchymal stem cells will grow on the implanted polyurethane scaffolds to form granulation tissue, secrete growth factors, and promote the ingrowth of cells from peripheral tissue. Additionally, in order to control cell fate with the polyurethane cell carrier, scaffolds with precisely controlled physical properties were generated by a 3D printing technique and were evaluated both *in vitro* and *in vivo* to fully characterize cell-polyurethane interactions. The detailed rationale and study design will be further described in Chapter 2.

Chapter 3 describes the development of the injectable and settable polyurethane cell delivery system and its application in rat excisional wound repair. The injectable lysine-derived two-component polyurethanes have been previously utilized to support cutaneous wound healing by slowing down the spontaneous fibrosis process after injury occurs[19] or further improved healing by delivering growth factors such as PDGF[14]. Yet, as a highly reactive system, its application in cell therapy with minimally invasive surgery has been limited. In this chapter, the employment of a protective barrier of alginate hydrogel is described to temporarily protect the transplanted mesenchymal stem cells. In order to ensure both short term and long term cell survivability, the optimization of scaffold's porosity, mechanical property, and setting time is reported and the proof-of-concept *in vivo* study is presented.

Further, in order to control cell fate with the polyurethane cell carrier, the development of a polyurethane scaffold with precisely controlled topological and mechanical properties is described in Chapter 4. In order to study cell- polyurethane interaction for long term, instead of utilizing lysine-derived polyurethane, HDI trimer was used to synthesize polyurethane scaffolds as its

hydrolytic degradation is negligible during the study time period[13]. The mechanical properties of polyurethane are modified by changing the crosslink density, which is easily achieved by controlling the chain length of polyol and isocyanate in the reaction [[20]]. In order to generate controllable physical properties, including pore size and porosity and elastic modulus, the application of a sacrificial template combining with the fast developing 3D printing technique and melt cast method previously developed in our lab is also described in this chapter. To prove its influence on cell fate control, the effects of scaffold pore size and elastic modulus on osteogenesis of mesenchymal stem cells were investigated.

Chapter 5 presents the *in vivo* evaluation of the 3D polyurethane scaffolds with controlled physical and mechanical properties on wound healing. Previously studies have compared injectable lysine-derived polyurethane scaffolds with different elastic moduli in a porcine excisional wound model and showed the importance of scaffold modulus on wound repair. Yet, due to the fast degradation of the injectable formulation, the biomolecular mechanism of mechanical strength could not be isolated and remained unclear. Thus polyurethane scaffolds with negligible degradation rate during wound healing with moduli ranging from 100 kPa to 100 MPa were designed and synthesized with the indirect 3D printing as described in Chapter 4 and evaluated in a rat subcutaneous wound model. The comparison of expression of growth factors, macrophage polarization, and mechanotransduction in wound fibroblasts is also discussed in this chapter.

Considering the importance of substrate rigidity on mesenchymal stem cell osteoblastic differentiation on rigid scaffolds (>10 MPa) as described in Chapter 4, Chapter 6 continues to

investigate the mechanism of osteogenesis. In addition to the 3D polyurethane scaffolds, a 2D polyurethane cell culture system with the same substrate modulus was employed in this section. It has been reported to be able to mimic the physiologically relevant rigidity in the bone microenvironment and been used to observe the expression of osteolytic factors in cancer cells that are able to metastasize to bone[21]. The involvement of both integrin and BMP receptors is described in this chapter. Although the conventional mechanotransduction kinase signaling pathways are characterized to be identical, the failure to establish a correlation between the well-known FAK phosphorylated activation with substrate rigidity at this high range leads to the observation of direct physical interactions between the two receptors. The relationship between integrin and BMP receptors was screened and confirmed by both immunoprecipitation and a novel Förster resonance energy transfer (FRET) experiment utilizing mesenchymal stem cells cultured on polyurethane substrates with varying modulus. The cumulative effects of integrin-BMP signaling on osteoblastic differentiation will also be discussed in this chapter and indicates the possibility to reduce the delivered dose of growth factors (such as BMP2) by optimizing the mechanical properties of scaffolds to eliminate complications.

Finally, to conclude, Chapter 7 summarizes the main results of this dissertation and Chapter 8 presents the discussion and suggestions for future work. Overall, this dissertation presents the development of polyurethane scaffolds with tunable physical properties for the wide application in tissue regeneration from soft tissue to weight bearing bone.

Reference

[1] Chunmeng Shi, Ying, Zhu, Yongping Su, Tianmin Cheng; Stem cells and their applications in skin-cell therapy; Trends in Biotechnology, Vol. 24 No. 1, January 2006.
[2] Anthony D. Metcalfe, Mark W. J. Ferguson; Tissue engineering of replacement skin: the crossroads of biomaterials, wound healing, embryonic development, stem cells and regeneration; Journal of the royal society interface (2007) 4, 413-437.
[3] Ellen Heber-Katz, John Leferovich, Khamilia Bedelbaeva, Dmitri Gourevitch, Lise Clark; The scarless heart and the MRL mouse; The Royal Society online 8 April 2004.
[4] David J. Mooney, Herman Vandenburgh; Cell Delivery Mechanisms for Tissue Repair; Cell Stem Cell 2, March 2008.
[5] Aldo Leal-Egaña , Ar ánzazu D áz-Cuenca , Aldo R. Boccaccini, Tuning of Cell–Biomaterial Anchorage for Tissue Regeneration, Adv. Mater. 2013, 25, 4049–4057
[6] Kim, B. S., Park, I. K., Hoshiba, T., Jiang, H. L., Choi, Y. J., Akaike, T., Cho, C. S. (2011). Design of artificial extracellular matrices for tissue engineering. Progress in Polymer Science, 36(2), 238-268.
[7] Dhandayuthapani, B., Yoshida, Y., Maekawa, T., Kumar, D. S. (2011). Polymeric scaffolds in tissue engineering application: a review. *International Journal of Polymer Science*, *2011*.
[8] Lee, K., Silva, E. A., Mooney, D. J. (2011). Growth factor delivery-based tissue engineering: general approaches and a review of recent developments. *Journal of The Royal Society Interface*, *8*(55), 153-170.
[9] Kretlow, J. D., Klouda, L., Mikos, A. G. (2007). Injectable matrices and scaffolds for drug delivery in tissue engineering. *Advanced drug delivery reviews*, *59*(4), 263-273.
[10] Langer, R., Tirrell, D. A. (2004). Designing materials for biology and medicine. Nature, 428(6982).
[11] Rosso, F., Marino, G., Giordano, A., Barbarisi, M., Parmeggiani, D., & Barbarisi, A. (2005)
[12] Mano J F, Silva G A, Azevedo H S, et al. Natural origin biodegradable systems in tissue engineering and regenerative medicine: present status and some moving trends [J]. Journal of the Royal Society Interface, 2007, 4(17): 999-1030.
[13] Andrea E. Hafeman, Bing Li, Toshitaka Yoshii, Katarzyna Zienkiewicz, Jeffrey M. Davidson, and Scott A. Guelcher; Injectable Biodegradable Polyurethane Scaffolds with Release of Platelet-derived Growth Factor for Tissue Repair and Regeneration; Pharmaceutical Research, Vol. 25, No. 10, October 2008.
[14] Bing Li, Jeffrey M. Davidson, Scott A. Guelcher; The effect of the local delivery of platelet-derived growth factor from reactive two-component polyurethane scaffolds on the healing in rat skin excisional wounds; Biomaterials 30 (2009) 3486-3494.
[15] M. Zanetta, N. Quirici, F. Demarosi, M.C. Tanzi, L. Rimondini, S. Fare; Ability of polyurethane foams to support cell proliferation and the differentiation of MSCs into osteoblasts; Acta Biomaterialia 5 (2009) 1126–1136.
[16] Carsten Schlickewei, Sophie Verrier, Sebastian Lippross, Simon Pearce, Mauro Alini, Sylwester Gogolewski; Interaction of Sheep Bone Marrow Stromal Cells With Biodegradable Polyurethane Bone Substitutes; Macromol. Symp. 2007, 253, 162–171.
[17] Bj ¨orn Carlberg, Mathilda Zetterstr ¨om Axell, Ulf Nannmark, Johan Liu, and H Georg Kuhn; Electrospun polyurethane scaffolds for proliferation and neuronal differentiation of human embryonic stem cells; Biomed. Mater. 4 (2009) 045004 (7pp).
[18] Moroni, L., De Wijn, J. R., Van Blitterswijk, C. A. (2008). Integrating novel technologies to

fabricate smart scaffolds. *Journal of Biomaterials Science, Polymer Edition*, *19*(5), 543-572.
[19] Adolph, E. J., Hafeman, A. E., Davidson, J. M., Nanney, L. B., Guelcher, S. A. (2012). Injectable polyurethane composite scaffolds delay wound contraction and support cellular infiltration and remodeling in rat excisional wounds. *Journal of Biomedical Materials Research Part A*, *100*(2), 450-461.
[20] Scott A. Guelcher; Biodegradable Polyurethanes: Synthesis and Applications in Regenerative Medicine; TISSUE ENGINEERING: Part B Volume 14, Number 1, (2008).
[21] Ruppender, N. S., Merkel, A. R., Martin, T. J., Mundy, G. R., Sterling, J. A., Guelcher, S. A. (2010). Matrix rigidity induces osteolytic gene expression of metastatic breast cancer cells. *PLoS One*, *5*(11), e15451.

CHAPTER 2

BACKGROUND

Tissue engineering for tissue regeneration

The ability to regenerate tissues a most robust form is not common for mammalian species. Fibrotic reactions are usually accompanied with tissue repair and result in the production of a scar [[1]]. Thus, researchers in tissue engineering have been investigating regenerative medicine approaches to restore the lost or dysfunctional tissues or organs for decades. For application of regenerative medicine, there are three general components: harvesting of cells from donor tissue, particularly precursor or stem cells from embryos or adults, or biomolecules that promote growth and/or differentiation into the desired cell type combined with supportive biomaterial scaffolds that support cell attachment as well as proliferation and/or differentiation (Figure 2.1) [[2]]. As an increasing number of growth factors have been investigated, the choice of biomolecules used for regenerative medicine has been broadened. Moreover, regenerative mammalian cells and more potentially differentiable cells that are able to self-renew have also been discovered. Therefore, with the goal of regenerating tissues or organs to restore normal functions, one important strategy of tissue engineering is to replace the lost tissues with polymeric scaffolds which contain specialized biomolecules or populations of living cells[[3]] [[4]]. For the successful application of scaffolds in tissue engineering, different desired properties have been proposed for cell/drug delivery systems (Table 2.1).

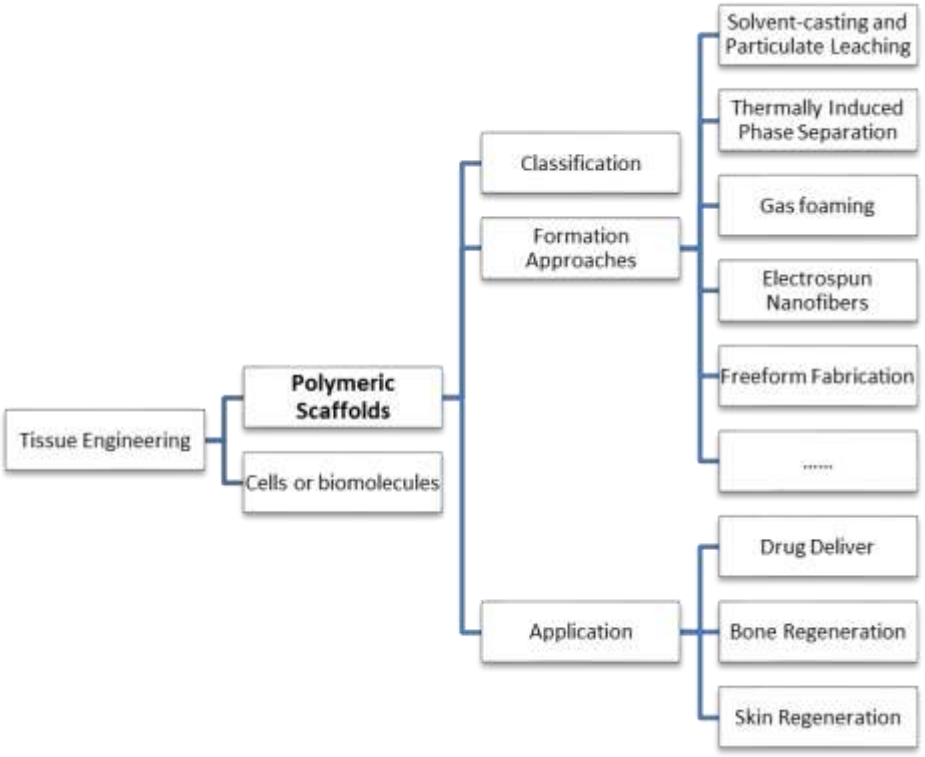

Figure 0.1 Polymeric scaffold for biomedical application

Polymeric scaffolds, mostly natural derived polymers, have been clinically applied for skin/cutaneous wound repair. After skin injuries, the three-dimensional scaffolds can cover the wound and support proliferation of dermal fibroblasts and keratinocytes for skin tissue engineering[5]. Multiple natural polymers have been commercialized for skin wound repair, such as collagen, chitosan, fibrin, elastin, gelatin, and hyaluronic acid[5]. However, their relatively low mechanical strength, shrinkage/contraction, and risks of immunological rejection have limited their broad application[6]. Therefore, due to the controllable desired properties of synthetic polymeric scaffolds (as shown in the table above), the application of synthetic polymers or blending synthetic polymers with natural polymers may be favorable when controllable fabrication is required[7].

Table 0.1 Desired properties of scaffolds for tissue engineering (Modified from Ref. [[8]])

Application	Desired Properties
Scaffolds for cell delivery	Mechanical properties that are sufficient to shield cells from tensile forces without inhibiting biomechanical cues
	Desired volume, shape, and mechanical strength
	Acceptable biocompatibility
	A highly porous and well-interconnected open pore structure to allow high cell seeding density and tissue in-growth
	Bioadsorption at predetermined time period
	Biocompatible chemical compositions and their degradation products, causing minimal immune or inflammatory responses
	Physical structure to support cell adhesion and proliferation, facilitating cell–cell contact and cell migration
Scaffolds for drug delivery	Homogenous drug dispersion throughout the scaffold
	Ability to release the drug at a predetermined rate
	Drug binding affinity that is sufficiently low to allow the drug released to be stable when incorporated in the scaffold at a physiological temperature
	Stable physical dimension, chemical structure, and biological activity over a prolonged period of time

Although bone tissue is subjected to continuous remodeling and thus possesses regeneration capacity in response to injury[9], unfavorable local conditions and extensive bone loss will result when bone repair fails[10]. Moreover, synthetic ECM in bone repair is not only important to serve as the template for cell interactions and structural support for the newly formed tissue, but it also must possess mechanical properties similar to those of host bone, biocompatibility, biodegradability at a rate commensurate with remodeling, porosity that allows migration and proliferation of osteoblasts and mesenchymal cells, adequate transport properties, and

vascularization[11]. Metallic and ceramic materials have been widely applied for bone repair. However, drawbacks such as poor tissue adherence, slow of degradation, and toxicity[12],[13] have driven the exploration for other bone replacement materials. Among the scaffolds that been developed, synthetic polymers have been extensively evaluated for bone defects regeneration due to the advantages of the highly reproducible and tunable control over porosity, mechanical properties, surface chemistry and degradation time[14] [15], as well as their higher mechanical strength over naturally derived polymers. As shown in Fig. 2.2, ,cells facilitating bone tissue regeneration can be cultured on these biomaterials for days to weeks to colonize and even pre-differentiate prior implantation to the injury site to obtain optimized benefit for bone repair.

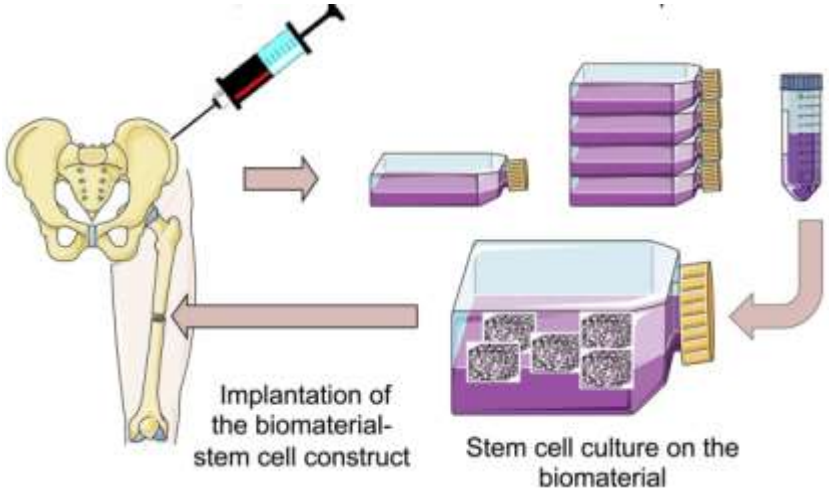

Figure 0.2 Scheme of mesenchymal stem cell culture on biomaterials prior to implantation

Materials and methods for polymeric scaffolding

Considering the sources of polymers mentioned above, polymeric scaffolds can be divided into two categories: natural and synthetic. The advantages of selecting the natural polymeric scaffolds are obvious. They are biocompatible, relatively abundant, and easy to process. Moreover,

most natural polymers will ultimately be broken down into carbon dioxide and water, which are generally nontoxic [[16]] and readily cleared from the body. However, since the structural properties of the scaffolds, such as pore size and its distribution, pore shape, pore interconnectivity, and overall porosity of scaffolds, play important roles in all processes involved in tissue genesis, accurate control over those properties is mandatory for the success of tissue engineering approach [[17]]. In contrast to natural polymeric scaffolds, both the structural properties and mechanical properties can be controlled and designed for synthetic polymers. Since synthetic polymers exhibit predictable and reproducible physical, chemical and degradation properties and their shapes and sizes are designable[18] as mentioned above, multiple methods for polymer scaffold synthesis have been developed.

Solvent-casting and particulate leaching

Solvent casting and particulate leaching is a simple method for fabrication of porous scaffolds for tissue engineering and is convenient and widely used [2] [[19]]. This method was first described in 1993 and 1994 by using ground sodium chloride as a porogen to demonstrate that biodegradable polymers could be processed into various porous materials [17]. The process comprises mixing water-soluble salt particles with a biodegradable polymer solution and then casting the mixture into a mold of desired shape, followed by removing the solvent by evaporation or lyophilization [17] [19]. Subsequently, the porous structure of the polymeric scaffold can be obtained after the salt particles are leached out (Figure 2.2). Besides various soluble salt particles, paraffin microspheres, polysaccharide microspheres, emulsion particles, and other kinds of soluble particles have been

used as porogens. Moreover, by regulating the amount and size of the porogen, the particulate leaching method can easily control pore morphology, overall porosity, and pore size of the scaffolds (Figure 2.3) [2].

However, there are also many issues associated with the porogen leaching process. First of all, it requires pressure to form the scaffold during the porogen leaching period and a relatively long period of soaking in solvent is required to leach the entire porogen particle population [2]. Secondly, since the pore morphology and porosity of the scaffolds are totally dependent on porogen particles, non-uniform distribution of the porogen and wide distribution of porogen size will affect properties of the scaffolds. What is more, since this method needs post process after the formation of the scaffolds, it decreases the injectability of the polymer. And also, the residual solvent and porogen by products are potentially local toxic [[20]].

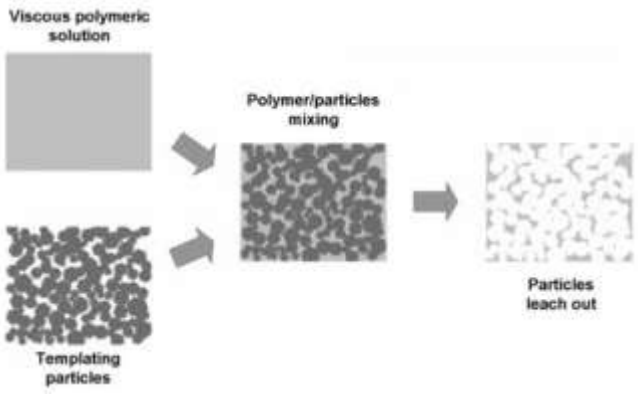

Figure 0.3 Representation of basic steps in processing method of solvent casting and particulate leaching [17]

Thus, accurate control over the process is required. Inhomogeneous scaffolds can be avoided by controlling the quantity and viscosity of the polymer used in fabrication. Accurate control over crystallinity during the drying stage is also necessary to achieve scaffolds with a reproducible

degree of crystallinity [17]. Recently, many studies have aimed to overcome limitations of this method, and it should be noted that porogen leaching can be coupled with many other processing methods to develop scaffolds with desired properties [17].

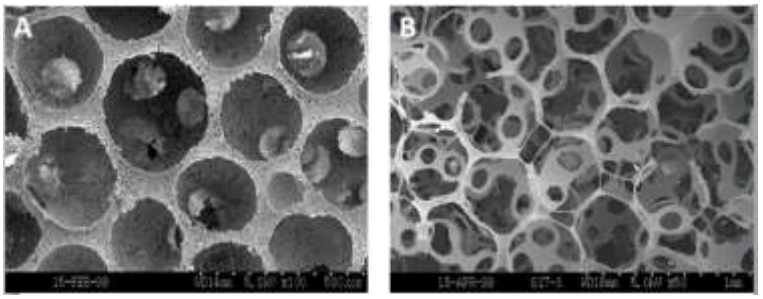

Figure 0.4 SEM images of poly (α-hydroxy acids) scaffolds. A, PLLA foams pepared with paraffin spheres with a size range of 250-350μm; B, PLGA foams prepared with paraffin spheres with a size range of 420-500μm [21].

Thermally Induced Phase Separation

In the past years, thermally-induced phase separation has been progressively adopted from synthetic membranes for the scaffold production in the field of tissue engineering and the fabrication of microspheres loaded with biological or pharmaceutical agents in drug delivery applications [17]. The phase separation technique is based on thermodynamic demixing. It is achieved either by cooling the biomaterial solution to a point below the bimodal solubility curve or exposure of the biomaterial solution to an immiscible solvent [2]. Subsequent removal of the solidified solvent-rich phase by sublimation generates the porous polymer scaffold [19]. It is also possible to form scaffolds by using a solid-liquid phase separation technique, while the mechanism is more complex than the behavior of binary systems [17].

During the demixing process, phase separation of polymer solutions leads to a polymer-rich

and a polymer-lean phase, according to a bimodal demixing or a spinodal decomposition, which are characterized by nucleation and growth inside the metastable region or spinodal decomposition inside the spinodal region (Figure 2.4) [[22]]. Therefore, considering the mechanism of phase separation of polymer solutions, the thermodynamics of phase separation plays a crucial role in determining the final structure: nucleation and growth yields a porous structure with poorly interconnected cells; and spinodal decomposition gives rise to an interconnected network [22]. The morphologies of scaffolds made from thermally induced phase separation can be varied with different phase separation mechanisms by adjusting the polymer concentration, using a different solvent, or varying the cooling rate [[23]]. Thus, it is possible to control the fiber density and porosity of the fibrous matrix by adjusting these processing parameters, resulting in a highly reproducible scaffold [17]. However, while gelation can create physical cross-links to improve mechanical properties of the scaffold, pore size generated by this method is generally less than 100 microns, suggesting its limited application in tissue regeneration [17].

Gas foaming

Both solvent-casting and particulate leaching to thermally-induced phase separation, utilize organic solvents. However, the residual solvent or porogen in the scaffolds may be harmful to adherent cells, protein growth factors, and nearby tissues [[24]]. Thus, in order to overcome this shortcoming, an approach without the use of organic solvents has been developed. In this approach, a gas or supercritical fluid (usually carbon dioxide or nitrogen) is used similarly to the porogen in particulate leaching [17] [[25]]. During the process, thermodynamic instability is created by rapidly

releasing the gases from the polymer system, and thus the nucleation and growth of gas bubbles will be performed inside the material (Figure 2.5) [19]. Besides "leaching out" the gases by physically regulating pressure or temperature, it is also possible to fabricate the scaffold with a gas-generating chemical reaction [[26]]. By selecting appropriate operating conditions (such as the blowing agent type and concentration, foaming temperature and pressure drop rate), the gas foaming technique allows a fine control over the extension of the porous network of the scaffolds [17].

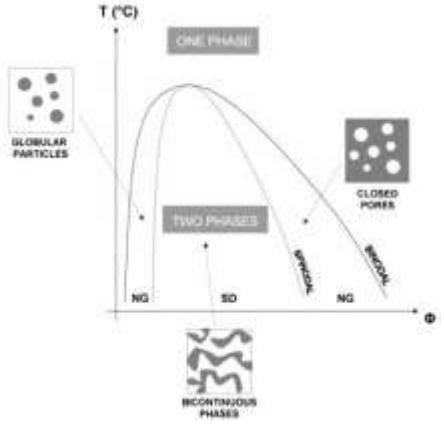

Figure 0.5 Schematic representation of binary phase diagram of polymer/solvent binary system showing expected morphological variations from liquid-liquid phase separation [17]

Since the gas foaming method eliminates organic solvents and can be processed at mild temperature, the scaffolds gain enhanced biocompatibility ease of use with bioactive molecules [25]. However, although pore size and porosity of the scaffolds prepared by gas foaming approach can be adjusted by controlling the operating conditions, the formation of highly interconnected scaffolds might be impaired by a combination of rheological and processing limitations which restrict the completion of pore opening during foaming and form a closed external skin [17] [24]. As

interconnected pores are necessary for scaffolds to support cell growth or infiltration, more studies are done to open up internal pores made from gas foaming method by combining other fabrication methods.

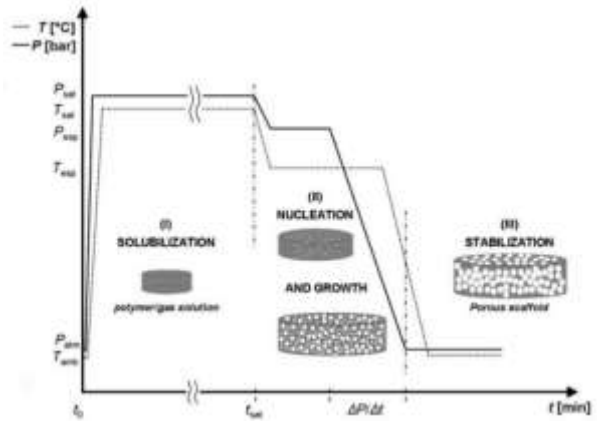

Figure 0.6 Schematic diagram of temporal evolution of pressure induced phase separation process and resulting physical state of system [17]

3-dimensional printing technology

Since the invention of 3D printing technology, researchers have been investigating its application in biomaterials printing for tissue engineering to take advantage of the precise control over 3D structure. 3D printing offers the advantage of control over scaffold geometry, pore size, and pore interconnectivity[27]. To design scaffolds recapitulating the natural ECM, the chemical composition, pore size, pore volume and mechanical properties are critical parameters for scaffold performance[27,28]. The application of 3D printing allows precise computer control over the microstructure by printing with different parameters[29]. With the aid of computer-assisted design, the 3D structure is sliced to 2D files and the fabrication materials are deposited layer by layer for each sliced 2D file[30]. The scheme for 3D printing technique is shown in Fig. 2.6. However, despite

with the benefits of 3D printing for scaffold design, the number of polymers that can be directly printed is still limited, and modification of specific materials for 3D printing is challenging and expensive[29]. To overcome this limitation, researchers have investigated new 3D printing approaches, such as fabricating scaffolds indirectly from the 3D printed scaffolds by casting the final materials into the printed mold cavity[29].

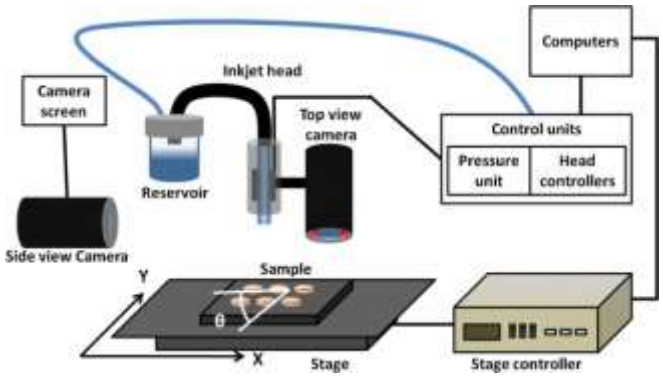

Figure 0.7 Schematic diagram of the 3D printing (3DP) system.[31]

Polyurethane scaffolds as potential cell delivery carrier for tissue regeneration

With the advantages of a wide range of versatility of tailoring their physical properties, blood and tissue compatibility and biodegradation character, polyurethanes remain to be one of the most popular group of biomaterials applied for medical devices [[32]]. Therefore, polyurethane scaffolds have found their wide applications as blood contacting biomaterials, such as vascular grafts, catheters, general purpose tubing, and artificial organs [[33],[34]]. Due to its tunable physical properties including high interconnectivity, cells are able to be directly seeded on the scaffolds and survive in long-term culture *in vitro* [35]. Moreover, it has already been reported that polyurethane scaffolds were able to support cell proliferation and the differentiation of stem cells into different cell lineages, such as osteoblasts [[35]], and neuronal cells [[36]].

At the same time, polyurethane scaffolds have been reported to serve as drug delivery system *in vitro* and *in vivo*[[37]]. Although it has not been reported for the application in cell therapy as a cell delivery system, considering its ability to support cell ingrowth as well as its injectability and ability to cure *in situ* [[38]], which suggests its potential application for minimally invasive therapy, injectable polyurethane scaffold can also be utilized as a polymer carrier for cell delivery. Moreover, physical properties of the synthesized polyurethane scaffolds can be easily regulated by modifying the involved reactants. For polyurethane foams, the porosity, interconnectivity and pore sizes can be controlled by adjusting water component and surfactant in the reaction. In the meanwhile, the mechanical properties can be modified by changing the structures of hard and soft segments, which can be easily achieved by controlling the chain length of polyester triol and (poly/mono) isocyanate in the reaction (Table 2.2) [[39]]. Therefore, injectable polyurethane is a promising carrier for *in situ* cell delivery with the ability to apply minimally invasive therapy.

Table 0.2 Tunable mechanical properties of synthesized polyurethane scaffolds[40]

Polymer	T_g (°C)	T_m (°C)	Modulus (MPa)
BDI/BDA/PCL1250 [36]	−37	A	54
BDI/BDA/PCL2000 [36]	−53	40	78
BDI/Lys/PCL1250 [36]	−40	A	14
BDI/Lys/PCL2000 [36]	−54	45	38
LDI/Phe/PCL530 [38]	−6	A	6.6
LDI/Phe/PCL1250 [38]	−34	43	54
LDI/Phe/PCL2000 [38]	−52	45	82
BDI/BDA/PCL2000 [34]	−57	20	52
HDI/BDA/PCL2000 [34]	−51	22	38
LDI/BDA/PCL2000 [34]	−52	41	40
BDI/BDO.BDI.BDO/PCL2000 [16]	−54	18	70

Sodium alginate hydrogel as protection barrier

Despite the superiority of polyurethane for cell delivery, cells cannot be encapsulated in the scaffolds directly. Reactants of polyurethane are highly hydrophobic without nutrients or dissolved

oxygen, which is not a friendly environment for cell survivability. Thus a protection barrier will be necessary during the process of polyurethane scaffold formation. Alginate, because of its abundance, easy gelling properties, and apparent biocompatibility, has been frequently employed for cell encapsulation to protect cells from the attack of host's immune system [[41]]. Alginates are natural-derived polymers (polysaccharides) isolated from brown algae such as *Laminaria hyperborean*[42]. Moreover, it has been shown that cells encapsulated within the calcium alginate hydrogel retained a high level of cell viability [[43]].

In the meantime, the controllable degradation rate of alginate hydrogel and the non-toxic lysates[44], 42 also contribute to its application as temporary protection barriers. As alginates can be made to hydrolysis via reaction with sodium periodate, their degradation rate can therefore be controlled through partial oxidation[24]. After partially oxidation of alginic acid, the conformation change of urinate residue then generates a hydrolytically labile bond that speeds up the hydrolysis process of alginate hydrogel[45]. Thus, alginate hydrogel is able to be performed as temporary protection of cells from the harmful products during the process of polyurethane formation.

Cell-biomaterials interaction

For the application of tissue engineering, cells either pre-seeded onto the fabricated scaffolds or infiltrated from host tissues will directly have contact with the scaffolding materials, driving the clarification of cell-biomaterials interaction. As an artificial ECM, scaffolds materials must provide informative microenvironments for cells to interpret the biomaterial instructions, as well as to modify cell fate accordingly[46]. Therefore, in order to control cell fate with scaffolds, their

topography, surface chemistry and physical properties are the crucial factors to be precisely controlled[47].

As the elasticity of native tissues varies in a wide range throughout the body, cells will perform differently in response to different surrounding mechanical environment to form tissues performing various functions [[48]]. The potential mechanism is that the elasticity of the underlying matrix will affect the spreading, proliferation, and even differentiation of cells [[49]]. Therefore, studies have been done to clarify the relationship between cell behaviors and mechanical stimulation. Fibroblasts have already been described to preferentially migrate from a soft surface to a stiff one [[50],[51]]. Moreover, it has been reported previously that human mesenchymal stem cells would proliferate faster and differentiate slower with stiff microstructure in 3D matrix [[52]], indicating that the multipotent stem cells are also able to respond to both the static mechanical stimuli and 3D microstructure.

As for the *in vivo* application of biomaterials, inflammatory response following material implantation during wound healing requires thoroughly consideration since macrophages and foreign body giant cells are recruited to the site of injury and play crucial roles for tissue repair and regeneration. Fig 2.7 here shows a brief sequence of the foreign body reaction to biomaterials implantation. The appearance of macrophages initiates and speeds up the wound repair process but yet may also lead to fibrosis and form scars[53]. Since it is the surface chemistry and other physical properties modulating the foreign body reaction following scaffolds implantation, understanding mechanism of foreign body reaction therefore will guide the design of implanted scaffolds[61].

Recently, more and more studies have shown that the controversial effects of macrophages

on wound healing are due to the polarization of macrophages to different phenotypes in response to specific environmental cues[54]. Mimicking the nomenclature of Th1/Th2 polarization, macrophage phenotypes have been described as M1/M2[55] as well while M1 is proinflammatory and M2 is anti-inflammotory. Previous studies have shown a strong correlation between macrophage response to implanted scaffold materials and the outcome of tissue remodeling and suggested different cell populations to the sites of materials induced the M1/M2 responses[56]. However, the direct correlation between the properties of implanted scaffolds and polarization of macrophages is still poorly characterized and requires thoroughly understanding.

Crucial mechanotransduct signaling pathways

Living cells in ECM experience not only biochemical but also diverse biomechanical environment. Previous studies have shown that a mechanical stimuli on cell surface receptors can immediately change the organization of molecular assemblies in the cytoplasm and nucleus in living cells (Fig. 2.8)[57]. Physical forces can be converted into biochemical signals that are then integrated into cellular responses through a process called "mechanotransduction", which is especially crucial in bone repair and regeneration [[58]]. It has been shown that proliferation and differentiation of osteoblasts were enhanced mechanical by the stimulation of specific pathways and genes[59]. At the same time, strain-applied therapies, such as vacuum compression, haven shown clinically efficacious in soft tissue injuries repair[60], indicating the importance of mechanotransduction in cutaneous wound healing as well. However, the detailed mechanism for how the biomechanical signal stimulated intracellular pathways remained unclear. Up to date, there

are several mechanotransduction signaling pathway have been extensively studied.

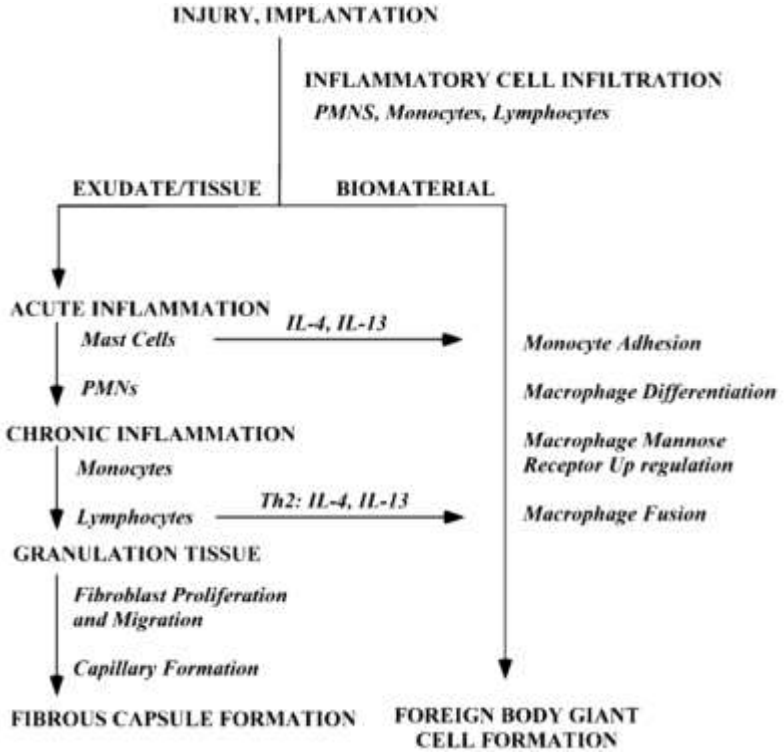

Figure 0.8 Sequence of events involved in inflammatory responses in wound healing[61]

Integrin signaling pathway

Integrin is a family of transmembrane heterodimeric cell surface adhesion receptors that are essential for multicellular life[62]. They act as anchors to connect cells to the ECM and transduce outer signals to the cell through the intracellular proteins that bind the integrin cytoplasmic tail to mediate signaling cascades that impact cell motility, growth, and survival[63]. Although not clearly understood, with the exposure to outer mechanical stimuli, contraction force possibly either triggers integrins increased clustering as a result of increased actin and myosin recruitment and cytoskeletal assembly[64] or alters the conformation of force-sensitive components of focal adhesions to induce binding interactions[65] and therefore kinases such as FAK (focal adhesion kinase), Ras, Rac, Rho, and Src are activated correspondingly to mediate mechanotransduction[66].

Integrin family contains both different α- and β-subunits and their pairings determine ligand specificity and as the α-tails generally have little similarity to one another while most integrin β-tails are conserved, studies have been focused on the mechanism of β-subunits response to stimuli[63].

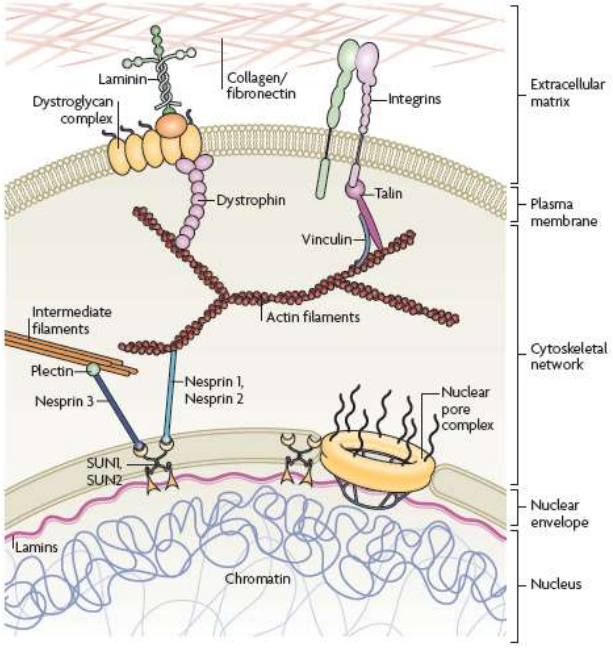

Figure 0.9 Force transmission between the extracellular matrix and the nucleus[67]

Crosstalk between integrin and growth factor pathways

The integrin-mediated cell-ECM interactions has been described to generate an adhesion molecule-integrin-actomyosin complex that can be shifted between signaling states by activation of myosin II or matrix rigidity[68], which can only be applied when the cells were able to displace ECM[69]. However, more and more biomolecular studies have shown that it is several integrin proteins themselves that are required for cells to conduct growth related signaling cascades. In response to underlying mechanical stimuli, the crosstalk between integrins and cells crucial growth factor signaling pathways has been well known but poorly understood for decades. Other than the effects on cell fate from downstream integrin mediated kinases activation as have mentioned above,

the requirement of specific integrin association for growth factor receptors function has been unveiled (Table 2.3).

Table 0.3 Integrin-Mediated Growth Factor Responses (Modified from Ref [[70]])

Growth factor	Integrin	Response
PDGF	$\alpha_v\beta_3$	Proliferation, migration
bFGF	$\alpha_v\beta_3,\ \alpha_5\beta_1$	Angiogenesis, migration
VEGF	$\alpha_v\beta_5$	Angiogenesis
EGF	$\alpha_v\beta_5$	Migration, metastasis
IGF/insulin	$\alpha_v\beta_5$	Migration, metastasis

Among integrin mediated growth factors, the responses of transforming growth factor-β(TGF-β) related signaling pathway has not been clarified up to date, especially the bone development sub-family BMP signaling. Although previous studies have shown that the stem cells or progenitors osteoblastic differentiation is highly responsive to the underlying substrate stiffness, its biomechanical mechanism is not totally understood. As is have been clearly demonstrated that the activity levels of integrin bound proteins are changing in response to mechanical stimuli, the crosstalk between BMP signaling and Integrin signaling has been believed to happen downstream. Yet, with more and more discoveries of direct crosstalk of integrin proteins and growth factors receptors, the mechanotransduction effects on osteoblasts development require to be re-considered and further understood.

Wnt signaling pathway

The Wnt signaling related glycoproteins are involved in critical biological processed such as cell fate determination during embryonic development, cell cycle arrest, cell proliferation, cell

differentiation, apoptosis and tissue homeostasis [[71]]. That is to say, Wnt signaling is involved in all aspects of embryonic development, as well as the homeostatic self-renewal of adult tissues (Fig. 2.9) [[72]]. It has been previously reported that Wnt signaling was able to promote proliferation of human mesenchymal stem cells and suppress osteogenic differentiation [[73]]. In the meanwhile, however, the promotion effect on osteoblast differentiation was as well discovered in another study [[74]] and the suppression of Wnt signaling was also considered to be possible to promote cell proliferation [[75]]. Moreover, increased Wnt signaling was detected in more differentiated cells [[76]], making the role of Wnt signaling in cell fate more complicated. At the same time, dose and time dependent effects were discovered [73,[77]], indicating a possible explanation for the reported contradictory results. Therefore, more work needs to be done to further clarify the relationship between Wnt signaling pathway and cell behavior both *in vitro* and *in vivo*.

It has been previously described that with the mechanical stimulation, the expression of sclerostin, which is an inhibitor of the Wnt signaling pathway, from osteocyte would be suppressed, allowing Wnt signaling-dependent bone formation to occur [[78],[79]]. At the same time, however, another study has shown a contradictory result that the inhibition of Wnt signaling can also stimulate osteoblast differentiation and mineral formation. Previous study described that Wnt signaling in maturing osteoblasts needs to be down-regulated to enable the formation of a mineralized bone matrix [[80]]. Although with the biphasic influence of Wnt signaling on osteogenic differentiation, its important role in mechanotransduction has been recognized [[81]]. Hence, more studies will be necessary to further clarify the potential biochemical mechanism of Wnt signaling response to static mechanical stimulations of matrix cells growing on.

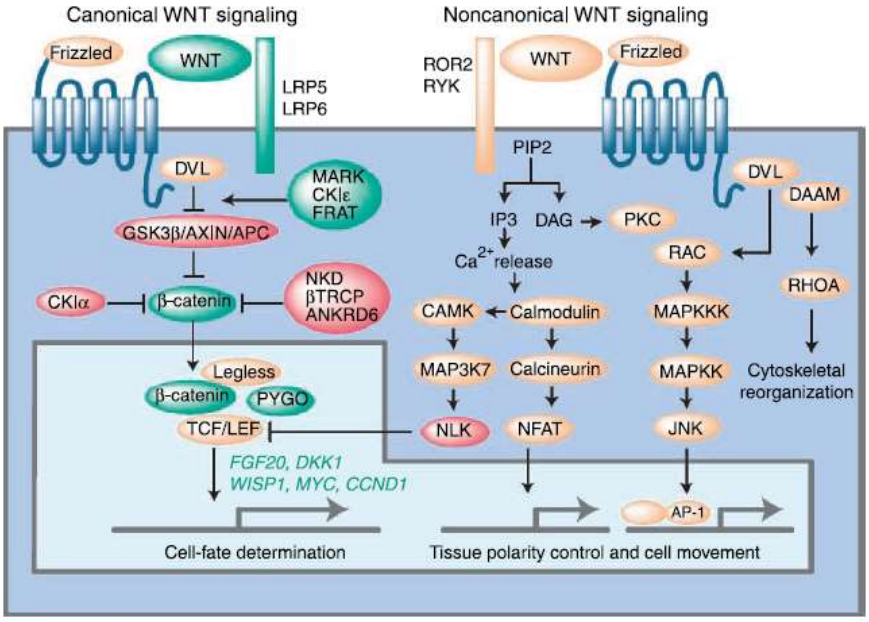

Figure 0.10 WNT signaling cascades. WNT signals are transduced for cell fate determination and control of cellmovement and tissue polarity.[82]

Reference

[1] Anthony D. Metcalfe, Mark W. J. Ferguson; Tissue engineering of replacement skin: thecrossroads of biomaterials, wound healing, embryonic development, stem cells and regeneration; Journal of the royal society interface (2007) 4, 413-437.
[2] Moon Suk Kim, Jae Ho Kim, Byoung Hyun Min, Heung Jae Chun, Dong Keun Han, Hai Bang Lee; Polymeric Scaffolds for Regenerative Medicine; Polymer Review, 51:23-52, 2011.
[3] Sujata K. Bhatia; Tissue engineering for clinical applications; Biotechnol. J. 2010, 5, 1309–1323.
[4] Molly S. Shoichet; Polymer Scaffolds for Biomaterials Applications; Macromolecules 2010, 43, 581–591.
[5] Zhong, S. P., Zhang, Y. Z., Lim, C. T. (2010). Tissue scaffolds for skin wound healing and dermal reconstruction. Wiley Interdisciplinary Reviews: Nanomedicine and Nanobiotechnology, 2(5), 510-525.
[6] Ng, K. W., Hutmacher, D. W., Schantz, J. T., Ng, C. S., Too, H. P., Lim, T. C., Phan, T. T., Teoh, S. H. (2001). Evaluation of ultra-thin poly (ε-caprolactone) films for tissue-engineered skin. Tissue engineering, 7(4), 441-455.
[7] Dai, N. T., Williamson, M. R., Khammo, N., Adams, E. F., Coombes, A. G. A. (2004). Composite cell support membranes based on collagen and polycaprolactone for tissue engineering of skin. Biomaterials, 25(18), 4263-4271.
[8] Garg, T., Singh, O., Arora, S., Murthy, R. S. R. (2012). Scaffold: a novel carrier for cell and drug delivery. *Critical Reviews™ in Therapeutic Drug Carrier Systems*, *29*(1).
[9] Kon E, Filardo G, Roffi A, Di Martino A, Hamdan M, De Pasqual L, Merli ML, Marcacci M, Bone regeneration with mesenchymal stem cells, Clin Cases Miner Bone Metab. 2012 Jan;9(1):24-7.
[10] Rosset P, Deschaseaux F, Layrolle P, Cell therapy for bone repair, Orthop Traumatol Surg Res. 2014 Feb;100(1 Suppl):S107-12.
[11] Kim, B. S., Park, I. K., Hoshiba, T., Jiang, H. L., Choi, Y. J., Akaike, T., Cho, C. S. (2011). Design of artificial extracellular matrices for tissue engineering. *Progress in Polymer Science*, *36*(2), 238-268.
[12] Hulbert, S. F., Young, F. A., Mathews, R. S., Klawitter, J. J., Talbert, C. D., Stelling, F. H. (1970). Potential of ceramic materials as permanently implantable skeletal prostheses. *Journal of biomedical materials research*,*4*(3), 433-456.
[13] Cadosch, D., Chan, E., Gautschi, O. P., Filgueira, L. (2009). Metal is not inert: role of metal ions released by biocorrosion in aseptic loosening—current concepts. Journal of Biomedical Materials Research Part A, 91(4), 1252-1262.
[14] Maspero, F. A., Ruffieux, K., Müller, B., Wintermantel, E. (2002). Resorbable defect analog PLGA scaffolds using CO2 as solvent: structural characterization. *Journal of biomedical materials research*, *62*(1), 89-98.
[15] An, Y. H., Woolf, S. K., Friedman, R. J. (2000). Pre-clinical in vivo evaluation of orthopaedic bioabsorbable devices. *Biomaterials*, *21*(24), 2635-2652.
[16] Moon Suk Kim, Jae Ho Kim, Byoung Hyun Min, Heung Jae Chun, Dong Keun Han, Hai Bang Lee; Polymeric Scaffolds for Regenerative Medicine; Polymer Review, 51:23-52, 2011.
[17] V. Guarino, F. Causa, A. Salerno, L. Ambrosio, P. A. Netti; Design and manufacture of microporous polymeric materials with hierarchal complex structure for biomedical application; Materials Science and Technology (2008) 24-9:1111-1117.

[18] D. Puppi, F. Chiellini, A.M. Piras, E. Chiellini; Polymeric materials for bone and cartilage repair; Progress in Polymer Science 35 (2010) 403–440.
[19] Xiaohua Liu, Peter X. Ma; Polymeric Scaffolds for Bone Tissue Engineering; Annals of Biomedical Engineering, (2004) 32-3: 477–486.
[20] Jinku Kim, Michael J. Yaszemski, Lichun Lu; Three-Dimensional Porous Biodegradable Polymeric Scaffolds Fabicated with Biodegradable Hydrogel Porogens; Tissue Engineering: Part C (2009) 15-4: 583: 594.
[21] Peter X. Ma, Ji-Won Choi; Biodegradable Polymer Scaffolds with Well-Defined Interconnected Spherical Pore Network; Tissue Engineering (2001) 7-1: 23-33.
[22] F. Carfı Pavia, V. La Carrubba, S. Piccarolo, V. Brucato; Polymeric scaffolds prepared via thermally induced phase separation: Tuning of structure and morphology; Wiley InterScience; (2007) 459:466.
[23] Ming-Hua Ho, Pei-Yun Kuo, Hsyue-Jen Hsieh, Tzu-Yang Hsien, Lein-Tuan Hou, Juin-Yih Lai, Da-Ming Wang; Preparation of porous scaffolds by using freeze-extraction and freeze-gelation methods; Biomaterials 25 (2004) 129–138.
[24] David J. Mooney, Daniel F. Baldwin, Nam P. Suh, Joseph P. Vacanti, Robert Larger; Novel approach to fabricate porous sponges of poly(o,klactic-co-glycolic acid) without the use of organic solvents; Biomaterials 17 (1996) 1417-1422.
[25] Zigang Ge, Zhaoxia Jin, Tong Cao; Manufacture of degradable polymeric scaffolds for bone regeneration; Biomed. Mater. 3 (2008) 022001 (11pp).
[26] Yoon Sung Nam, Jun Jin Yoon, Tae Gwan Park; A Novel Fabrication Method of Macroporous Biodegradable Polymer Scaffolds Using Gas Foaming Salt as a Porogen Additive; 2000 J. Biomed. Mater. Res. 53 1.
[27] Bose, S., Vahabzadeh, S., Bandyopadhyay, A. (2013). Bone tissue engineering using 3D printing. *Materials Today*, *16*(12), 496-504.
[28] Bose, S., Roy, M., Bandyopadhyay, A. (2012). Recent advances in bone tissue engineering scaffolds. *Trends in biotechnology*, *30*(10), 546-554.
[29] Lee, M., Dunn, J. C., Wu, B. M. (2005). Scaffold fabrication by indirect three-dimensional printing. *Biomaterials*, *26*(20), 4281-4289.
[30] Lam, C. X. F., Mo, X. M., Teoh, S. H., Hutmacher, D. W. (2002). Scaffold development using 3D printing with a starch-based polymer. *Materials Science and Engineering: C*, *20*(1), 49-56.
[31] Jacot-Descombes, L., Gullo, M. R., Cadarso, V. J., Brugger, J. (2012). Fabrication of epoxy spherical microstructures by controlled drop-on-demand inkjet printing. *Journal of Micromechanics and Microengineering*, *22*(7), 074012.
[32] J.P. Santerre, K. Woodhouse, G. Laroched, R.S. Labow; Understanding the biodegradation of polyurethanes: From classical implants to tissue engineering materials; Biomaterials 26 (2005) 7457–7470.
[33] Yanling Luo, Changhu Zhang, Feng Xu, Yashao Chen, Lihua Fan, Qingbo Wei; Synthesis and characterization of novel THTPBA/PEG-derived polyurethane scaffolds for tissue engineering; J Mater Sci (2010) 45:1866–1877.
[34] Sibylle Grad, Laszlo Kupcsik, Katarzyna Gorna, Sylwester Gogolewski, Mauro Alini; The use of biodegradable polyurethane scaffolds for cartilage tissue engineering: potential and limitations; Biomaterials 24 (2003) 5163–5171.
[35] M. Zanetta, N. Quirici, F. Demarosi, M.C. Tanzi, L. Rimondini, S. Fare; Ability of polyurethane foams to support cell proliferation and the differentiation of MSCs into osteoblasts;

Acta Biomaterialia 5 (2009) 1126–1136.
[36] Bj ¨orn Carlberg, Mathilda Zetterstr ¨om Axell, Ulf Nannmark, Johan Liu, and H Georg Kuhn; Electrospun polyurethane scaffolds for proliferation and neuronal differentiation of human embryonic stem cells; Biomed. Mater. 4 (2009) 045004 (7pp).
[37] Bing Li, Toshitaka Yoshii, Andrea E. Hafeman, Jeffry S. Nyman, Joseph C. Wenke, Scott A. Guelcher; The effects of rhBMP-2 released from biodegradable polyurethane/microsphere composite scaffolds on new bone formation in rat femor; Biomaterials 30 (2009) 6768-6779.
[38] Jerold E. Dumas, Katarzyna Zienkiewics, Shaun A. Tanner, Edna M. Prieto, Subha Bhattacharyya, Scott A. Guelcher; Synthesis and Characterization of an Injectable Allograft Bone/Polymer Composite Bone Void Filler with Tunable Mechanical Properties; Tissue Engineering: Part A, Volume 16, Number 8, 2010.
[39] Scott A. Guelcher; Biodegradable Polyurethanes: Synthesis and Applications in Regenerative Medicine; TISSUE ENGINEERING: Part B Volume 14, Number 1, (2008).
[40] Kavlock, K. D., Pechar, T. W., Hollinger, J. O., Guelcher, S. A., Goldstein, A. S. (2007). Synthesis and characterization of segmented poly (esterurethane urea) elastomers for bone tissue engineering. Acta biomaterialia, 3(4), 475-484.
[41] Rosa M Hernandez, Gorka Orive, Ainhoa Murua, Jose Luis Pedraz; Microcapsules and microcarriers for in situ cell delivery; Advanced Drug Delivery Reviews (2010).
[42] Augst, A. D., Kong, H. J., Mooney, D. J. (2006). Alginate hydrogels as biomaterials. Macromolecular bioscience, 6(8), 623-633.
[43] Nan Wang, Gary Adams, Lee Buttery, Franco H. Falcone, Snow Stolnik; Alginate encapsulation technology supports embryonic stem cells differentiation into insulin-producing cells; Journal of Biotechnology 144 (2009) 304-312.
[44] Novikova, L. N., Mosahebi, A., Wiberg, M., Terenghi, G., Kellerth, J. O., Novikov, L. N. (2006). Alginate hydrogel and matrigel as potential cell carriers for neurotransplantation. Journal of Biomedical Materials Research Part A, 77(2), 242-252.
[45] Bouhadir, K. H., Lee, K. Y., Alsberg, E., Damm, K. L., Anderson, K. W., Mooney, D. J. (2001). Degradation of partially oxidized alginate and its potential application for tissue engineering. Biotechnology progress, 17(5), 945-950.
[46] Martino, S., D'Angelo, F., Armentano, I., Kenny, J. M., Orlacchio, A. (2012). Stem cell-biomaterial interactions for regenerative medicine.*Biotechnology advances*, *30*(1), 338-351.
[47] Kumari, A., Yadav, S. K., Yadav, S. C. (2010). Biodegradable polymeric nanoparticles based drug delivery systems. *Colloids and Surfaces B: Biointerfaces*, *75*(1), 1-18.
[48] Murat Guvendiren, Jason A. Burdick; Stiffening hydrogels to probe short- and long-term cellular responses to dynamic mechanics; nature communications, 3:792, DOI: 10.1038 ncomms1792;
[49] Stephanie Nemir, Heather N. Hayenga, Jennifer L. West; PEGDA Hydrogels With Patterned Elasticity: Novel Tools for the Study of Cell Response to Substrate Rigidity; Biotechnology and Bioengineering, Vol. 105, No. 3, February 15, 2010.
[50] Robert J. Pelham, Jr., And Yu-Li Wang; Cell locomotion and focal adhesions are regulated by substrate flexibility; Proceedings of the National Academy of Sciences of the United States of America, 94(25), 13661–13665 (1997).
[51] Shelly R. Peyton, Cyrus M. Ghajar, Chirag B. Khatiwala, Andrew J. Putnam; The emergence of ECM mechanics and cytoskeletal tension as important regulators of cell function; Cell Biochem Biophys (2007) 47:300–320.
[52] John M. Collins, Perla Ayala, Tejal A. Desai, Brenda Russell; Three Dimensional Culture

with Stiff Microstructures Increases Proliferation and Slows Osteogenic Differentiation of Human Mesenchymal Stem Cells; Small. 2010 February 5; 6(3): 355–360.
[53] Rodero, M. P., Khosrotehrani, K. (2010). Skin wound healing modulation by macrophages. *International journal of clinical and experimental pathology*,*3*(7), 643.
[54] Novak, M. L., Koh, T. J. (2013). Macrophage phenotypes during tissue repair. *Journal of leukocyte biology*, *93*(6), 875-881.
[55] Mills, C. D., Kincaid, K., Alt, J. M., Heilman, M. J., Hill, A. M. (2000). M-1/M-2 macrophages and the Th1/Th2 paradigm. *The Journal of Immunology*,*164*(12), 6166-6173.
[56] Brown, B. N., Londono, R., Tottey, S., Zhang, L., Kukla, K. A., Wolf, M. T., Daly, K.A., Reing, J.E., Badylak, S. F. (2012). Macrophage phenotype as a predictor of constructive remodeling following the implantation of biologically derived surgical mesh materials. *Acta biomaterialia*, *8*(3), 978-987.
[57] Maniotis, A. J., Chen, C. S., Ingber, D. E. (1997). Demonstration of mechanical connections between integrins, cytoskeletal filaments, and nucleoplasm that stabilize nuclear structure. Proceedings of the National Academy of Sciences, 94(3), 849-854.
[[58]] Chenyu Huang, and Rei Ogawa; Mechanotransduction in bone repair and regeneration; The FASEB Journal, Vol. 24 October 2010, 3625-3632.
[59] Lau, KH., Kapur, S., Kesavan, C., Baylink, DJ., Up-regulation of the Wnt, estrogen receptor, insulin-like growth factor-I, and bone morphogenetic protein pathways in C57BL/6J osteoblasts as opposed to C3H/HeJ osteoblasts in part contributes to the differential anabolic response to fluid shear, J Biol Chem. 2006 Apr 7;281(14):9576-88.
[60] Cao, T. V., Hicks, M. R., & Standley, P. R. (2013). In Vitro Biomechanical Strain Regulation of Fibroblast Wound Healing. *JAOA: Journal of the American Osteopathic Association*, *113*(11), 806-818.
[61] Anderson, J. M., Rodriguez, A., Chang, D. T. (2008, April). Foreign body reaction to biomaterials. In Seminars in immunology (Vol. 20, No. 2, pp. 86-100). Academic Press.
[62] Harburger, D. S., Calderwood, D. A. (2009). Integrin signalling at a glance.*Journal of cell science*, *122*(2), 159-163.
[63] Morse, E. M., Brahme, N. N., Calderwood, D. A. (2014). Integrin Cytoplasmic Tail Interactions. *Biochemistry*, *53*(5), 810-820.
[64] Schoenwaelder, S. M., Burridge, K. (1999). Bidirectional signaling between the cytoskeleton and integrins. Current opinion in cell biology, 11(2), 274-286.
[65] Zhong, C., Chrzanowska-Wodnicka, M., Brown, J., Shaub, A., Belkin, A. M., Burridge, K. (1998). Rho-mediated contractility exposes a cryptic site in fibronectin and induces fibronectin matrix assembly. *The Journal of cell biology*, *141*(2), 539-551.
[66] Katsumi, A., Orr, A. W., Tzima, E., Schwartz, M. A. (2004). Integrins in mechanotransduction. Journal of Biological Chemistry, 279(13), 12001-12004.
[67] Jaalouk, D. E., Lammerding, J. (2009). Mechanotransduction gone awry. Nature reviews Molecular cell biology, 10(1), 63-73.
[68] Boettiger D. Mechanical control of integrin-mediated adhesion and signaling. Current opinion in cell biology. 2012;24:592-9
[69] Moore SW, Roca-Cusachs P, Sheetz MP. Stretchy proteins on stretchy substrates: the important elements of integrin-mediated rigidity sensing. Developmental cell. 2010;19:194-206.
[70] Eliceiri, B. P. (2001). Integrin and growth factor receptor crosstalk. Circulation research, 89(12), 1104-1110.
[71] Jia-Ling Teo, Michael Kahn; The Wnt signaling pathway in cellular proliferation and

differentiation: A tale of two coactivators; Advanced Drug Delivery Reviews 62 (2010) 1149–1155.
[72] Hans Clevers; Wnt/β-Catenin Signaling in Development and Disease; Cell 127, November 3, 2006, 469-480.
[73] Genevieve M. Boland, Geraldine Perkins, David J. Hall, and Rocky S. Tuan; Wnt 3a Promotes Proliferation and Suppresses Osteogenic Differentiation of Adult Human Mesenchymal Stem Cells; Journal of Cellular Biochemistry 93:1210–1230 (2004).
[74] Kristina Kapinas, Catherine Kessler, Tinisha Ricks, Gloria Gronowicz, and Anne M. Delany; miR-29 Modulates Wnt Signaling in Human Osteoblasts through a Positive Feedback Loop; THE JOURNAL OF BIOLOGICAL CHEMISTRY VOL. 285, NO. 33, pp. 25221–25231, August 13, 2010.
[75] Maria P. Alfaro, Matthew Pagni, Alicia Vincent, James Atkinson, Michael F. Hill, Justin Catesa, Jeffrey M. Davidson, Jeffrey Rottman, Ethan Lee, and Pampee P. Young; The Wnt modulator sFRP2 enhances mesenchymal stem cell engraftment, granulation tissue formation and myocardial repair; 18366–18371, PNAS, November 25, (2008) vol. 105, no. 47.
[76] Ivo Kalajzic, Ada Staal, Wen-Pin Yang, Yuli Wu, Susan E. Johnson, Jean H. M. Feyen, Winfried Krueger, Peter Maye, Fang Yu, Yifang Zhao, Lynn Kuo, Rishi R. Gupta, Luke E. K. Achenie, Hsin-Wei Wang, Dong-Guk Shin, and David W. Rowe; Expression Profile of Osteoblast Lineage at Defined Stages of Differentiation; Vol. 280, No. 26, Issue of July 1, pp. 24618–24626, 2005.
[77] Jan de Boer, Ramakrishnaiah Siddappa, Claudia Gaspar, Aart van Apeldoorn, Ricardo Fodde, and Clemens van Blitterswijk; Wnt signaling inhibits osteogenic differentiation of human mesenchymal stem cells; Bone 34 (2004) 818– 826.
[78] Alexander G. Robling, Paul J. Niziolek, Lee A. Baldridge, Keith W. Condon, Matthew R. Allen, Imranul Alam, Sara M. Mantila, Jelica Gluhak-Heinrich, Teresita M. Bellido, Stephen E. Harris, and Charles H. Turner; Mechanical Stimulation of Bone in Vivo Reduces Osteocyte Expression of Sost/Sclerostin; The Journal Of Biological Chemistry VOL. 283, NO. 9, Pp. 5866–5875, February 29, 2008.
[79] Charles H. Turner, Stuart J. Warden, Teresita Bellido, Lilian I. Plotkin, Natarajan Kumar, Iwona Jasiuk, Jon Danzig, Alexander G. Robling; Mechanobiology of the Skeleton; www.SCIENCESIGNALING.org, 28 April (2009) Vol 2, Issue 68 pt3.
[80] Geertje van der Horst, Steffie M van der Werf, Hetty Farih-Sips, Rutger L van Bezooijen, Clemens WGM L öwik, and Marcel Karperien; Downregulation of Wnt Signaling by Increased Expression of Dickkopf-1 and -2 is a Prerequisite for Late-Stage Osteoblast Differentiation of KS483 Cells; J. Bone Miner. Res. 20, 1867–1877.
[81] Justus H.W. Jansen, Marco Eijken, Holger Jahr, Hideki Chiba, Jan A.N. Verhaar, Johannes P.T.M. van Leeuwen, Harrie Weinans; Stretch-Induced Inhibition of Wnt/b-Catenin Signaling in Mineralizing Osteoblasts; J. Orthop. Res. 28, 390–396.
[82] Katoh, M., Katoh, M. (2007). WNT signaling pathway and stem cell signaling network. *Clinical Cancer Research*, *13*(14), 4042-4045.

CHAPTER 3

A TRANSIENT CELL-SHIELDING METHOD FOR VIABLE MSC DELIVERY WITHIN HYDROPHOBIC SCAFFOLDS POLYMERIZED *IN SITU*

1.Introduction

Autologous and allogeneic cell-based therapies have emerged as promising approaches for regenerative medicine [1]. While direct injection of cells has limited therapeutic efficacy due to poor cell survivability [2-4], delivery of cells within a 3D matrix can improve integration with host tissue and promote healing [5]. Injectable and settable cell carriers could be advantageous as a minimally invasive surgical approach to rapid filling of complex defects followed by *in situ* curing to form a porous scaffold with suitable mechanical properties [6].

Lysine-derived poly(ester urethane)s (PURs) offer potential advantages as injectable carriers for local cell delivery, such as curing using non-cytotoxic catalysts [7] without the need for UV radiation [8], support of cell attachment without cell adhesion peptides [9, 10], tunable hydrolytic and oxidative degradation to non-cytotoxic breakdown products [11, 12], and adjustable mechanical properties ranging from those of soft tissue [13] to bone [9, 14]. Furthermore, macropores can be generated within PUR scaffolds by CO_2 gas foaming via the reaction of isocyanate groups with water [15]. When using these materials as acellular scaffolds, the CO_2 and heat generated by the *in situ* reaction is well tolerated at the biomaterial-tissue interface [7, 16] due to the relatively long length scales (>1 mm) between the material and surrounding cells (Figure 3.1A). However, cells encapsulated within the reactive material experience steeper CO_2 and temperature gradients due to transport of reaction products over much smaller length scales (<100

μm, Figure 3.1B). Furthermore, after the reaction is complete, hydrophobic polymers absorb negligible amounts of water and allow less diffusion of vital cell nutrients and wastes than swollen hydrogels. While hydrophobic biomaterials provide a generalizable, biodegradable platform for tissue scaffolding, their use as an injectable system for cell delivery has not been achieved due to two primary challenges: (1) maintenance of cell viability during *in situ* polymerization, and (2) provision of an interconnected, macroporous structure to allow effective nutrient and waste exchange post-cure. Overcoming these key barriers was the goal of the current work in order to enable the use of injectable, settable, mechanically robust, and cell-adhesive PUR networks to fill tissue defects and to locally deliver and retain viable cells in vivo.

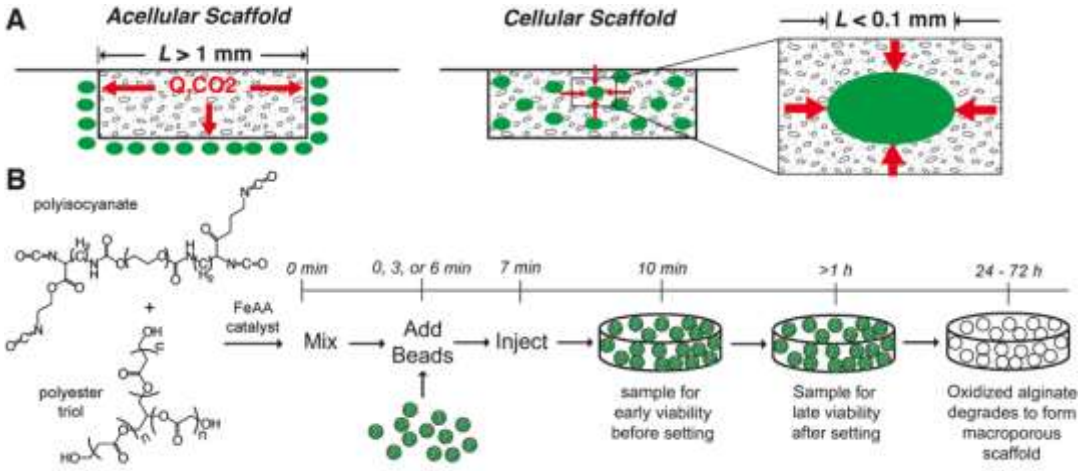

Figure 0.1 Design of injectable, settable carriers for cell delivery.
(A) For an acellular scaffold, the length scale of diffusion of reaction products is comparable to the size of the tissue defect. However, in a cellular scaffold, reaction products diffuse radially toward the encapsulated cell over a much shorter length scale (comparable to the size of the cell). (B) Schematic illustrating the design concept in which an NCO-functional prepolymer reacts with a polyester polyol in the presence of an iron acetylacetonoate (FeAA) catalyst to form a polyurethane network. Encapsulation of cells in oxidized alginate beads (green) provides temporary protection from the chemical reaction and is followed by hydrolytic degradation of the oxidized alginate to form interconnected macropores that are enhanced by the NCO-water reaction.

Achieving these goals will provide a new alternative to photopolymerizable systems that utilize cytocompatible initiators [17, 18] and water-soluble macromers [19-21] to encapsulate cells in injectable hydrogels [8]. Polyethylene glycol (PEG)-based hydrogels have generated considerable interest for localized cell delivery since they can be administered by minimally-invasive injections, set within clinically relevant working times, exhibit tissue-like structure, and induce a minimal inflammatory response [1, 22-24]. However, PEG hydrogels must be functionalized with an optimal combination of peptides that serve as integrin-binding sites for cell adhesion and peptide crosslinkers that are matrix metalloproteinase (MMP) substrates to enable cellular infiltration and cell-mediated hydrogel degradation [5, 25].

Alternative settable carriers must protect cells from reaction products prior to cure and then set *in situ* to form an interconnected, macroporous scaffold that supports cell adhesion and growth. In this study, we designed injectable PUR scaffolds for concurrent incorporation of macropores and cells within PUR scaffolds (Figure 3.1B). Through encapsulation within partially oxidized sodium alginate (o-Alg) beads, cells were protected from the PUR reaction prior to gelation. Hydrolytic degradation of the o-Alg beads within the first 1 – 2 days after gelation was anticipated to result in cell release and attachment to the scaffold. Thus, in contrast to the porogen co-encapsulation approach [26, 27], the o-Alg beads functioned both as a temporary barrier to transport of reaction products as well as a porogen. Encapsulation of cells within o-Alg beads prior to embedding in an injectable calcium phosphate cement (CPC) has been reported to protect cells from mechanical stress [28]. However, the utility of o-Alg as a barrier to heat and mass transfer in an exothermic, CO_2-generating polymerization reaction has not been studied. Thus,

we investigated the effects of o-Alg bead size and loading within PUR scaffolds and assessed the effects of heat and CO_2 generation rates on cell survivability both prior to and after cure *in vitro*. In a proof-of-concept experiment, the lead-candidate formulation that produced maximal cell viability *in vitro* was injected into full-thickness excisional skin wounds in Sprague-Dawley rats to evaluate the potential of the injectable PUR stem cell carrier for wound repair and restoration *in vivo*.

2. Materials and Methods

2.1. Materials

The sodium salt of alginic acid (Alg, viscosity = 20 – 40 cPs) was supplied by Sigma Aldrich (St. Louis, MO). Acros Organics supplied calcium chloride and glycerol. αMEM and DMEM were supplied by GIBCO. Fetal bovine serum (FBS) was purchased from Thermo Scientific. Penicillin/streptomycin (P/S), trypsin EDTA and Amphotericin B were obtained from Corning Cellgro. Live/Dead kits for mammalian cells were supplied by Life Technologies. Glycolide and D,L-lactide were purchased from Polysciences (Warrington, PA). A lysine triisocyanate-poly(ethylene glycol) (LTI-PEG) prepolymer was supplied by Medtronic, Inc, and hexamethylene diisocyanate trimer (HDIt) was supplied by Bayer Material Science. Iron acetylacetonate and other materials were supplied by Sigma-Aldrich. ε-caprolactone was dried over anhydrous $MgSO_4$, and all other materials were used as received.

2.2. Cell culture

MC3T3 cells (ATCC) were cultured in a complete medium of αMEM with 10% FBS and 1% P/S. Primary rat bone marrow mesenchymal stem cells (BMSCs) were maintained in DMEM with 10% FBS, 1% P/S, and 0.1% Amphotericin B (Sigma). BMSCs were generated from pooled bone marrow from 4 male Sprague-Dawley rats. Cells were not sorted prior to encapsulation, since the objective was to design a translatable system in which cells could be harvested and immediately encapsulated. Rat femora and tibiae were removed after sacrificing and bone marrow was flushed out with BMSC culture medium. After centrifuging, cell pellets were suspended in BMSC culture medium and plated in T75 tissue culture flasks. Three days after seeding, floating cells were removed and culture medium refreshed every other day. Harvested BMSCs at passage 3 were then plated in 24-well plates and fed with culture medium modified with osteogenic (10 nM dexamethasone and 0.1 mM β-glycerophosphate) or adipogenic (10 μM dexamethasone (dex), 10 μg/ml insulin, 100 μg/ml IBMX) supplements for differentiation (21 days). Alizarin red staining (Figure 3.2A) and Oil red O staining (Figure 3.2B) were performed after fixation of cell monolayer in 10% formalin for 30 min. Cells of passage 5-10 were detached at sub-confluency by trypsin EDTA (0.25%) and suspended in alginate solution at 10^5 cells/ml for encapsulation.

2.3. Preparation of partially oxidized alginate

An aqueous solution of sodium periodate (2.0 mM) was mixed with 1 w/v% solution of sodium alginate (Alg) and reacted in the dark for 24 h at ambient temperature. Two drops of ethylene glycol were added to stop oxidation. The resultant solution was precipitated in ethanol (2:1 v/v ethanol/water) and sodium chloride (6.25 g/L). Precipitates were dissolved in distilled

water to the original volume, precipitated in ethanol solution, and dried under vacuum at room temperature. After drying, partially oxidized sodium alginate (o-Alg) was dissolved in distilled water, filtered, and lyophilized [29]. A concentration of 4 w/v% of o-Alg was utilized to generate hydrogel beads.

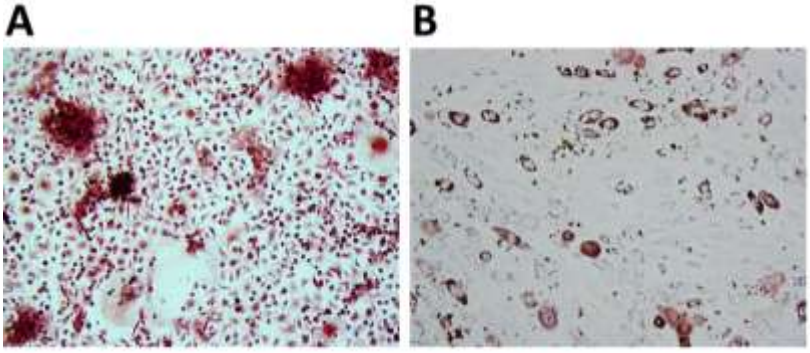

Figure 0.2 Osteogenic and adipogenic differentiation of bone marrow-derived mesenchymal stem cells (BMSCs).

(A) BMSCs cultured for 21 days in osteogenic medium and stained with Alizarin Red. (B) BMSCs cultured for 21 days in adipogenic medium and stained with Oil red O.

2.4. Encapsulation of cells in alginate beads

Cells (10^5 cells/mL) were encapsulated in calcium alginate hydrogel by pumping the sodium alginate solution (1 w/v% for Alg and 4 w/v% for o-Alg) through a nozzle (diameter=0.35μm) into a 100 mM calcium chloride crosslinking solution. An electronic bead maker (Nisco, VAR V1) was used to control bead size over the range 300 – 1000 μm by adjusting the potential difference between the nozzle and gelling agent solution [30]. Alginate bead size was measured by light microscopy.

2.5. Synthesis and characterization of polyurethane scaffolds

A polyester triol (900 g/mol) was synthesized from a glycerol starter and a backbone comprising 70 wt% ε-caprolactone, 20 wt% glycolide, and 10 wt% D,L-lactide as described previously [31]. An isocyanate (NCO)-terminated prepolymer (21,000 cP, NCO:OH equivalent ratio = 3.0:1.0, 21% NCO [32]) was synthesized by adding polyethylene glycol (PEG, 200 g/mol) drop-wise to lysine triisocyanate (LTI). Polyurethane (PUR) scaffolds were synthesized by reactive liquid molding of the prepolymer with a hardener component comprising the polyester triol, iron catalyst (5% iron acetylacetonate (FeAA) in dipropylene glycol), and alginate beads. The reactivity of the LTI-PEG prepolymer was measured by using ATR-FTIR (Bruker, Billerica, MA) to quantify the disappearance of the NCO peak [7]. Rheological properties of the scaffolds during curing process were measured with a parallel plate AR 2000ex rheometer in dynamic mode (New Castle, DE) to determine the working time (crossover point of storage moduli (G') and loss moduli (G'')).

The pore size distribution and internal pore morphology of the scaffolds were determined by SEM (Hitachi, Finchampstead, UK). Porosity was calculated from mass and volume measurements of vacuum dried cylindrical scaffold cores (ρ_{PUR} = 1.27 g cm^{-3}) [15]. The Young's modulus was determined from the slope of the stress-strain curve from compression tests performed using a TA Instruments Dynamic Mechanical Analyzer Q1000 (New Castle, DE). The flow rate of air through a preformed scaffold was measured using a flowmeter (Cole Parmer, Chicago, IL) and the permeability calculated as:

$$k = Q\frac{L}{A}\left(\frac{m}{\Delta P}\right) \qquad (1)$$

where Q = volumetric air flow rate, L and A are the scaffold thickness and cross-sectional area, μ is the viscosity of air, and ΔP is the pressure drop across the scaffold [33].

2.6. Survival of encapsulated cells

The ability of cells to survive the polymerization was evaluated at 10 min after mixing of the polyisocyanate and polyester triol components. At this early time point, diffusion of heat and CO_2 into the beads (which occurs on the time scale of minutes) was anticipated to be the primary regulator of cell viability. The study design is summarized in Table 3.1. The polyisocyanate composition (LTI-PEG or HDIt), timing of 500 μm bead addition (0, 3, or 6 min delay), and catalyst concentration (0, 0.26, or 0.52 wt% FeAA) were varied to control the amount of cell exposure to the heat and CO_2 generated by the PUR reactions. The viability of cells embedded in unreactive controls with no catalyst was also measured to decouple any effects of chemical toxicity from loss of cell viability due to reaction-generated heat and CO_2. Beads containing cells were removed from the cured scaffolds at 10 min using forceps, washed with Dulbecco's Phosphate Buffered Saline (DPBS, Corning, Corning, NY), and stained with the Cytotoxicity Kit (Live/Dead® Viability/Cytotoxicity Kit for mammalian cells, Invitrogen). An inverted confocal microscope (Zeiss LSM 510) was used to capture images with live/dead cells inside beads after 30 min. The viability percentage was calculated as:

$$\% \text{ Viability} = \frac{N_{live}}{N_{total}} \times 100\% \qquad (2)$$

where N_{live} = the number of live cells (fluorescently green) and N_{total} = the number of all the stained

cells [34].

At later time points exceeding the gel time, cell survivability was anticipated to be limited by both exposure to reaction products as well as the permeability of the cured scaffolds, which controls the rate at which nutrients diffuse into the scaffold. Therefore, cell survivability was investigated at 10 min (prior to gelation), 30 min (at gelation), and 3 h (after gelation) post-mixing as a function of bead loading and timing of addition, which were expected to regulate scaffold permeability due to dissolution of the o-Alg beads and gas foaming. At each time point, Alg beads containing cells were removed from the cured scaffolds and stained with an Apoptotic & Necrotic Cell Differentiation kit (PromoCell GmbH). Apoptotic cells were identified with fluorescein- (FITC, green) labeled Annexin V, necrotic cells were identified with a positively charged nucleic acid probe Ethidium homodimer III (EthD-III, red), and Hoechst 33342 (blue) was used to identify the total number of cells. An inverted fluorescence microscope (Olympus CKX41) was used to identify healthy cells (blue only) as well as cells entering apoptosis (blue and green) or necrosis (blue, green, and red). The percentage of cells entering necrosis or apoptosis was calculated using Eq. (2). In another test group, scaffolds were incubated in PBS for 48 h to dissolve the o-Alg beads and the porosity and permeability measured as described above.

2.7. Culture of cellularized PUR scaffolds

PUR scaffolds embedded with rat BMSCs stained with a cytoplasmic dye (VyBrant® CFDA SE Cell Tracer Kit, Life Technologies, per the manufacturer's guidelines) and encapsulated in either Alg or o-Alg beads were fabricated and cultured in 48-well tissue culture plates for 1, 4,

and 7 days. Scaffolds were rinsed with DPBS and fixed with 5% glutaraldehyde or 2% OsO_4 solution before vacuum drying for SEM imaging. A subset of scaffolds was also sectioned (30 μm) for microscopic imaging to observe cell viability and attachment to the scaffolds.

The ability of the MSCs to retain pluripotency after embedding in the scaffolds was determined by measuring adipogenic and osteogenic differentiation. Scaffolds were maintained in growth, adipogenic, or osteogenic media for up to 21 days and stained with Oil Red O or Alizarin Red S. Immediately following staining, dyes were dissolved in appropriate solvents (100% isopropanol for Oil Red O and 5% SDS for Alizarin Red S) and absorbances of the solutions were read on a plate reader (OD 490nm for Oil Red O and OD 570nm for Alizarin Red S). Absorbances were compared to stained scaffolds cultured in growth media.

2.8. In vivo cutaneous repair in rats

All surgical and care procedures were carried out under aseptic conditions per an approved IACUC protocol. Scaffolds (n=4) that contained encapsulated male rat BMSCs were injected into 10 mm full-thickness excisional wounds in the dorsal skin of adult female Sprague-Dawley rats and allowed to cure for 15 min [16]. BMSCs from male rats encapsulated in Alg beads and embedded in PUR scaffolds did not integrate with host tissue and were consequently ejected from the wound bed. Therefore, only scaffolds containing o-Alg beads were evaluated at days 4 and 7. Injectable scaffolds containing no cells (Inj group) and implanted, pre-formed scaffolds seeded with cells (Impl+BMSC group) were both evaluated as controls compared to injectable scaffolds with cells (Inj+BMSC). Rats were euthanized 4d and 7d after surgery, and wounds

were harvested for histology and RT-PCR analysis. RNA from each sample was isolated and purified by RNeasy Mini Kit (Qiagen). cDNA synthesis was carried out from purified total RNA using iScript™ Reverse Transcription Supermix (Biorad). RT-PCR amplified for rat SRY gene (5′-CATCGAAGGGTTAAAGTGCCA-3′,5′-ATAGTGTGTAGGTTGTTGTCC-3′) was measured to track the fate of delivered cells. Gomori's trichrome, Ki67, and collagen IV immunostaining were performed on tissue sections for tissue infiltration, cell proliferation and angiogenesis analysis, respectively. The ROI (region of interest) for quantitative analysis of tissue infiltration comprised a rectangle centered between the midpoint and the edge of the excisional wound. The reactivity was expressed as the percentage of area occupied by immunoreactive cells.

2.9 Scanning Electron Microscopy (SEM)

Following in vitro culture, the scaffolds were cut open to expose the center surfaces. Scaffolds were fixed in 10% formalin for 15 minutes, then washed in PBS and dehydrated through increasing alcohol concentrations (50-100%). Materials were air-dried and mounted to a specimen stub using carbon tape. Samples were sputter-coated with gold (108 Auto Sputter Coater; TedPella, Redding CA) and viewed via scanning electron microscopy (Carl Zeiss VP-40; Oberkochen, Germany).

2.10. Statistical analysis

The statistical significance between experimental groups was determined by a two-factor ANOVA ANOVA. Graphs show mean $\pm$ S.D., and $p \leq$ ANOVA. $p < 0.05$ is considered as statistically significant.

3.Results

3.1 Reactivity and settability

Injectable reactive liquid precursors that cure *in situ* to form a solid scaffold should ideally be amenable to flow through a small-bore needle and set within clinically relevant gelation times to form a polymer network with suitable mechanical properties [35-37]. The gel point (GP) approximates the working time available for injection, since beyond the gel point the mixture is no longer flowable. For a prepolymer with functionality of 4 and a polyol with functionality of 3, the gel point occurs at ξ_{GP} = 38% conversion of the reactive NCO groups [38], which was achieved at 25.5 min when cell-containing beads were immediately added to the reactive PUR mixture (Figure 3.3A).

Since CO_2 generated during the polymerization might harm the cell-loaded beads added to the reactive mixture, the effects of delaying the addition of the beads were also investigated. When addition of beads to the reactive PUR was delayed for 3 min, the gel point decreased to 19.5 min (Figure 3.3A). The working time can also be determined by the G'-G" crossover point (Figure 3.3B, C), at which point the storage modulus (G') equals the loss modulus (G"). For delayed addition, the crossover point occurred at 22 min, which is comparable to that determined from chemical reaction kinetics (Figure 3.3A). In contrast, for immediate addition, the crossover point occurred at 33 min (both G' and G" decreased with time at early time points due to significant volumetric expansion of the scaffold as a result of CO_2 generation (Figure 3.3C)). The data in Figure 3.3B-C indicate that the cream time, defined as the time at which the reactive mixture begins to expand in volume [39], was <15 min.

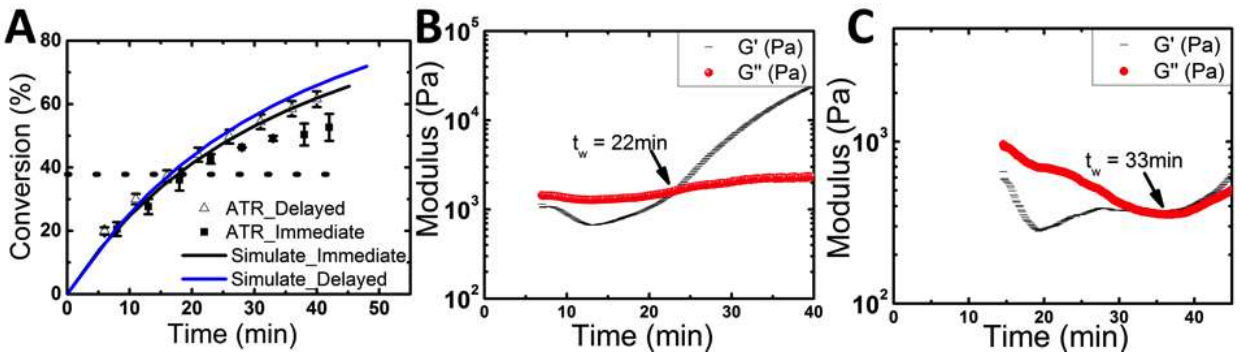

Figure 0.3 Handling properties of injectable and settable PUR scaffolds.

(A) Overall NCO conversion for immediate and delayed (3 min) addition of alginate beads. The gel point (i.e., working time t_w) occurred at 38% NCO conversion (dashed line), which corresponded to 19.5 min for delayed addition and 25.5 min for immediate addition. (B-C) Storage (G') and loss (G") moduli versus time for delayed (3 min, B) and immediate (C) addition of alginate beads. The value of t_w is defined as the G'-G" crossover point (22 min for delayed addition).

3.2 Effects of bead size on cell survival at early time points

MC3T3 cells were encapsulated in Alg beads that were immediately mixed (0 min delay) with the reactive PUR mixture. Beads were harvested from the scaffolds after 10 min and stained for live and dead cells. For 500 – 2000-μm diameter beads not embedded in PUR, the viability of encapsulated MC3T3 cells exceeded 95% and was independent of bead size (Figure 3.4A,C). However, when embedded in the reactive PUR (50 wt% bead loading, Figure 3.4B), cell viability decreased with decreasing bead size (Figure 3.4C). These observations suggest that transport of heat and/or CO_2 generated by the PUR reaction reduced cell survival at early (i.e, prior to gelation) time points.

3.3 Effects of delayed addition of MSCs on cell survivability at early time points

To investigate the effects of delayed addition of beads on cell survival, MC3T3 cells were encapsulated in Alg beads that were subsequently mixed with the reactive PUR. The timing of bead addition (0, 3, or 6 min delay), the isocyanate composition (LTI-PEG or HDIt), and the catalyst concentration (0, 0.26, or 0.52 wt% FeAA) were varied to control the amount of cell exposure to the heat and CO_2 generated (Figure 3.5A) by the PUR gelling (k_G) and blowing (k_B) reactions. The NCO groups in the polyisocyanate (R_1-NCO) react with hydroxyl groups (OH) in the polyester triol (R_2-OH) by the gelling reaction or in water (W) by the blowing reaction:

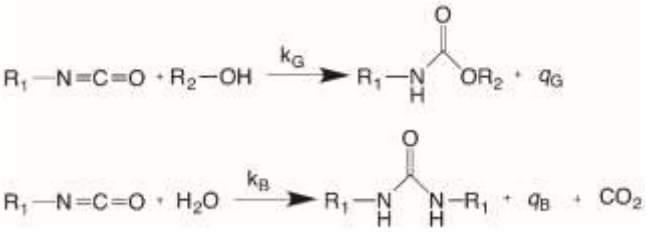

(1)

The amounts of heat (q_G or q_B) and CO_2 generated by Reaction (1) at 10 min were calculated from a PUR reaction kinetics model [7] (Q_{10} and $J_{CO2,10}$ listed in Figure 3.5A). Cell viability was measured at 10 min (V_{10}, Figure 3.5A) to test the hypothesis that transport of heat and CO_2 is the primary cause of acute cell death at early time points. The rates of the second-order gelling (r_G) and blowing (r_B) reactions are given by:

$$r_G = k_G C_{NCO} C_{OH,P}$$
$$r_B = k_B C_{NCO} C_{OH,W} \qquad (2)$$

where C_{NCO} is the concentration of NCO groups in the prepolymer (eq g^{-1}) and C_{OH} is the concentration of OH groups (eq g^{-1}) in the polyester triol (P) or water (W). The specific reaction rates k_G and k_B (Table 3.1) were calculated from kinetic experiments in which the polyisocyanate

was reacted with either the polyester triol (k_G) or water (k_B) and the disappearance of the NCO peak monitored by ATR-FTIR over time [7, 40].

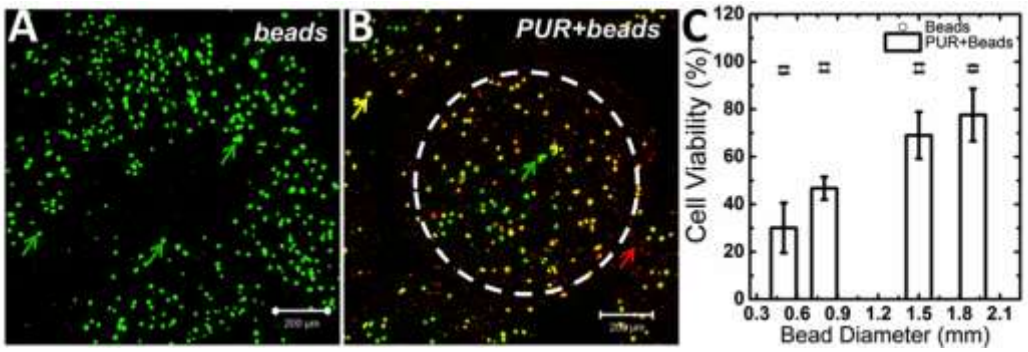

Figure 0.4 Effects of bead size on survival of MC3T3 cells encapsulated in o-Alg and embedded in a reactive hydrophobic polymer at early time points (10 min post-mixing).
(A) Confocal images show viable (green) cells in 500 μm beads. (B) Viability decreases when viable (green) MC3T3 cells encapsulated in Alg are immediately embedded in PUR scaffolds. Immediate embedding of Alg beads in PUR scaffolds resulted in significant cell death (yellow, orange, and red cells) near the surface of the beads. (C) The viability of encapsulated cells embedded in PUR scaffolds directly correlated with bead size, suggesting that transport of reaction products into the beads was responsible for the observed cytoxicity.

Table 0.1 Experimental conditions for early-stage (10 min) cell viability. Alginate beads were removed from the scaffolds 10 min after the start of mixing and viability measured by live/dead staining.

Treatment Group	**Isocyanate**	**FeAA catalyst wt%**	**Delay min**	**Rate Constant g eq^{-1} min^{-1}**	**k_G/k_W**
L-0C-0	LTI-PEG	0%	0	N/A	N/A
L-LC-0	LTI-PEG	0.26%	0	k_G = 12.1, k_B = 1.9	6.4
L-LC-3	LTI-PEG	0.26%	3		
L-LC-6	LTI-PEG	0.26%	6		
H-LC-0	HDIt	0.26%	0	k_G = 8.2, k_B = 0.61	13.4
H-HC-0	HDIt	0.52%	0	k_G = 31.4, k_B = 0.68	46.2

The concentration profiles of each component were calculated as a function of time by modeling the system as a constant-volume isothermal batch reactor, since the increase in

temperature in the bulk scaffold was <15°C [15]. The equivalent balance equations for polyester triol and water were solved $C_{OH,P}$ and $C_{OH,W}$ using the ode45 function in MATLAB:

$$\frac{dC_{OH,P}}{dt} = - r_G M_{PUR}, \quad t = 0, C_{OH,P} = C_{OH,P0}$$
$$\frac{dC_{OH,W}}{dt} = - r_B M_{PUR}, \quad t = 0, C_{OH,W} = C_{OH,W0} \qquad (3)$$

where M_{PUR} is the mass of the PUR component (polyisocyanate and polyester triol) and $C_{OH,P0}$ and $C_{OH,W0}$ denote the initial concentrations (eq g^{-1}) of polyester triol and water, respectively (details of how these parameters were determined are described in the Supplemental Information).

The heat generated by the gelling and blowing reactions as a function of time was normalized by the total alginate (A) bead area (Q, J cm^{-2}). The CO_2 generated by the blowing reaction was also normalized by the alginate bead area (mmol CO_2 cm^{-2}):

$$Q = \frac{\Delta H_{Rx} a_A r_A (1 - x_A)}{3 x_A} \left(\frac{C_{OH,P0} - C_{OH,P}}{f_P} - \frac{C_{OH,W0} - C_{OH,W}}{f_W} \right)$$
$$n_{CO2} = \frac{a_A r_A (1 - x_A)}{3 x_A} \left(\frac{C_{OH,W0} - C_{OH,W}}{f_W} \right) \qquad (4)$$

where f is the functionality (eq mol^{-1}), ΔH_{Rx} = 80 kJ mol^{-1} is the heat of reaction [41], a_A is the radius of the alginate beads, ρ_A = 1.601 g cm^{-3} is the density of alginate, and x_A is the weight fraction of alginate beads in the scaffold. The values of Q and n_{CO2} are plotted versus time in Figure 3.5B-C. The amounts of heat (Q_{10}) and CO_2 ($n_{CO2,10}$) generated at 10 minutes are listed in Figure 3.5A. The effects of Q_{10} and $n_{CO2,10}$ on cell viability (V_{10}) are shown in the contour plot in Figure 3.5D. The values of V_{10} were fit to the following equation to generate the contour plot:

$$V_{10} = 87.7 - 0.0883 \exp\left(56.35 n_{CO2,10}\right) - 1.34 \exp(3.76 Q_{10}) \qquad (5)$$

Mixing the beads with a non-reactive PUR mixture (LTI-PEG or HDIt) reduced the viability to

88%, which is about 10% less than that measured for the beads alone. For the region bounded by $Q_{10} < 0.4$ J cm^{-2} and $n_{CO2,10} < 0.08$ mmol cm^{-2}, the effects of the chemical reaction on cell viability were negligible. However, outside this range, V_{10} decreased exponentially with Q^*_{10} and $n^*_{CO2,10}$. Taken together, these data indicate that diffusion of both CO_2 and heat into the beads contributed to acute cell death at early time points.

3.4 Effects of permeability on cell survival at later time points

After gelation (20 – 30 min, Figure 3.1), the reactive PUR cures to form a solid scaffold, at which time diffusion of nutrients into the interior is also anticipated to affect cell viability. Permeability (eq (2)) and porosity are key parameters controlling the rate of diffusion of nutrients into the scaffold. Thus, the effects of bead loading and the timing of bead addition on the porosity, permeability, and mechanical properties of the PUR scaffolds were investigated. SEM images comparing scaffolds prepared by 3 min delayed addition of o-Alg beads at 50 wt versus 70 wt% (Figure 3.6A-B) supported this hypothesis and showed that pore connectivity increased with bead loading. As bead loading increased from 50 and 70 wt% (3 min delay), the increase in porosity was not significant (78 – 82%) but the air permeability increased five-fold increase in ($p<0.05$) after leaching to remove the beads (Figure 3.6C). Interestingly, the air permeability increased to values comparable to those reported for open-pore PUR foams with similar densities [33]. In contrast, when the beads were added immediately (0 min delay), neither permeability nor porosity increased with bead loading (Figure 3.6D). This observation suggests that CO_2 gas foaming contributed substantially to porosity and permeability when the beads were immediately added to

the PUR carrier. As shown in Figure 3.6E, the elastic modulus of scaffolds (E^*) prepared by either immediate or delayed addition of beads followed the predicted scaling with porosity ε [42]:

$$E^* = E_s\left(\frac{1 - r_s e}{r_s}\right)^2 \qquad (6)$$

where the density of the bulk polymer ρ_s = 1.27 g cm^{-3} and the modulus of the bulk polymer E_s = 2.5 MPa.

The data in Figures 3.4 – 3.5 point to diffusion of chemical reaction products into the Alg beads as a key factor contributing to acute cell death prior to gelation. At later time points, cells may undergo apoptosis or necrosis due to the continuing effects of the chemical reaction and/or limited diffusion of nutrients into the interior of the cured scaffold. To investigate the relative contributions of the chemical reaction and scaffold permeability to cell viability, Alg beads were removed from the cured scaffolds at 10 min (prior to the gel point), 30 min (at the gel point), and 3 h (after the gel point) using forceps and stained with an Apoptotic & Necrotic Cell Differentiation kit. Plots of the percentage of cells undergoing apoptosis (Figure 3.6F) or necrosis (Figure 3.6G) versus time reveal that the number of cells entering apoptosis or necrosis did not change substantially versus time at 70 wt% bead loading. In contrast, at 50 wt% loading, >45% of the cells entered apoptosis or necrosis at 30 min post-mixing. For the immediate addition group, % apoptosis (or necrosis) decreased slightly at 3 h, while for the delayed addition group % apoptosis (or necrosis) continued to increase. As shown in the contour plots (Figure 3.6H-I), the percentage of cells entering apoptosis or necrosis increased with increasing reaction time and decreasing permeability. As anticipated, permeability exhibited only a modest effect on % apoptosis (or necrosis) at 10 min

post-mixing, since the scaffold had not yet formed. However, at 3 h % apoptosis increased with permeability, approaching 50% at the lowest permeability. These observations point to both chemical reaction products and scaffold permeability as key factors regulating cell survivability.

3.5 Long-term culture of encapsulated cells in vitro

The ability of BMSCs to attach to the scaffold *in vitro* was investigated for both Alg and o-Alg beads for the conditions of 70% loading and 3 min delayed addition, where cell survivability was highest. After 7 days in culture, cells (stained green with a cytoplasmic dye) remained clustered within the Alg beads, with few cells appearing adjacent or adherent to the PUR scaffold (stained blue, Figure 3.7A). In contrast, PUR scaffolds encapsulating o-Alg beads showed evidence of cell release from the beads and increasing numbers of cells lining the PUR surface. Similarly, SEM analysis revealed evidence that cells were attached to the surface of PUR scaffolds embedded with o-Alg beads (Figure 3.7B). Thus, loading the scaffold with a sufficiently high volume fraction of an o-Alg porogen to create interconnected macropores not only increased pore interconnectivity (Figure 3.6) but also supported release of cells from the beads and consequent attachment to the scaffold. To determine whether MSCs retained their pluripotency after the reaction, scaffolds with o-Alg beads were cultured in growth, adipogenic, or osteogenic medium for 21 days. Compared to cells cultured in growth medium, cells cultured in adipogenic medium showed higher oil red dye absorbance, while cells cultured in osteogenic medium showed higher alizarin red dye absorbance (Figure 3.7C). Thus, after exposure to the chemical reaction, MSCs retained their potential to differentiate to adipocytes or osteoblasts.

3.6 In vivo delivery of BMSCs encapsulated in injectable PUR scaffolds

To investigate the ability of the cells to survive the injection and generate new extracellular matrix *in vivo*, a proof-of-concept experiment was performed in full-thickness excisional skin wounds in Sprague-Dawley (SD) rats [16]. BMSCs from male SD rats were delivered to wounds in female rats, and SRY (sex determining region Y, Sox9) immunohistochemical staining was performed to track transplanted cells. PUR scaffolds embedded with Alg beads with or without cells were extruded from the wounds after 7 days (data not shown), indicating limited integration with host tissue due to slow degradation of the conventional alginate and consequent low porosity. In contrast, transplanted BMSCs (10^5 cells/ml or 2×10^4 cells/scaffold) encapsulated in o-Alg and embedded in injectable (Inj+BMSC) or implantable (Impl+BMSC) PUR scaffolds for at least 7 days (black arrows in Figure 3.8A and 3.8D). High-magnification (20X, Figure 3.8B) images from trichrome staining revealed degradation of o-Alg to form new pores throughout the scaffold (PUR, light gray), while fragments of o-Alg (A, green acellular material) remained in some of the pores. New extracellular matrix (M) was deposited in the scaffold as early as day 4. Interestingly, the Inj+BMSC group showed significantly more deposition of new matrix at both time points compared to the Inj (injectable with no cells) or the Impl+BMSC (implanted scaffold seeded with cells) groups (Fig. 3.8E). To investigate the mechanism by which transplanted BMSCs enhanced deposition of new matrix, we measured the population of $Ki67^+$ proliferating cells and deposition of Collagen IV (a marker of angiogenesis) in Inj and Inj+BMSC scaffolds by immune-histochemical staining. Inj+BMSC scaffolds showed significantly more $Ki67^+$ proliferating cells (Fig. 3.8F) and increased Collagen IV production (Fig. 3.8G) compared to Inj scaffolds. Taken

together, these observations indicate that transplanted cells not only survived the chemical reaction, but also stimulated cell proliferation and angiogenesis after transplantation *in vivo*.

A

Treatment Group	Isocyanate	FeAA wt%	Delay min	$n_{CO2,10}$ mmol cm^{-2}	Q_{10} J cm^{-2}	V_{10} %
L-0C-0	LTI-PEG	0%	0	0	0	87.7 ± 5.7
L-5C-0	LTI-PEG	0.26%	0	0.107	0.392	38.4 ± 6.4
L-5C-3	LTI-PEG	0.26%	3	0.085	0.380	66.6 ± 2.0
L-5C-6	LTI-PEG	0.26%	6	0.063	0.367	69.5 ± 4.1
H-5C-0	HDIt	0.26%	0	0.044	0.317	76.3 ± 9.0
H-10C-0	HDIt	0.52%	0	0.036	0.655	56.4 ± 11.2

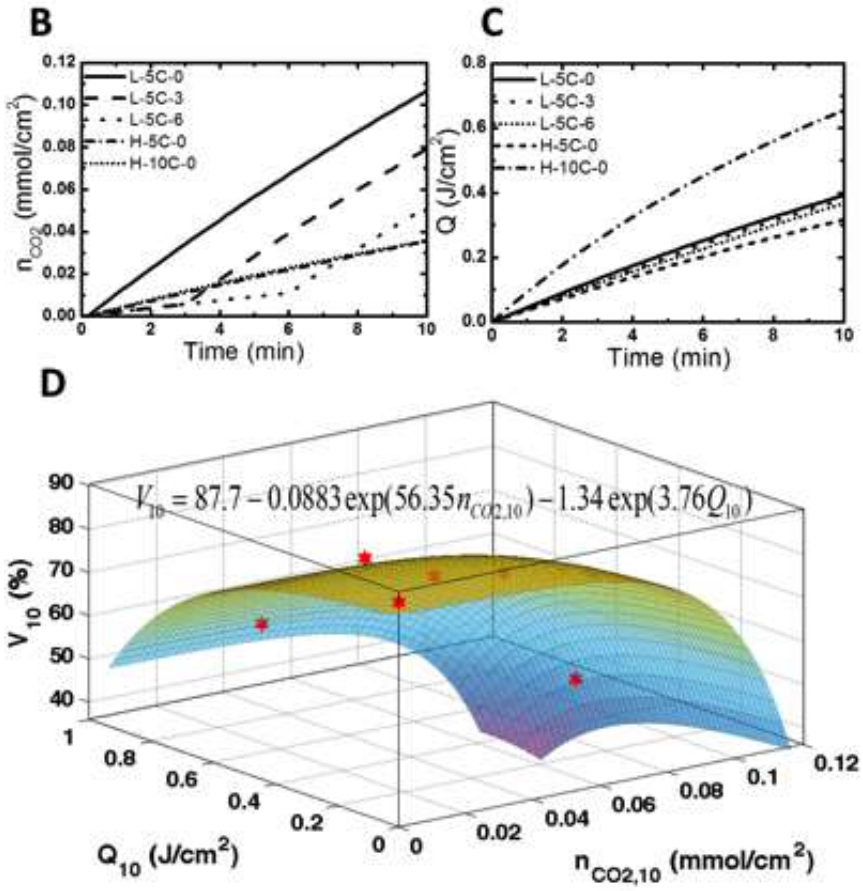

Figure 0.5 Effects of heat and CO2 released by the polyurethane reaction on viability of MSCs encapsulated in Alg beads and embedded in a reactive hydrophobic polymer at early time points.

(A) Table listing the experimental conditions, values of $n_{CO2,10}$ and Q_{10} calculated from the PUR reaction kinetics model, and measured values of cell viability at 10 min (V_{10}). (B) Plot of the moles CO_2 generated by the PUR reaction (n_{CO2}, calculated from the reaction kinetics model) as a function of time for up to 10 min. (C) Plot of the heat generated (Q, calculated from the reaction kinetics model) as a function of time for up to 10 min. (D) Contour plot showing V_{10} as a function of CO_2 ($n_{CO2,10}$) and heat (Q_{10}) generated at 10 min. Red stars represent the data points and the surface was plotted from the fit to the experimental data shown on the plot.

4.Discussion

In this study, we designed injectable PUR scaffolds for local transplantation of viable cells for tissue repair and restoration by encapsulating cells in degradable o-Alg beads prior to embedding in the reactive polymer. In contrast to hydrogels that utilize water-soluble initiators [17, 18] and macromers [19-21] to facilitate cell encapsulation from aqueous suspensions, direct encapsulation of cells in reactive hydrophobic polymers is confounded by their low (<5%) swelling in water and generation of chemical by-products and heat [7]. Two factors limited cell survivability *in vitro*: (1) generation of CO_2 and heat by the chemical reaction prior to gelation, and (2) permeability of the scaffolds after gelation. Delayed (3 min) addition of the o-Alg beads at a loading of 70% balanced the requirements for minimal exposure of cells to reaction products, high permeability for transport of nutrients and wastes, and mechanical integrity of the scaffolds. Under these conditions, PUR scaffolds injected with encapsulated BMSCs promoted increased extracellular matrix deposition *in vivo* compared to both injected acellular scaffolds and implanted

scaffolds seeded with BMSCs, and they did so without biofunctionalization of the scaffold with expensive peptides, growth factors, or other biologics.

Encapsulation of cells in Alg beads of sufficient size provided a barrier to diffusion of CO_2 and heat prior to gelation (10 min). This observation is consistent with a previous study reporting that acellular PUR scaffolds reach the reaction exotherm at 3 min post-mixing [15]. While Alg protected the cells from the chemical reaction prior to gelation, the persistence of Alg after gelation hindered attachment of cells to the scaffolds *in vitro* (Figure 3.7A-B) and tissue ingrowth *in vivo* (Figure 3.8). These observations are in agreement with a previous study reporting that cells encapsulated in Alg beads and embedded in a CPC failed to release from beads after 14 days in culture [34]. Thus, slow dissolution of Alg beads precludes the formation of interconnected macropores (>10 μm) [36, 43]. Partial oxidation to o-Alg renders it susceptible to hydrolysis [29, 44], which has prompted the use of o-Alg as a degradable carrier for MSCs. Delivery of human adipose stem cells from o-Alg hydrogels with a degradation time of ~40 days promoted generation of new adipose tissue in mice [45]. In another study, MSCs encapsulated in o-Alg beads and mixed with a calcium phosphate cement (CPC) provided mechanical protection during mixing [28, 46]. However, the utility of o-Alg as a temporary barrier to diffusion of harmful chemical reaction products, which was the subject of the present study, has not been systematically investigated.

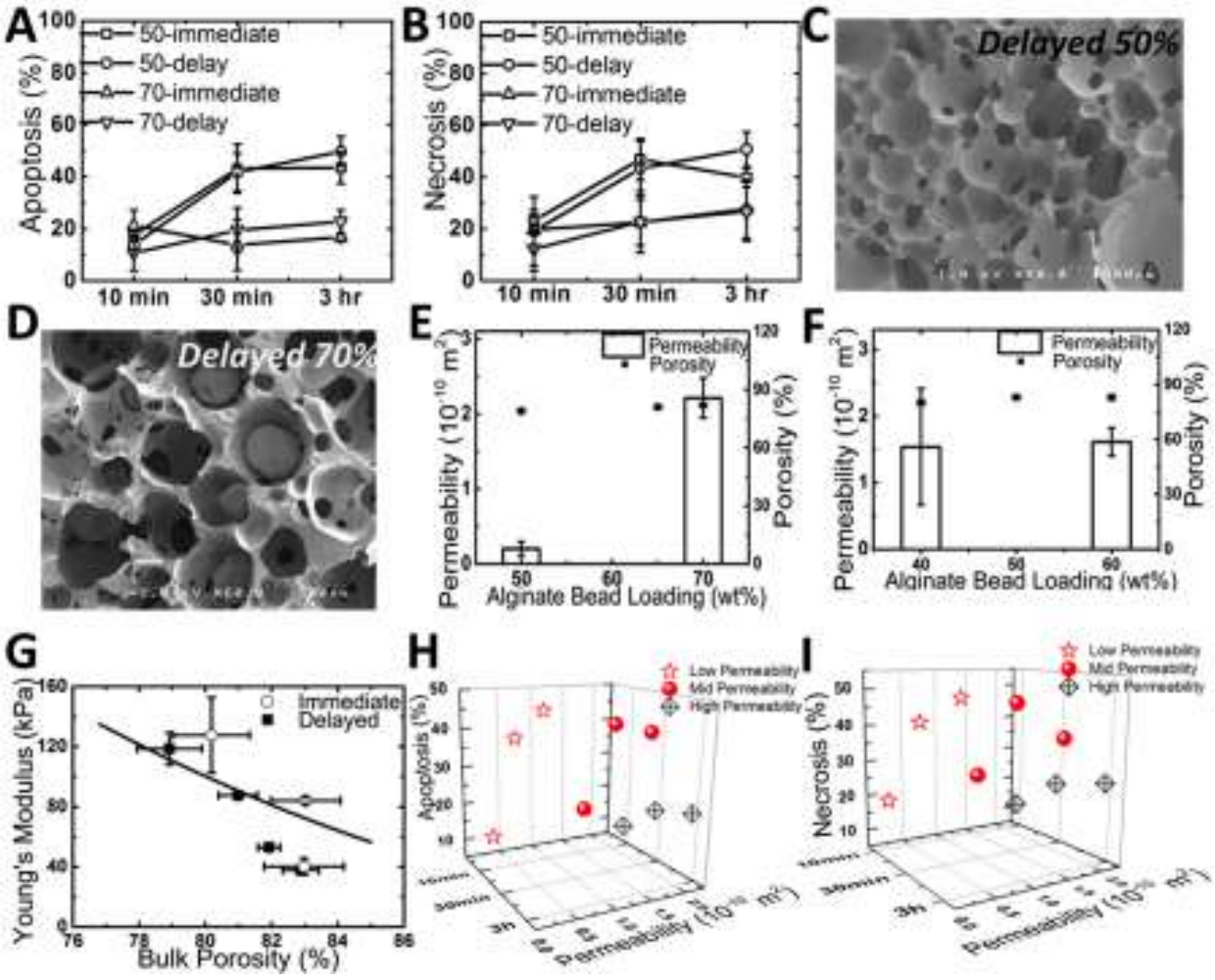

Figure 0.6 Effects of o-Alg bead loading and timing of bead addition on scaffold properties and cell viability at late time points.

(A-B) Representative SEM images of scaffolds fabricated with (A) 50 wt% beads and (B) 70 wt% beads. (C, D) Porosity and permeability of PUR scaffolds as a function of o-Alg bead loading for (C) delayed (3 min) and (D) immediate addition. (E) The elastic modulus of the scaffolds prepared by delayed and intermediate addition of beads decreased with bulk porosity. (F-G) The percentage of cells undergoing apoptosis (F) and/or necrosis (G) was measured at 10 min, 30 min, and 3 h as a function of bead loading (50 or 70 wt%) and timing of addition (immediate or delayed). (H-I) Contour plots showing the percentage of cells undergoing apoptosis (H) and/or necrosis (I) as a function of reaction time (10 min, 30 min, or 3 h) and permeability. Cell survivability decreases with increasing reaction time and decreasing permeability.

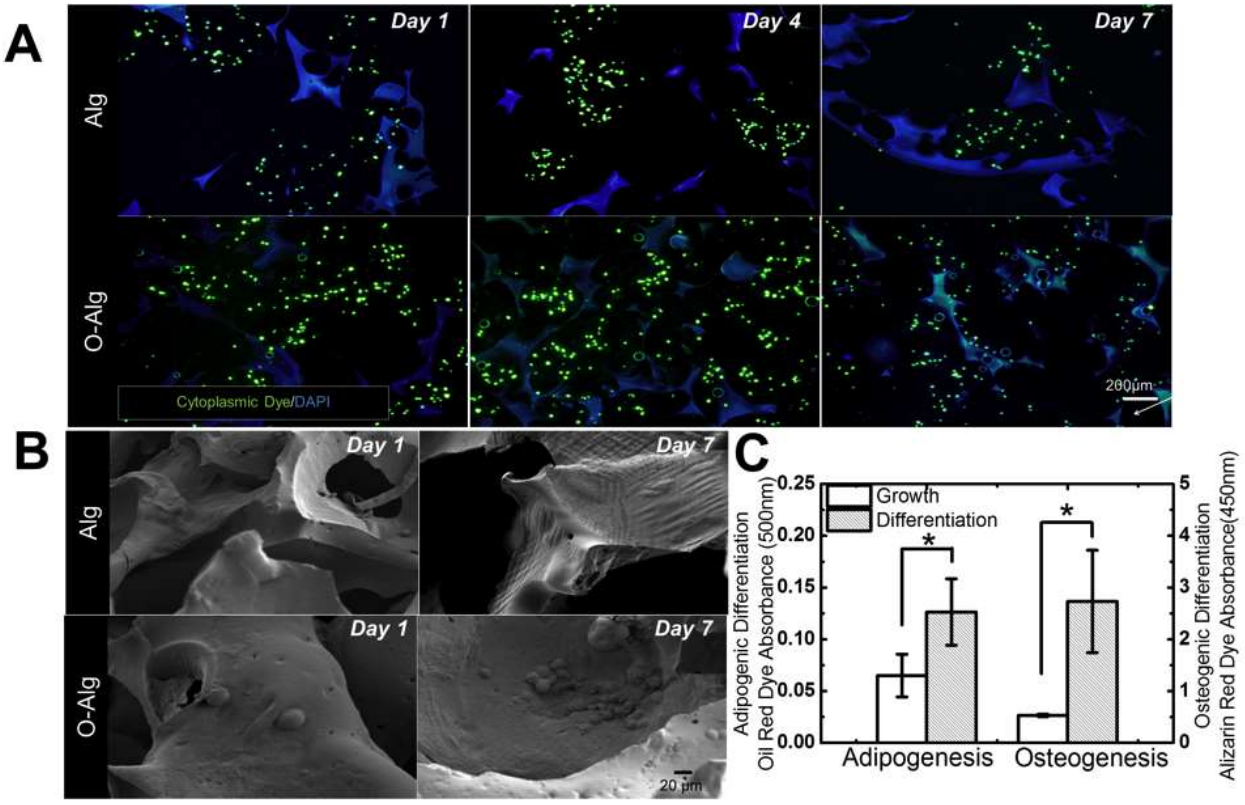

Figure 0.7 Culture of BMSCs on injectable PUR scaffolds *in vitro*.

(A) Representative histological sections stained with the cytoplasmic dye carboxyfluorescein diacetate (CFDA, green) and DAPI (blue) of PUR scaffolds loaded with 70 wt% 500 μm conventional alginate beads show viable rat BMSCs at days 1, 4, and 7. Cells are stained green and the scaffold is stained blue. Degradation of the o-Alg beads resulted in formation of macropores and subsequent attachment of rat BMSCs to the scaffold. However, even at 7 days, cells remained encapsulated in Alg beads and did not attach to the scaffold. (B) Representative SEM images of PUR scaffolds loaded with 70 wt% 500 μm o-Alg beads showed cells attached to the scaffold after 7 days, while few cells were observed for scaffolds loaded with Alg beads. (C) Osteogenic (measured by Alizarin red absorption) and adipogenic (measured by Oil red dye absorption) differentiation of BMSCs encapsulated in polyurethane foams. Cells were cultured on the scaffolds in growth, osteogenic, or adipogenic medium for 21 days, stained with Alizarin red or Oil red dye, and the dye extracted to measure absorbance.

Considering the optimal pore size of 90 – 360 μm reported for cellular infiltration and new tissue ingrowth [47], the diameter of the o-Alg beads was initially targeted at ~350 μm. However, when 350 μm beads were immediately mixed with the reactive polymer, only 30% of the cells survived at 10 min (Figure 3.4B-C). As shown in Figure 3.5D, generation of both CO_2 and heat outside the region bounded by $Q_{10} > 0.4$ J cm^{-2} and $n_{CO2,10} > 0.08$ mmol cm^{-2} (calculated at 10 min from the chemical kinetics) resulted in excessive cell death. Delayed addition of o-Alg beads reduced CO_2 generation below 0.08 mmol cm^{-2}, thereby increasing acute survivability of cells encapsulated in 500 μm beads to levels exceeding 80% (Figure 3.5D). These observations are consistent with a previous study reporting that the viability of cells encapsulated in fibrin-alginate beads embedded in an injectable CPC decreased as the concentration of $NaHCO_3$ (reacting with citric acid to produce CO_2) increased from 15 to 30% [46]. Considering that the bicarbonate-citric acid reaction is endothermic, cell death in this previous study was likely caused by CO_2.

An important unanswered question is whether the cells die in response to a cumulative increase in temperature (or CO_2 concentration) or the rate at which these parameters are changing. Quantifying the relative contributions of CO_2 and heat generation to cell death both prior to and after gelation requires solution of the unsteady state heat conduction and CO_2 diffusion equations for both Alg (A) and polymer (PUR) phases [48]:

$$\frac{\partial T_A}{\partial t} = a_A \nabla^2 T_A$$
$$\frac{\partial T_{PUR}}{\partial t} = a_{PUR} \nabla^2 T_{PUR} + \frac{Q(t)}{r_{PUR} C_{p,PUR}} \quad (7)$$
$$\frac{\partial c_{CO_2,A}}{\partial t} = D_{CO_2,A} \nabla^2 c_{CO_2,A}$$
$$\frac{\partial c_{CO_2,A}}{\partial t} = D_{CO_2,A} \nabla^2 c_{CO_2,A} + r_{CO_2,PUR}$$

where $\alpha = \kappa/\rho C_p$ is the thermal diffusivity, κ is the thermal conductivity, C_p is the heat capacity, $Q(t)$ is the heat generated by the chemical reaction (Eq. 4), c_{CO2} is the concentration of carbon dioxide, and D_{CO2} is the diffusivity of CO_2. While the exact solution of unsteady state heat conduction and CO_2 diffusion equations is outside the scope of this study, several observations can be made from the apoptosis/necrosis kinetic data (Figure 3.6H-I). The percentage of cells entering apoptosis or necrosis increased from 10 min to 3 h for all scaffolds, including highly permeable ($>2\times10^{-10}$ m^2) scaffolds with minimal transport limitations, suggesting that the cells did not recover from the initial exposure to heat and CO_2. Furthermore, the percentage of cells entering apoptosis or necrosis was comparable at all time points and permeabilities. The majority of damaged cells stained positive for both apoptotic and necrotic markers, which further confirms that cells did not recover from the initial exposure to reaction products. Finally, cell survival after gelation (30 min – 3 h) improved dramatically in highly permeable ($>2\times10^{-10}$ m^2) scaffolds. These observations suggest that exposure to heat and CO_2 regulates cell survival prior to gelation, while scaffold permeability controls cell survival after gelation.

While delayed (3 min) addition of o-Alg beads reduced exposure of cells to CO_2, the extent of gas foaming can be controlled by tuning the gel:blow (k_G/k_B) ratio. For the LTI-PEG

prepolymer and FeAA catalyst used in this study, the gel:blow ratio was 6.4 (Table 1), which is substantially greater than the value of ~0.05 reported for a triethylene diamine catalyst [7] but not large enough to obviate the need for delayed addition of the beads. In contrast, HDIt exhibited a gel:blow ratio of 13.4 at the lowest catalyst level (Table 1), which was sufficiently high that delayed addition of the beads was not required to achieve high viability. These observations point to the gel:blow ratio as a key parameter for maintaining high cell survivability without delayed addition of the beads and is the focus of ongoing studies.

In a proof-of-concept *in vivo* experiment, injected scaffolds showed comparable cell survival to implanted scaffolds (Figure 3.8D). However, the Inj+BMSC group showed significantly more new granulation tissue compared to both the Impl+BMSC and Inj (no cells) groups (Figure 3.8E). To investigate the mechanism by which transplanted BMSCs enhanced healing, we measured the number of $Ki67^+$ proliferating cells and area% Collagen IV by histomorphometry. The number density of $Ki67^+$ cells was significantly higher in the Inj+BMSC group compared to the Inj group on days 4 and 7 (Figure 3.8F). Furthermore, the area% Collagen IV was significantly higher in the Inj+BMSC group on days 7 and 14, despite the fact that the transplanted cells survived for only 7 days. These observations are consistent with the notion of trophic activity, by which MSCs influence healing by the secretion of growth factors and cytokines that stimulate proliferation of tissue-intrinsic progenitor cells as well as angiogenesis [49, 50]. Using this adaptable and versatile technique, BMSCs can be encapsulated in o-Alg beads directly after harvesting, mixed with the two-component PUR, and injected into defects of varying sizes and complex shapes.

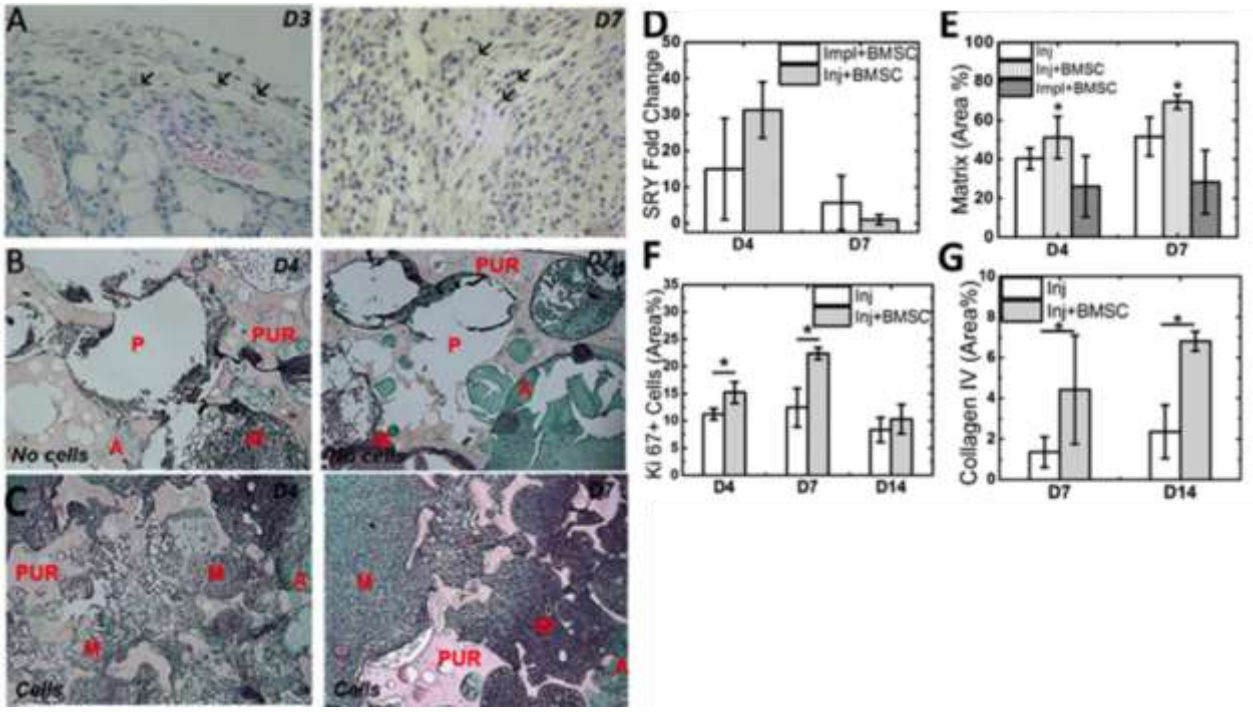

Figure 0.8 Rat BMSCs encapsulated in 500 μm o-Alg beads embedded in a PUR scaffold survive transplantation and enhance deposition of new extracellular matrix in a rat excisional wound model.

(A) SRY (sex determining region Y, Sox9) immunohistochemical staining revealed the presence of male donor rat BMSCs in wounds on female rats (black arrows) at day 7 (40X magnification). (B-C) High-magnification (20X) images of histological sections of PUR scaffolds injected into 10-mm excisional wounds in rats without (B) or with (C) 10^5 rat BMSCs/ml encapsulated in o-Alg beads at 7 days show that local cell delivery increases deposition of new extracellular matrix (M). O-Alg beads (A) degraded to form macropores (P), resulting in infiltration of cells and ingrowth of granulation tissue along the surface of the residual polyurethane (PUR). (D) qRT-PCR measurements of SRY expression show that cells survive for up to 7 days in implanted (Impl+BMSC) and injected (Inj+BMSC) scaffolds. (E) Histomorphometric analysis showed that Inj+BMSC scaffolds supported significantly greater ingrowth of extracellular matrix (E) at days 4 and 7 compared to the injected acellular (Inj) and cellular implant (Impl+BMSC) controls. (F-G) $Ki67^+$ proliferating cells (F) and Collagen IV (G) are higher in Inj+BMSC scaffolds at days 4 and 7 compared to the acellular Inj control. * denotes significant differences between the blank and BMSC groups, $p < 0.05$.

5.Conclusion

Injectable PUR scaffolds embedded with bone marrow-derived MSCs encapsulated in o-Alg were designed to promote peripheral tissue infiltration in rat subcutaneous wound model. MSCs were encapsulated in o-Alg before the PUR reaction to enhance cell survivability. After incorporation, o-Alg beads subsequently degraded to form interconnected macropores that supported cellular migration, proliferation, and deposition of new extracellular matrix *in vitro* and *in vivo*. These properties underscore the potential utility of PUR scaffolds as a versatile, clinically-translatable, and functionally-significant injectable cell delivery system for regenerative medicine applications.

Acknowledgments

The authors acknowledge Frank Rauh at FMC Novamatrix for helpful discussions on preparation of partially oxidized alginate. Financial support was provided by the Orthopaedic Extremity Trauma Research Program (DOD W81XWH-07-1-0211), the National Institute of Arthritis and Musculoskeletal and Skin Diseases (AR056138), and the Department of Veterans Affairs. The content is solely the responsibility of the authors and does not necessarily represent the official views of the National Institutes of Health or the Department of Veterans Affairs.

Reference:

[1] Burdick JA, Anseth KS. Photoencapsulation of osteoblasts in injectable RGD-modified PEG hydrogels for bone tissue engineering. Biomaterials 2002;23:4315-23.
[2] Cleland JG, Coletta AP, Abdellah AT, Cullington D, Clark AL, Rigby AS. Clinical trials update from the American Heart Association 2007: CORONA, RethinQ, MASCOT, AF-CHF, HART, MASTER, POISE and stem cell therapy. European journal of heart failure 2008;10:102-8.
[3] Horwitz EM, Prockop DJ, Fitzpatrick LA, Koo WW, Gordon PL, Neel M, et al. Transplantability and therapeutic effects of bone marrow-derived mesenchymal cells in children with osteogenesis imperfecta. Nat Med 1999;5:309-13.
[4] Orlic D, Kajstura J, Chimenti S, Jakoniuk I, Anderson SM, Li B, et al. Bone marrow cells regenerate infarcted myocardium. Nature 2001;410:701-5.
[5] Salinas CN, Anseth KS. Mesenchymal stem cells for craniofacial tissue regeneration: designing hydrogel delivery vehicles. J Dent Res 2009;88:681-92.
[6] Kretlow JD, Klouda L, Mikos AG. Injectable matrices and scaffolds for drug delivery in tissue engineering. Advanced Drug Delivery Reviews 2007;59:263 - 73.
[7] Page JM, Prieto EM, Dumas JE, Zienkiewicz KJ, Wenke JC, Brown-Baer P, et al. Biocompatibility and chemical reaction kinetics of injectable, settable polyurethane/allograft bone biocomposites. Acta Biomater 2012;8:4405-16.
[8] Nguyen KT, West JL. Photopolymerizable hydrogels for tissue engineering applications. Biomaterials 2002;23:4307-14.
[9] Guelcher SA, Srinivasan A, Dumas JE, et al. Synthesis, mechanical properties, biocompatibility, and biodegradation of polyurethane networks from lysine polyisocyanates. Biomaterials 2008;29:1762-75.
[10] Zhang J-Y, Beckman EJ, Piesco NJ, Agarwal S. A new peptide-based urethane polymer: synthesis, biodegradation, and potential to support cell growth in vitro. Biomaterials 2000;21:1247-58.
[11] Hafeman AE, Zienkiewicz KJ, Zachman AL, Sung HJ, Nanney LB, Davidson JM, et al. Characterization of the degradation mechanisms of lysine-derived aliphatic poly(ester urethane) scaffolds. Biomaterials 2011;32:419-29.
[12] Martin JR, Gupta MK, Page JM, Yu F, Davidson JM, Guelcher SA, et al. A porous tissue engineering scaffold selectively degraded by cell-generated reactive oxygen species. Biomaterials 2014;35:3766-76.
[13] Hafeman A, Li B, Yoshii T, Zienkiewicz K, Davidson J, Guelcher S. Injectable biodegradable polyurethane scaffolds with release of platelet-derived growth factor for tissue repair and regeneration. Pharm Res 2008;25:2387-99.
[14] Guelcher SA. Biodegradable polyurethanes: synthesis and applications in regenerative medicine. Tissue Eng B: Reviews 2008;14:3 - 17.

[15] Guelcher S, Srinivasan A, Hafeman A, Gallagher K, Doctor J, Khetan S, et al. Synthesis, In vitro degradation, and mechanical properties of two-component poly(ester urethane)urea scaffolds: Effects of water and polyol composition. Tissue Engineering 2007;13:2321-33.
[16] Adolph EJ, Hafeman AE, Davidson JM, Nanney LB, Guelcher SA. Injectable polyurethane composite scaffolds delay wound contraction and support cellular infiltration and remodeling in rat excisional wounds. J Biomed Mater Res A 2012;100A:450-61.
[17] Mann BK, Gobin AS, Tsai AT, Schmedlen RH, West JL. Smooth muscle cell growth in photopolymerized hydrogels with cell adhesive and proteolytically degradable domains: synthetic ECM analogs for tissue engineering. Biomaterials 2001;22:3045-51.
[18] Bryant SJ, Nuttelman CR, Anseth KS. Cytocompatibility of UV and visible light photoinitiating systems on cultured NIH/3T3 fibroblasts in vitro. J Biomater Sci Polym Ed 2000;11:439-57.
[19] Kim IS, Jeong YI, Kim SH. Self-assembled hydrogel nanoparticles composed of dextran and poly(ethylene glycol) macromer. Int J Pharm 2000;205:109-16.
[20] Martens P, Anseth KS. Characterization of hydrogels formed from acrylate modified poly(vinyl alcohol) macromers. Polymer 2000;41:7715-22.
[21] Bulpitt P, Aeschlimann D. New strategy for chemical modification of hyaluronic acid: preparation of functionalized derivatives and their use in the formation of novel biocompatible hydrogels. J Biomed Mater Res 1999;47:152-69.
[22] Kloxin AM, Kloxin CJ, Bowman CN, Anseth KS. Mechanical properties of cellularly responsive hydrogels and their experimental determination. Adv Mater 2010;22:3484-94.
[23] Boerckel JD, Kolambkar YM, Dupont KM, Uhrig BA, Phelps EA, Stevens HY, et al. Effects of protein dose and delivery system on BMP-mediated bone regeneration. Biomaterials 2011;32:5241-51.
[24] Phelps EA, Enemchukwu NO, Fiore VF, Sy JC, Murthy N, Sulchek TA, et al. Maleimide cross-linked bioactive PEG hydrogel exhibits improved reaction kinetics and cross-linking for cell encapsulation and in situ delivery. Adv Mater 2012;24:64-70, 2.
[25] Lutolf MP, Lauer-Fields JL, Schmoekel HG, Metters AT, Weber FE, Fields GB, et al. Synthetic matrix metalloproteinase-sensitive hydrogels for the conduction of tissue regeneration: engineering cell-invasion characteristics. Proc Natl Acad Sci U S A 2003;100:5413-8.
[26] Hwang CM, Sant S, Masaeli M, Kachouie NN, Zamanian B, Lee SH, et al. Fabrication of three-dimensional porous cell-laden hydrogel for tissue engineering. Biofabrication 2010;2:035003.
[27] Scott EA, Nichols MD, Kuntz-Willits R, Elbert DL. Modular scaffolds assembled around living cells using poly(ethylene glycol) microspheres with macroporation via a non-cytotoxic porogen. Acta Biomater 2010;6:29-38.
[28] Tang M, Chen W, Weir MD, Thein-Han W, Xu HH. Human embryonic stem cell encapsulation in alginate microbeads in macroporous calcium phosphate cement for bone tissue engineering. Acta Biomater 2012;8:3436-45.

[29] Bouhadir KH, Lee KY, Alsberg E, Damm KL, Anderson KW, Mooney DJ. Degradation of partially oxidized alginate and its potential application for tissue engineering. Biotechnol Prog 2001;17:945-50.
[30] Moghadam H, Samimi M, Samimi A, Khorram M. Electro-spray of high viscous liquids for producing mono-sized spherical alginate beads. Particuology 2008;6:271-5.
[31] Guelcher SA, Patel V, Gallagher KM, Connolly S, Didier JE, Doctor JS, et al. Synthesis and in vitro biocompatibility of injectable polyurethane foam scaffolds. Tissue Engineering 2006;12:1247-59.
[32] Dumas JE, Zienkiewicz K, Tanner SA, Prieto EM, Bhattacharyya S, Guelcher S. Synthesis and Characterization of an Injectable Allograft Bone/polymer Composite Bone Void Filler with Tunable Mechanical Properties. Tissue Eng Part A 2010;16:2505-18.
[33] Zhao W, Fierro V, Pizzi A, Du G, Celzard A. Effect of composition and processing parameters on the characteristics of tannin-based rigid foams. Part II: Physical properties. Materials Chemistry and Physics 2010;123:210-17.
[34] Zhao L, Weir MD, Xu HH. An injectable calcium phosphate-alginate hydrogel-umbilical cord mesenchymal stem cell paste for bone tissue engineering. Biomaterials 2010;31:6502-10.
[35] Guvendiren M, Lu HD, Burdick JA. Shear-thinning hydrogels for biomedical applications. Soft Matter 2012;8:260-72.
[36] Bencherif SA, Sands RW, Bhatta D, Arany P, Verbeke CS, Edwards DA, et al. Injectable preformed scaffolds with shape-memory properties. Proc Natl Acad Sci U S A 2012;109:19590-5.
[37] Bohner M. Design of ceramic-based cements and putties for bone graft substitution. Eur Cell Mater 2010;20:1-12.
[38] Sperling LH. Introduction to Physical Polymer Science. 3rd ed. New York: Wiley-Interscience; 2001.
[39] Oertel G. Polyurethane Handbook. 2nd ed. Berlin: Hanser Gardner Publications; 1994.
[40] Parnell S, Min K, Cakmak M. Kinetic studies of polyurethane polymerization with Raman spectroscopy. Polymer 2003;44:5137-44.
[41] Lovering EG, Laidler KJ. Thermochemical Studies of Some Alcohol-Isocyanate Reactions. Canadian Journal of Chemistry 1962;40:26-30.
[42] Gibson LJ, Ashby MF. Cellular solids: Structure and properties: Cambridge University Press; 1997.
[43] Han LH, Lai JH, Yu S, Yang F. Dynamic tissue engineering scaffolds with stimuli-responsive macroporosity formation. Biomaterials 2013;34:4251-8.
[44] Boontheekul T, Kong HJ, Mooney DJ. Controlling alginate gel degradation utilizing partial oxidation and bimodal molecular weight distribution. Biomaterials 2005;26:2455-65.
[45] Kim WS, Mooney DJ, Arany PR, Lee K, Huebsch N, Kim J. Adipose tissue engineering using injectable, oxidized alginate hydrogels. Tissue Eng Part A 2012;18:737-43.
[46] Chen W, Zhou H, Tang M, Weir MD, Bao C, Xu HH. Gas-foaming calcium phosphate cement scaffold encapsulating human umbilical cord stem cells. Tissue Eng Part A 2012;18:816-27.

[47] Wang H, Pieper J, Peters F, van Blitterswijk CA, Lamme EN. Synthetic scaffold morphology controls human dermal connective tissue formation. J Biomed Mater Res A 2005;74:523-32.
[48] Bird R, Stewart W, Lightfoot E. Transport Phenomena. New York: Wiley; 1960.
[49] Caplan AI, Dennis JE. Mesenchymal stem cells as trophic mediators. J Cell Biochem 2006;98:1076-84.
[50] Caplan AI. Why are MSCs therapeutic? New data: new insight. The Journal of pathology 2009;217:318-24.

CHAPTER 4

SUBSTRATE MODULUS AND PORE SIZE OF 3D SCAFFOLDS FABRICATED BY TEMPLATED FUSED DEPOSITION MODELING REGULATE OSTEOGENIC DIFFERENTIATION

1. Introduction

The properties of the extracellular matrix, including elastic modulus, porosity, pore size, and curvature, are known to regulate cell fate in a number of physiological processes, including tissue repair and restoration as well as disease progression. Biomimetic 3D *in vitro* systems have been proposed for investigating interactions between cell populations and the microenvironment (MEN), identifying the molecular mechanisms of healing and/or disease progression, and screening drugs.[1] Consequently, new biomaterials re-capitulating the bone MEN are critical for understanding the spatio-temporal dynamics of bone remodeling as well as how bone cells integrate mechanical and chemical signals over multiple length scales. While Additive Manufacturing (AM) approaches such as Fused Deposition Modeling (FDM) enable precise control over topological properties[2], the limited number of materials that can be processed by AM techniques precludes precise control over mechanical properties. Here, we fabricated 3D scaffolds with substrate moduli ranging from the basement membrane to the low end of cortical bone (10 – 900 MPa[3, 4]) and pore sizes in the range that supports enhanced bone formation and vascularization (>300 μm[5, 6]) using a new templated-Fused Deposition Modeling (t-FDM) process. Previous studies have reported that osteogenic differentiation of mesenchymal stem cells (MSCs) increases with substrate modulus up to about 100 kPa.[7] However, it has been

suggested that above this range cells are in an isometric state of contraction and cannot respond to further increases in rigidity.[8, 9] Surprisingly, we found that osteogenic differentiation and mineralization of MSCs increased with increasing substrate modulus in the MPa range and decreasing pore size.

A limited number of studies have investigated the effects of the elastic modulus on osteogenic differentiation on rigid substrates approximating trabecular bone (100 – 400 MPa[3]). Expression of the osteogenic transcription factor *Runx2* and the osteoblast marker alkaline phosphatase (*ALP*) increased with 2D substrate rigidity when MC3T3-E1 pre-osteoblasts were cultured on PEG-diacrylate hydrogels (600 kPa) or tissue culture polystyrene (2000 MPa).[10] RhoA activity increased on stiffer substrates, thereby promoting increased cellular contractility through ROCK. A later study reported that for 2D acrylate films with moduli ranging from 5–850 MPa, the composition of the polymer had a more significant effect on differentiation than the substrate modulus.[3] Curvature, pore size, and pore shape have also been reported to affect the rate of new bone formation. A recent study has reported that new bone formation is enhanced on concave versus convex or flat surfaces.[11] Cells respond to radii of curvature larger than themselves, and the magnitude of the contractile forces and the rate of new bone formation have been suggested to increase with the degree of curvature of the surface.[12, 13] This increasing osteogenic potential with decreasing scaffold pore size has been attributed in part to mechanical forces[12], since smaller pores with a higher degree of curvature may result in increased stress concentration.[13] Thus, the effects of substrate modulus and pore size on osteogenesis may be inter-related. While previous studies point to elastic modulus, pore size, and pore shape as determinants of osteogenic

differentiation, the relative contributions of these mechanical and topological properties to osteogenic differentiation have not been fully elucidated. A more fundamental understanding of how the properties of the matrix direct osteogenesis would guide the rational design of cell-responsive scaffolds that recapitulate the bone MEN for restoration and repair of bone damaged by trauma or disease.

2. Results

To fabricate t-FDM scaffolds with well-defined topological properties approximating those of rod-like trabecular bone, polylactic acid (PLA) templates were designed using Auotodesk software and fabricated by Fused Deposition Modeling (FDM) with a MakerBot® Replicator 2 3D printer (**Figure 4.1A**). PLA templates were printed with 100% inter-connected nominal 300 μm (Figure 1B) or 500 μm (Figure 4.1C) fibers. Measured PLA fiber sizes were 423 +/- 34 and 557 +/- 44 μm for nominal 300 and 500 μm templates, respectively (Figure 4.1D). The reactive polyurethane (PUR), which comprised hexamethylene diisocyanate trimer (HDIt), a polyester triol (300 (Rigid, R) or 3000 (Compliant, C) g mol^{-1}), and iron acetylacetonate (FeAA) catalyst, was mixed and poured into the PLA template. The catalyst concentration was adjusted to maintain the reactive PUR as a fluid for a sufficient period of time required to fill the inter-fiber space. After curing overnight, PLA fibers were leached from the scaffolds by immersion in dichloromethane for 18h to form inter-connected pores in the PUR scaffolds, while the inter-fiber space was filled with PUR (Figure 4.1E). To determine the effects of scaffold processing on PUR properties, 2D PUR films were also synthesized by casting in well plates. The contact angles measured for rigid (R) and

compliant (C) PUR films did not show significant differences between groups, indicating similar surface chemistry for protein adsorption and consequent cell adhesion (Figure 4.1F).

The ratio of fiber diameter:inter-fiber spacing was maintained at 1:1 in order to provide relatively constant porosity (46 +/- 4% to 52 +/- 2%) and ~100% inter-connected pores across scaffold groups. Scaffold modulus was controlled by synthesizing PUR scaffolds from polyester triols of different molecular weight (300 or 3000 g mol^{-1}). The Young's modulus of the polymeric substrate (E_s) was measured by nanoindentation using the method of Oliver and Pharr.[14] Values of E_s for 2D films and 3D scaffolds were anticipated to be comparable, since they were synthesized from the same polymer. While the values of E_s matched for compliant films and scaffolds, the substrate modulus of the rigid PUR scaffolds was ~30% less than that of the films (Figure 4.1G). The bulk moduli of both the 2D films (K) and 3D scaffolds (K^*) were also measured under compression by MTS.[15] The 3D scaffold bulk modulus was calculated (K^*_{pred}) from measured values of K, polymer density (ρ = 1.27 g cm^{-3}), and scaffold porosity ε[16]:

$$K^*_{pred} = K\left(\frac{1-\varepsilon}{3}\right)^2 \quad (1)$$

Experimental and predicted values of K^* for the 3D scaffolds are compared in Figure 4.1H. For all groups, the measured bulk moduli of the 3D scaffolds were statistically the same as the values calculated from the bulk moduli of 2D films using Equation (1). Taken together, the nanoindentation and bulk modulus experiments show that the substrate modulus for each polymer (rigid or compliant) is similar in 2D and 3D, and that the substrate modulus of the rigid scaffolds is significantly higher than that of the compliant scaffolds.

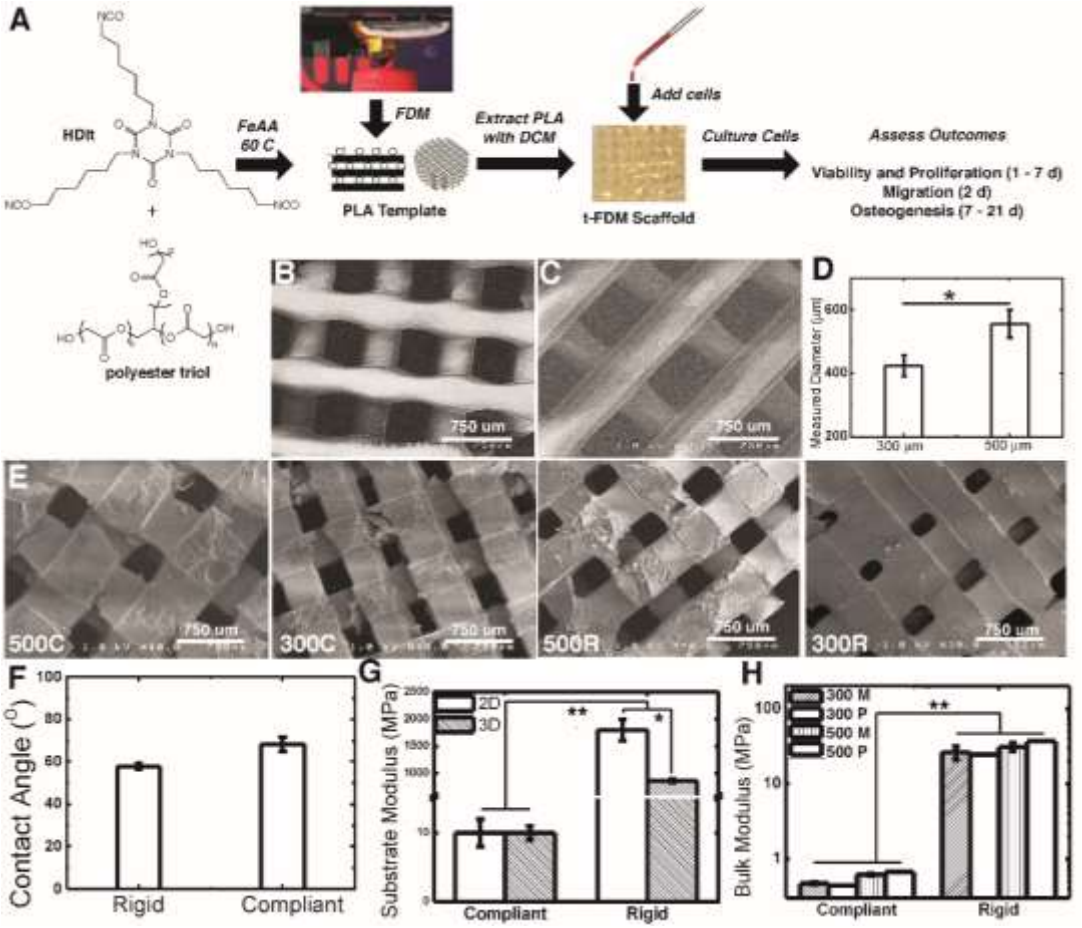

Figure 0.1 Fabrication and characterization of 3D scaffolds with tunable elastic moduli and pore size by template Fused Deposition Modeling (t-FDM).

(A) Hexamethylene diisocyanate trimer (HDIt) was mixed with a polyester triol and iron acetylacetonate (FeAA) catalyst and poured into a poly(lactic acid) (PLA) template fabricated by a MakerBot® Replicator 2 3D printer. After curing overnight, the PLA template was dissolved in dichloromethane for 18 h. After washing with DI water, cells were cultured on the scaffolds. (B-C) SEM images of the nominal (B) 300 and (C) 500 µm PLA templates. (D) Size of PLA fibers in the scaffolds measured by SEM. (E) SEM images of 500C, 300C, 500R, and 300R scaffolds. (F) Water contact angle measured for 2D compliant (C) and rigid (R) films. (G) Substrate modulus of 2D rigid films (2D-R) and 3D scaffolds (300-C and 300-R) measured by nanoindentation shows. (F) Comparison of scaffold bulk modulus K^* measured under compression and predicted (K^*_{pred}) from the bulk modulus of the 2D films and cellular solids theory. * $p < 0.05$, ** $p < 0.01$.

Cell culture experiments were performed to investigate the effects of elastic modulus and pore size on adhesion, proliferation, and differentiation of bone marrow-derived mesenchymal stem cells (BMSCs). Rat BMSCs were suspended in complete cell culture medium, seeded onto scaffolds (10^5 cells cm^{-3} scaffold), and cultured at 37°C for 24 h. Adhered cells imaged by scanning electron microscopy (SEM) were well spread on all four scaffolds (**Figure 4.2A**), which is consistent with the notion that cells cannot deform substrates with elastic moduli exceeding 100 kPa.[8, 9] To investigate the effects of modulus and pore size on viability, live/dead staining, total protein assays, and metabolic assays were performed. Minimal (<5%) cell death was detected 48 h after cell seeding in all four groups (Figure 4.2B), indicating that the scaffolds are non-cytotoxic. Cell proliferation was assessed by total protein and metabolic assays. While total protein increased from day 1 to day 7 for all treatment groups (Figure 4.2C), differences between groups were not significant, which suggests that modulus and pore size have minimal effects on proliferation. In contrast, the metabolism level of BMSCs cultured in rigid scaffolds was significantly higher than that observed for compliant scaffolds at each time point, while pore size effects were not significant (Figure 4.2D). These observations suggest that cells are more metabolically active on rigid substrates, which was conjectured to promote increased cell migration. Two assays were performed to assess the effects of substrate modulus on migration of BMSCs. Live cell tracking[17] on 2D rigid and compliant PUR films showed that BMSCs migrated faster on rigid films (Figure 4.2E). Due to technical challenges associated with tracking cells in 3D, trans-well invasion experiments[18] were performed using 3D scaffolds, which showed that cells migrated faster on rigid scaffolds, although differences for 500 μm scaffolds were not significant (Figure 4.2F-G). These findings

suggest that metabolism and migration of BMSCs at early time points after seeding (< 7 days) are primarily controlled by the substrate modulus.

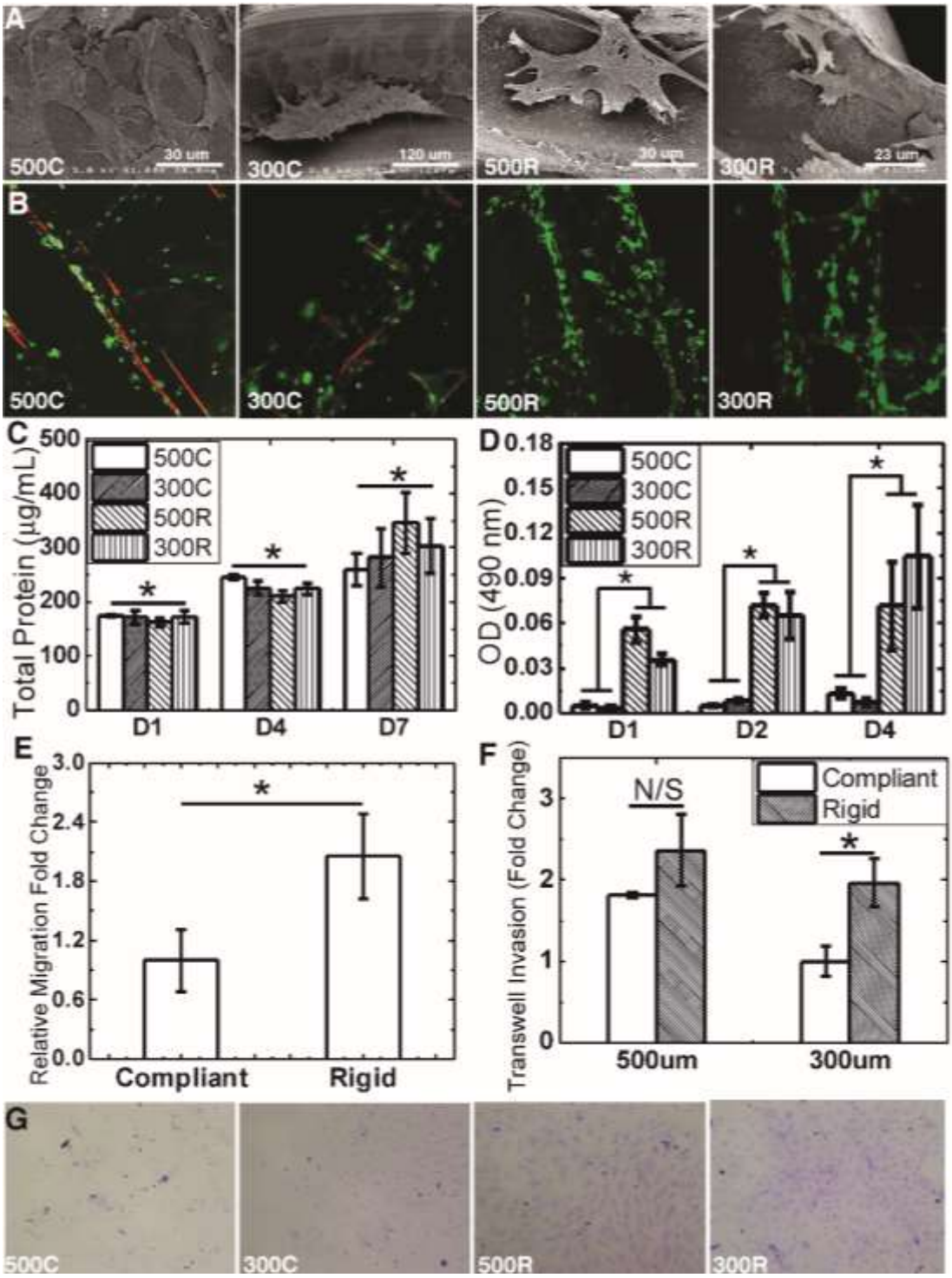

Figure 0.2 Effects of elastic modulus and pore size on cellular attachment, proliferation, and migration.

(A) SEM images of adherent MSCs show minimal differences in morphology as a function of scaffold properties. (B) Live (green)/dead (red) staining (10x) shows no effects of substrate modulus or pore size on the viability of adherent MSCs. (C) Measurements of total protein on D1, 4, and 7 show no significant differences in cell proliferation as a function of elastic modulus or pore size. (D) Assessment of cell metabolic activity by the MTS assay shows significantly higher activity on rigid scaffolds. (E) Live-cell tracking measurements showed that BMSC migration increased on rigid 2D films. (F) 3D migration of BMSCs, as assessed by an invasion assay, increased with increasing substrate modulus and decreasing pore size. (G) Images of cells stained with crystal violet (10x) that migrated through the scaffolds to the well plate in the invasion assay. * $p < 0.05$.

Rat BMSCs were cultured in ostegenic medium (complete cell culture medium supplemented with 10 nM dexamethasone, 50 μg ml^{-1} ascorbic acid, and 0.1 mM β- glycerophosphate) for up to 21 days and total RNA extracted to quantify expression of osteogenic genes at D5, 10 and 15. Expression of the transcription factor *Runx2*[19] was assessed by quantitative real-time PCR (qPCR) to investigate the effects of scaffold properties on osteogenic differentiation of BMSCs. While the effects of pore size on expression of *Runx2* were not significant, *Runx2* was significantly up-regulated on rigid scaffolds at 5 and 15 days (**Figure 4.3A**). Expression of *Collagen-1* (*Col-1*) and *Fibronectin* (*Fn*) has been reported to be necessary for osteogenic differentiation[20] and was also evaluated in this study. Significant increases in gene expression were only observed on D5, with increased *Col-1* expression observed for 500-R and 300-R (Figure 4.3B) and increased *Fn* expression observed for 300-R (Figure 4.3C). These observations point to an early cellular

response to substrate rigidity that drives increased production of extracellular matrix proteins to support osteogenic differentiation of BMSCs.[21] Expression of *Osteopontin* (*OPN*), a prominent component of the mineralized extracellular matrix in bone and a marker of osteogenic differentiation[22], was also evaluated in this study. *OPN* expression was significantly higher on rigid scaffolds at D10 and D15 (Figure 4.3D). Expression was significantly higher on 300-R compared to 500-R scaffolds on D10, but the effects of pore size on *OPN* expression were insignificant on D15.

Since the ability to mineralize the extracellular matrix is an important late-stage marker of osteogenic differentiation, mineralization was assessed by the deposition of aggregated mineral nodules. Cells were fixed, stained for nodular aggregates at D21 by Alizarin Red S[23], the adsorbed dye extracted from the scaffolds with 5% SDS solution[24], and the absorbance of the extract measured at 550 nm. Consistent with the gene expression data, Alizarin Red S absorbance increased with scaffold rigidity (Figure 4.3E), indicating up-regulated mineralization on the rigid scaffolds. Interestingly, mineralization also significantly increased with decreasing pore size. Another group of scaffolds were fixed at D21, sectioned (5 μm), and stained with Alizarin Red S. A greater number of mineralized nodules were observed on the rigid compared to compliant scaffolds (Figure 4.3F). Furthermore, SEM images of mineralized extracellular matrix at D21 (Fig. 4.3G) showed larger and more extensive formation of mineral nodules on 300-R compared to the other scaffolds. Taken together, the gene expression and mineralization experiments show that ostegenic differentiation was highest on the rigid scaffolds with bone-like substrate modulus and 423 μm pores, which challenges the notion that cells adhered to substrates with moduli

exceeding 100 kPa are in an isometric state of contraction. Considering that cells cannot displace substrates with moduli greater than about 10 kPa[9], an alternative mechanotransduction mechanism, such as coupling of an integrin and soluble factor receptor[25], is conjectured to promote the observed increased osteogenesis on rigid bone-like substrates.

3. Discussion

There are a limited number of studies investigating the effects of scaffold substrate modulus and pore size on osteogenic differentiation using AM approaches that enable precise control over mechanical and topological properties.[2] Our observation that mineralization increased with decreasing pore size is consistent with a recent study reporting that scaffolds fabricated by selected laser melting (another AM technique) with 500 μm pores enhanced cellular response compared to 1000 μm.[26] Interestingly, the majority of *in vivo* studies have reported enhanced new bone formation in scaffolds with larger pore sizes.[2, 6, 27] Thus, while effects such as stress concentration[13] may increase osteogenic potential in scaffolds with smaller pores *in vitro*, the relative contributions of phenomena such as reduced transport[28] and initiation of new bone formation through a chondrogenic pathway[27, 29] may be more important *in vivo*. The topology of the scaffold may also affect osteogenesis and new bone formation. Trabecular bone exhibits both rod- and plate-like structures, and thus the degree of curvature varies spatially within the bone.[30] Furthermore, the relative portions of rods and plates, which is quantified by the Structure Model Index (SMI) describing the trabecular architecture[30], varies from one anatomic site to another. Thus, further *in vivo* studies are needed to identify how new bone formation is controlled by

substrate pore size, pore shape, and surface curvature, which can be precisely controlled by templated AM techniques.

In this study, we designed a new t-FDM process to fabricate 3D scaffolds with tunable substrate modulus over the range of 10 – 900 MPa, which spans the complete range of substrate moduli for trabecular bone (93 – 365 MPa[3]) and the lower end of the range for cortical bone (871 – 11,500 MPa[3]). Osteogenic differentiation and mineralization increased as the substrate modulus increased from 10 to 900 MPa, which has not been previously reported in 3D. Mineralization also increased as pore size decreased from 557 to 423 μm. While the t-FDM scaffolds described herein exhibited precisely controlled topological properties with ~100% interconnectivity, the patterned, rod-like pores of the t-FDM scaffolds differ from the irregular pores of trabecular bone. Future studies aim to design templated AM scaffolds with a mixture of rods and plates, which more accurately recapitulates the topological properties of trabecular bone.

4. Experimental section:

Fabrication and characterization of PUR scaffolds from PLA templates: PLA templates were designed using Autodesk and fabricated by FDM (MakerBot Replicator® 2 3D printer). Polyester triols (300 g/mol or 3000 g/mol) were synthesized from a glycerol starter and a backbone comprising ε-caprolactone, glycolide, and D,L-lactide.[31] PUR scaffolds were synthesized by reactive liquid molding of HDIt, the polyester triol, and FeAA catalyst (5% FeAA in dipropylene glycol), which were poured into the PLA templates (14 mm diameter) after mixing and cured at 60°C overnight. PLA templates were then removed by extraction with dichloromethane overnight.

Pore size was controlled by adjusting the diameter of the PLA fibers, which was measured by SEM for 50 PLA fibers in each scaffold.

Cell culture: Primary rat bone marrow mesenchymal stem cells (BMSCs) were generated from pooled bone marrow from femurs of four Sprague-Dawley rats. BMSCs were maintained in DMEM with 10% FBS, 1% P/S, and 0.1% Amphotericin B (Sigma). Cells were detached at sub-confluency by trypsin EDTA (0.25%) and re-suspended at 10^6 cells/mL in complete medium and seeded on scaffolds (60 μl /scaffold) pre-soaked in fibronectin solution (4 μg/mL) at 37°C for 24 h. After seeding, scaffolds were incubated for 4h (5% CO_2 and 37°C) in 12-well plates before adding 2mL complete medium to facilitate cell attachment to the surface. A Live/Dead® Viability/Cytotoxicity Kit (Invitrogen) was used to measure cell viability 48h after seeding. Cell proliferation and metabolism were measured by total protein (BCA Protein Assay Reagent, Thermo) and MTS assay (CellTiter 96® Aqueous Non-Radioactive Cell Proliferation Assay, Promega) respectively.

Cell migration assay: BMSCs plated on 2D PUR films were cultured in a live cell chamber (LiveCell™) at 5% CO_2 and 37°C and monitored by light microscopy (Olympus CKX41). Photos of the same field were taken every 30 min and the photo series analyzed by Image J to track single cell movement. The 3D BMSC invasion assay was conducted using a cell transwell plate (Corning). Cells were cultured on 3D scaffolds (3 mm height × 6 mm diameter) as described above and placed in the transwell inserts. Cells were attracted to the bottom by serum gradient. Complete

medium was added to the outer well while reduced serum was used in the transwell to establish a serum gradient. After 72 h, the inserts were removed and the number of cells attached to the bottom plate counted by optical microscopy.

Osteogenesis assays: BMSCs were cultured in complete medium after seeding for 4 days and changed to osteoinductive medium for osteoblast differentiation (10 nM dexamethasone, 50 μM ascorbic acid and 0.1 mM β-glycerophosphate). Cells were detached by trypsin EDTA (0.25%) at D5, D10, and D15, and total RNA was isolated from the harvested cell pellets by RNeasy mini Kit (Qiagen). cDNA synthesis was carried out from purified total RNA using iScript™ Reverse Transcription Supermix (Biorad). Quantitative real-time PCR (qPCR) for osteogenic genes was performed to assess osteoblast differentiation. The following primers were used: *Runx2*: TCCAGACCAGCAGCACTCC (forward 5' to 3'), GTTATGAAAAACCAAGTAGCCAGGT (reverse 5' to 3'); *Col-1*: TGCTGATGGACAACCTGG (forward 5' to 3'), ACTGTTGCCTTTGGGACC (reverse 5' to 3'); *OPN*: AGTGGTTTGCCTTTGCCTGTT (forward 5' to 3'), TCAGCCAAGTGGCTACAGCAT (reverse 5' to 3'); *FN*: GCACAGGGGAAGAAAAGGAG (reverse 5' to 3'), TTGAGTGGATGGGAGGAGAG (reverse 5' to 3').

Mineralization: Scaffolds were maintained in osteogenic media for up to 21 days, washed with DPBS (Gibco), and fixed in formalin (10%). Alizarin Red S staining was applied after fixation. In one cohort, dyes were dissolved in 5% SDS immediately following staining, and the absorbances

of the resulting solutions were read on a plate reader (OD=550nm). In another cohort, scaffolds were fixed in 10% formalin for 15 minutes, washed in PBS, and dehydrated through increasing alcohol concentrations (50-100%) Fixed scaffolds were embedded in poly(methyl methacrylate) (PMMA), cut into 5 μm sections, and stained with Alizarin Red S for histological evaluation of mineralization. In a third cohort, scaffolds were cut to expose the center surfaces, fixed as described above, air-dried, and mounted to a specimen stub using carbon tape. Samples were sputter-coated with gold (108 Auto Sputter Coater; TedPella, Redding CA) and viewed via scanning electron microscopy (Hitachi, Finchampstead, UK).

Statistical Analysis: The statistical significance between experimental groups was determined by Student's *t test* or by a two-factor ANOVA. Graphs show mean and S.D., and $p < 0.05$ is considered statistically significant.

Acknowledgments

Research reported in this publication was supported by the National Institute of Arthritis and Musculoskeletal and Skin Diseases (part of the National Institutes of Health, under Award Number 5R01AR056138-02), the National Science Foundation under Award Number DMR-0847711, and the Department of Veterans Affairs under Award Number 1I01BX001957. The content is solely the responsibility of the authors and does not necessarily represent the official views of the National Institutes of Health, the National Science Foundation, or the Department of Veterans Affairs.

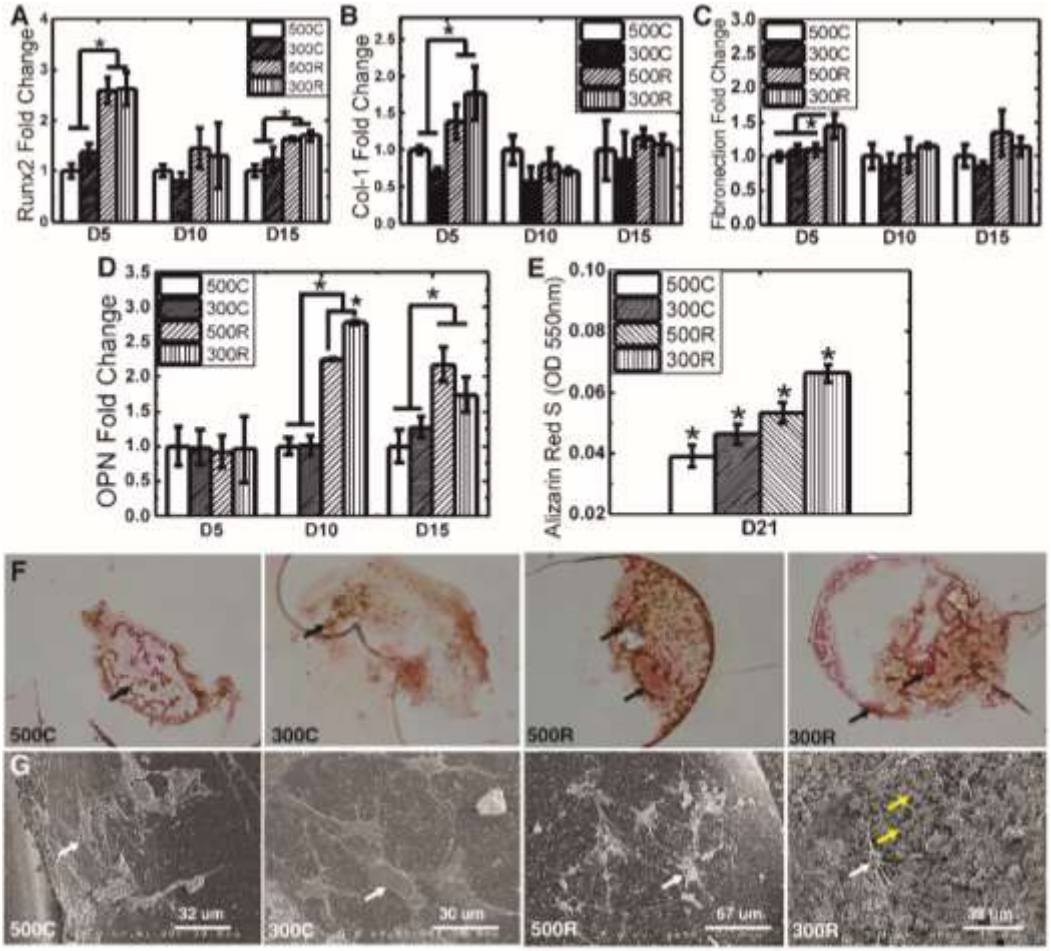

Figure 0.3 Osteogenic differentiation and mineralization increase with increasing substrate modulus and decreasing pore size of t-FDM scaffolds.

(A-D) Gene expression measured by qPCR. (A) *Runx2* (osteogenic transcription factor) expression is highest on 500R and 300R scaffolds on D5 and D15. (B) *Col-1* expression is significantly higher on rigid scaffolds on D5. (C) *Fn* expression is highest on 300R scaffolds on D5. (D) *OPN* (late marker of osteogenic differentiation) expression is highest on rigid scaffolds on D10 and D15, and highest on 300R scaffolds on D10. (E) Alizarin Red S absorbance measured at 550 nm increases significantly with increasing substrate modulus and decreasing pore size. (F) High-magnification (40X) images of histological sections stained with Alizarin Red S show more extensive mineralized nodules (black arrows) on rigid versus compliant scaffolds. (G) SEM images show larger and more extensive mineralized nodules on 300R scaffolds (yellow arrow), as well as cells embedded in extracellular matrix (white arrows). * $p < 0.05$.

Reference

[1] T. K. Schuessler, X. Y. Chan, H. J. Chen, K. Ji, K. M. Park, A. Roshan-Ghias, P. Sethi, A. Thakur, X. Tian, A. Villasante, I. K. Zervantonakis, N. M. Moore, L. A. Nagahara, N. Z. Kuhn, Cancer Res 2014, 74, 5359.

[2] A. A. Zadpoor, Biomaterials Science 2015, 3, 231.

[3] K. E. Smith, S. L. Hyzy, M. Sunwoo, K. A. Gall, Z. Schwartz, B. D. Boyan, Biomaterials 2010, 31, 6131.

[4] A. Parekh, N. S. Ruppender, K. M. Branch, M. K. Sewell-Loftin, J. Lin, P. D. Boyer, J. E. Candiello, W. D. Merryman, S. A. Guelcher, A. M. Weaver, Biophys J 2011, 100, 573.

[5] F. Rossi, M. Santoro, G. Perale, J Tissue Eng Regen Med 2013, DOI: 10.1002/term.1827; L. A. Cyster, D. M. Grant, S. M. Howdle, F. R. Rose, D. J. Irvine, D. Freeman, C. A. Scotchford, K. M. Shakesheff, Biomaterials 2005, 26, 697; A. Penk, Y. Forster, H. A. Scheidt, A. Nimptsch, M. C. Hacker, M. Schulz-Siegmund, P. Ahnert, J. Schiller, S. Rammelt, D. Huster, Magnetic resonance in medicine : official journal of the Society of Magnetic Resonance in Medicine / Society of Magnetic Resonance in Medicine 2013, 70, 925.

[6] V. Karageorgiou, D. Kaplan, Biomaterials 2005, 26, 5474.

[7] A. J. Engler, S. Sen, H. L. Sweeney, D. E. Discher, Cell 2006, 126, 677; M. Guvendiren, J. A. Burdick, Nature communications 2012, 3, 792; A. S. Rowlands, P. A. George, J. J. Cooper-White, Am J Physiol Cell Physiol 2008, 295, C1037.

[8] D. E. Discher, P. Janmey, Y. L. Wang, Science 2005, 310, 1139.

[9] S. W. Moore, P. Roca-Cusachs, M. P. Sheetz, Dev Cell 2010, 19, 194.

[10] C. B. Khatiwala, P. D. Kim, S. R. Peyton, A. J. Putnam, J Bone Miner Res 2009, 24, 886; C. B. Khatiwala, S. R. Peyton, M. Metzke, A. J. Putnam, J Cellular Physiology 2007, 211, 661.

[11] C. M. Bidan, K. P. Kommareddy, M. Rumpler, P. Kollmannsberger, P. Fratzl, J. W. Dunlop, Advanced healthcare materials 2013, 2, 186.

[12] M. Rumpler, A. Woesz, J. W. Dunlop, J. T. van Dongen, P. Fratzl, J R Soc Interface 2008, 5, 1173.

[13] J. A. Sanz-Herrera, P. Moreo, J. M. Garcia-Aznar, M. Doblare, Biomaterials 2009, 30, 6674.

[14] W. C. Oliver, G. M. Pharr, Journal of Materials Research 1992, 7, 1564.

[15] J. E. Dumas, K. Zienkiewicz, S. A. Tanner, E. M. Prieto, S. Bhattacharyya, S. Guelcher, Tissue Eng Part A 2010, 16, 2505.

[16] L. J. Gibson, M. F. Ashby, *Cellular solids: Structure and properties*, Cambridge University Press, 1997.

[17] E. Meijering, O. Dzyubachyk, I. Smal, Methods Enzymol 2012, 504, 183.

[18] L. Soroceanu, T. J. Manning, Jr., H. Sontheimer, The Journal of neuroscience : the official journal of the Society for Neuroscience 1999, 19, 5942.

[19] C. Gersbach, J. Le Doux, R. Guldberg, A. Garc á, Gene Ther 2006, 13, 873; M. Bruderer, R. G. Richards, M. Alini, M. J. Stoddart, Eur Cell Mater 2014, 28, 269; J. S. Lee, J. M. Lee, G. I. Im, Biomaterials 2011, 32, 760.

[20] X. Wang, H. Schr öder, V. Grebenjuk, B. Diehl-Seifert, V. Mail änder, R. Steffen, U.

Schloßmacher, W. Müller, Mar Drugs 2014, 12, 1131; Z. Hamidouche, O. Fromigué, J. Ringe, T. Häupl, P. Vaudin, J. Pagès, S. Srouji, E. Livne, P. Marie, Proc Natl Acad Sci U S A. 2009, 106, 18587.
[21] J. S. Park, J. S. Chu, A. D. Tsou, R. Diop, Z. Tang, A. Wang, S. Li, Biomaterials 2011, 32, 3921; D. Karamichos, J. Skinner, R. Brown, V. Mudera, J Tissue Eng Regen Med 2008, 2, 97.
[22] Q. Chen, P. Shou, L. Zhang, C. Xu, C. Zheng, Y. Han, W. Li, Y. Huang, X. Zhang, C. Shao, A. I. Roberts, A. B. Rabson, G. Ren, Y. Zhang, Y. Wang, D. T. Denhardt, Y. Shi, Stem Cells 2014, 32, 327; J. Lee, A. A. Abdeen, K. A. Kilian, Sci Rep 2014, 4, 5188; J. Sodek, B. Ganss, M. D. McKee, Osteopontin 2000, 11, 279.
[23] Y. Talukdar, J. Rashkow, G. Lalwani, S. Kanakia, B. Sitharaman, Biomaterials 2014, 35, 4863.
[24] A. Alford, S. Terkhorn, A. Reddy, K. Hankenson, Bone 2010, 46, 464; N. Su, Q. Sun, C. Li, X. Lu, H. Qi, S. Chen, J. Yang, X. Du, L. Zhao, Q. He, M. Jin, Y. Shen, D. Chen, L. Chen, Human molecular genetics 2010, 19, 1199.
[25] A. J. Galliher, W. P. Schiemann, Breast Cancer Res 2006, 8, R42.
[26] S. Van Bael, Y. C. Chai, S. Truscello, M. Moesen, G. Kerckhofs, H. Van Oosterwyck, J. P. Kruth, J. Schrooten, Acta Biomater 2012, 8, 2824.
[27] Q. M. Jin, H. Takita, T. Kohgo, K. Atsumi, H. Itoh, Y. Kuboki, J. Biomed. Mater. Res. 2000, 52, 841.
[28] Y. Takahashi, Y. Tabata, J Biomater Sci Polym Ed 2004, 15, 41.
[29] Y. Kuboki, Q. Jin, H. Takita, J Bone Joint Surg Am 2001, 83-A Suppl 1, S105.
[30] T. Hildebrand, P. Ruegsegger, Computer methods in biomechanics and biomedical engineering 1997, 1, 15.
[31] S. A. Guelcher, V. Patel, K. M. Gallagher, S. Connolly, J. E. Didier, J. S. Doctor, J. O. Hollinger, Tissue Engineering 2006, 12, 1247.

CHAPTER 5

SCAFFOLD RIGIDITY REGULATES THE REGENERATIVE RESPONSE IN EXCISIONAL WOUNDS THROUGH THE MACROPHAGE PHENOTYPE AND WNT SIGNALING

1. Introduction

The growing need for the treatment of large cutaneous defects has led to considerable interest in the design of improved scaffolds for stimulate wound healing. While many studies have focused on the acceleration of wound closure, a growing number of studies have aimed to restore the function of impaired tissue through a more regenerative wound approach [1]. Local delivery of growth factors, such as platelet-derived growth factor (PDGF), transforming growth factor-β (TGF-β), and vascular endothelial growth factor (VEGF), from scaffolds has improved wound repair and restoration [2-4]. However, growth factor delivery requires optimized release kinetics to enhance tissue healing and minimize adverse events [5], and translation of local drug delivery technologies requires a more complex regulatory pathway.

An increasing body of evidence highlights the relative contribution of the mechanical properties of implanted scaffolds on the process of wound healing healing [6, 7]. Orientation of both fibroblasts infiltrating the wound bed as well as the extracellular matrix they deposit has been identified as a key parameter for evaluating scar formation and is affected by the elastic modulus of the implanted scaffold [8, 9]. The mechano-responsive properties of fibroblasts, which comprise a significant component of the granulation tissue, has been investigated to understand the mechanisms by which scaffold modulus regulates wound healing. The activity of dermal

fibroblasts that determine wound phenotype is regulated by β-catenin, which is a crucial component of the canonical Wnt signaling pathway [10, 11]. Genetically stabilized β-catenin has been considered to lead to hyperplastic scars [12-14], and thus down-regulation of the elevated β-catenin protein level of wound fibroblasts [14] is required to improve cutaneous wound repair.

In addition to Wnt signaling, macrophage polarization has also been implicated as a factor regulating the regenerative versus fibrotic (i.e., scarring) phenotype. Recent studies have reported that while both macrophage phenotypes are present throughout the wound healing process, the relative ratio of regenerative to inflammatory macrophages contributes to wound healing outcomes [15, 16]. Markers for M1 (inflammatory) and M2 (regenerative) macrophages have been evaluated from cells harvested from the wound bed without specific cell type separation to detect their effects on wound healing [17, 18]. Macrophage polarization is regulated by the fiber and pore sizes of electrospun scaffolds [19], and mechanical forces to scaffolds stimulate inflammation [13, 20]. However, the effects of scaffold modulus on macrophage polarization have not been extensively investigated.

In the present study, we designed poly(ester urethane) (PUR) scaffolds using a templated-Fused Deposition Modeling (t-FDM) process to investigate the effects of the elastic modulus of the PUR (the substrate modulus, E_s) on wound healing in a rat subcutaneous model. Considering previous studies reporting that scaffold degradation rate [1] and initial bulk modulus (E_B) [21] regulate regeneration versus scarring, t-FDM scaffolds were designed with slow degradation rates and initial bulk moduli exceeding that of host dermal tissue to isolate the effects of the substrate modulus. Thus, the effects of substrate modulus on collagen deposition and alignment,

angiogenesis, Wnt signaling, and macrophage polarization were investigated by controlling the crosslink density of the PUR.

2. Materials and Methods

2.1 Materials

DMEM (1.0 g/L glucose = 1.0 g/L) and fetal bovine serum (FBS) were purchased from Thermo Scientific. Penicillin/streptomycin (P/S), trypsin EDTA, and Amphotericin B were obtained from Corning Cellgro. Glycolide and D,L-lactide were purchased from Polysciences (Warrington, PA). Hexamethylene diisocyanate trimer (HDIt) was supplied by Bayer Material Science (Pittsburgh, PA). Iron acetylacetonate (FeAA) catalyst was supplied by Sigma-Aldrich. ε-caprolactone (Sigma-Aldrich) was dried over anhydrous $MgSO_4$, and all other materials were used as received.

2.2 Fabrication of PUR scaffolds from 3D printed PLA templates

Polylactic acid (PLA) templates were designed by Solidworks (Waltham, MA) with desired fiber diameter and dimensions and then fabricated by Fused Deposition Modeling (FDM) with a MakerBot® Replicator® 2 3D printer. Polyester triols (300 g/mol, 720 g/mol or 3000 g/mol) were synthesized from a glycerol starter and a backbone comprising ε-caprolactone, glycolide, and D,L-lactide as described previously [22]. Polyurethane (PUR) scaffolds were synthesized by reactive liquid molding of HDIt with a hardener component comprising the polyester triol and iron catalyst (5% iron acetylacetonate (FeAA) in dipropylene glycol). The reactants were poured into the PLA

templates (for 3D scaffolds) or tissue culture plates (for 2D films) after mixing and cured at 60^{o}C overnight. After cure, the PLA template was leached from the scaffold by immersion in dichloromethane overnight.

2.3 Scaffold characterization

Scaffold porosity was calculated from mass and volume measurements of cylindrically punched 3D PUR scaffolds (n=4) as previously described [22]. Pore size and morphology of the scaffolds were measured by scanning electron microscopy (Hitachi S-4200 SEM, Finchampstead, UK) after gold sputter coating with a Cressington Sputter Coater. The bulk moduli of both the 2D films (K) and 3D scaffolds (K^{*}) were measured under compression by MTS after pre-soaking in PBS overnight at 37^{o}C.

2.4 In vivo cutaneous repair in rats

All surgical and care procedures were carried out under aseptic conditions per an approved Institutional Animal Care and Use Committee (IACUC) protocol. The study design is listed in Table 5.1. Scaffolds (n=4) of each rigidity were punched into 6-mm cylinders, sliced to form 2-mm discs, and implanted in rat subcutaneous wounds in adult male Sprague-Dawley rats. All scaffolds were sterlized in 70% ethanol overnight and washed with PBS prior to implantation. Rats were euthanized 7d, 14d, and 21d after surgery and the wounds harvested for histology and quantitative real-time PCR (q-PCR). For histological staining, harvested wounds were fixed in neutral buffered formalin overnight at 4, transferred into 70% ethanol for 48 h, embedded in

paraffin, and sectioned at 5 μm. Cellular infiltration was quantified by Hematoxylin & eosin (H&E) performed on the tissue sections. Histological images were taken by Olympus white light microscope and image quantification were performed with Image J. Collagen fiber orientation was measured from tissue sections stained with Masson's trichrome green, and color images were taken under the same settings. The fiber alignment evaluation was carried out using a previously published ImageJ plug-in "OrientationJ" [23, 24]. Collagen fiber directional variance of infiltrated tissues was calculated from the local angle distribution by analyzing the low magnification images (2x) at each pixel using coherency weighted alignment. To compare the local fiber alignment, directional variance was computed and normalized to the total pixels of the selected ROI.

Table 0.1 Animal study design.

Treatment group	Polyester triol M_n (g/mol)	7 days	14 days	21 days
S300	300	4	4	4
S720	720	4	4	4
S3000	3000	4	4	4

2.5 Isolation and culture of fibroblasts

Primary rat fibroblast cells from the wound bed were generated from pooled implanted PUR scaffolds for n=4 rats and were maintained in DMEM supplemented with 10% FBS, 1% P/S, and 0.1% Amphotericin B (Sigma). Primary rat dermal fibroblast cells were isolated as previously described. Briefly, rat foreskins were harvested and maintained in trypsin EDTA (0.25%) overnight

at 4^{o}C, and the dermis was detached and plated in a tissue culture plate with complete cell culture medium. Cells were detached at sub-confluency by trypsin EDTA (0.25%), re-suspended at 10^5 cells/mL in complete medium, and cultured on either 2D films or directly in a 12-well tissue culture plate (1 mL/well). To facilitate cell attachment, all PUR films were pre-treated with a fibronectin solution (4 μg/mL in PBS) in cell culture incubator for 24 h. Fibroblast cells were cultured in complete medium for up to 7 days and then detached by trypsin EDTA (0.25%) and spun down to harvest cell pellets for further analysis. Conditioned media (CM) were daily transferred from wells with cells cultured on 2D films to cells in blank wells, and CM-treated cells were collected after 7 days for analysis.

2.6 Western Blotting

PUR films of different rigidities were synthesized in 6-well tissue culture plates as described above and incubated in complete cell culture medium overnight to facilitate cell attachment. Either dermal fibroblasts or fibroblasts from the wound bed were plated in PUR-coated tissue culture plates and cultured for up to 7 days. Cells were detached by trypsin EDTA (0.25%) and total protein extracted from cell pellets by RIPA buffer (Thermo scientific) containing protease inhibitors and phosphatase inhibitors (Thermo scientific) on ice for 15 min. Protein concentration was measured by Pierce BCA Protein Assay Kit. Cell lysates were then centrifuged at full speed for 15 min to remove cellular debris at 4^{o}C. Equal amounts of total protein were loaded onto SDS-PAGE gels, separated by Bio-rad 2-D Electrophoresis units, and transferred to PVDF membranes. The membrane was blocked in LI-COR preformed blocking buffer for 1h at room temperature and then

incubated with β-catenin antibody (8480S, Cell Signaling) in blocking buffer at 4ºC with gentle shaking overnight. HRP-conjugated goat anti-rabbit secondary antibody was then applied to the membranes after washing, and signals were detected by Western Lightning Chemiluminescent (PerkinElmer).

Table 0.2 Primers used for qPCR analysis.

Marker	Forward 5' to 3'	Reverse 5' to 3'
PDGF	CCCACACGTCAAACTACAGCTCCAA	GCCCAGTTCGTTTCAGTGCCACAT
Collagen-1	TGCTGATGGACAACCTGG	ACTGTTGCCTTTGGGACC
Collagen-3	CTGGATCTCCTGGTGCTAAG	CAGCGTGTCCTTGTGGTC
CD31	GGAGGTGACAGAAGGTGGGATTG	GCTTGGCAGCGAAACACTAACAGG
VEGF	GCCAGCACATAGGAGAGATGAG	ACCGCCTTGGCTTGTCAC
TGF-β	AAGTGGATCCACGAGCCCAA	GCTGCACTTGCAGGAGCGCA
TNF-α	GGCCACCACGCTCTTTCTGTCA	TGGGCTACGGGCTTGTCACTC
iNOS	CCTGGTGCAAGGGATCTTGG	GAGGGCTTGCCTGAGTGAGC
CD206	GGTTCCGGTTTGTGGAGCAG	TCCGTTTGCATTGCCCAGTA
GAPDH	GACTTCAACAGCAACTCC	GCCATATTCATTGTCATACCA
Axin2	GGACAGTAGCGTAGATGGAG	CGGAAAATGAGGTAGAGACA
CyclinD1	CTGGTGTTTGGAAGTAGGAA	GTTTAAAAGCCTCCTGTGTG
sFRP2	ATGGAAACCCTTTGTAAAAATGACT	TCTTGCTCTTTGTCTCCAGGATGAT

2.7 Gene Expression by RT-PCR

Harvested tissue samples were maintained in RNALater buffer until ready for RNA extraction. Total RNA was isolated from the harvested scaffolds or cell pellets by RNeasy mini Kit (Qiagen). cDNA synthesis was carried out from purified total RNA using iScript™ Reverse Transcription Supermix (Bio-rad). q-PCR amplified for growth factor, macrophage, and Wnt/β-catenin signaling pathway-related genes were measured to compare the effects of scaffold rigidity on wound healing. The primers used for q-PCR amplification are listed in Table 5.2. qPCR was performed with the IQ Real Time SybrGreen PCR Supermix (Biorad). All reactions were run in triplicate and the RT-PCR results of all genes were normalized to GAPDH.

2.8 Immunohisochemistry staining

Formalin-fixed paraffin-embedded tissues were sectioned at 5 μm, placed on slides, and warmed overnight at 60°C. Slides were deparaffinized and rehydrated with graded alcohols ending in Tris buffered saline (TBS-T Wash Buffer, LabVision, Freemont, CA). Heat-mediated target retrieval was performed in 1X Target Retrieval Buffer (Citrate, pH 6.0, DAKO, Carpenteria, CA). Endogenous peroxidases and non-specific background were blocked by subsequent incubations in 3% H_2O_2 (Fisher, Suwanee, GA) in TBS-T and protein block (DAKO). Primary antibody to rat CD68 was used at 1:800 for 1 h followed by secondary incubation in biotinylated rabbit anti-mouse IgG (1:200; Vector, Burlingame, CA) and tertiary incubation in SA-HRP (RTU, BD Pharmingen, San Jose, CA). Slides were rinsed with TBS-T between each reagent treatment and all steps were carried out at room temperature. Visualization was achieved with DAB+ chromogen (DAKO).

Slides were counterstained with Mayer's hematoxylin, dehydrated through a series of alcohols and xylenes, and then coverslipped with Acrytol Mounting Media (Surgipath, Richmond, IL). Immunohistochemical staining was performed using commercial antibody specifically directed against rat CD68 (Bio-Rad, Hercules, CA).

2.9 Statistical analysis

The statistical significance between experimental groups was determined by one-way ANOVA with Bonferroni correction. Graphs show mean ± SEM, and $p < 0.05$ is considered as statistically significant.

3. Results

3.1 Fabrication of templated 3D scaffolds

In this study, we investigated the effects of scaffold rigidity on rat subcutaneous wound healing. HDIt was selected as the isocyanate component due to its relatively slow hydrolytic degradation rate compared to the time scale of wound healing [25] in order to ensure that the mechanical properties of the scaffold did not change over the time course of the experiment. Considering the limited number of materials available for FDM, we printed PLA templates with a MakerBot® Replicator® 2 3D printer (Figure 5.1A). To control the rigidities of the PUR networks cast in the PLA templates, we used polyester triols with varying molecular weight (300, 720, or 3000 g mol^{-1}) to tune the bulk modulus of the PUR scaffolds from 2 to 200 MPa (Figure 5.1B). For *in vitro* 2D cell culture, the PUR reactants were directly cured in tissue culture plates to form

films that provided the same physical properties. Leaching of the PLA template in dichloromethane yielded scaffolds with 100% interconnected pores (Fig. 1C). The inner pore size was determined by the fiber diameter of PLA templates and thus was created uniformly to be 300 μm.

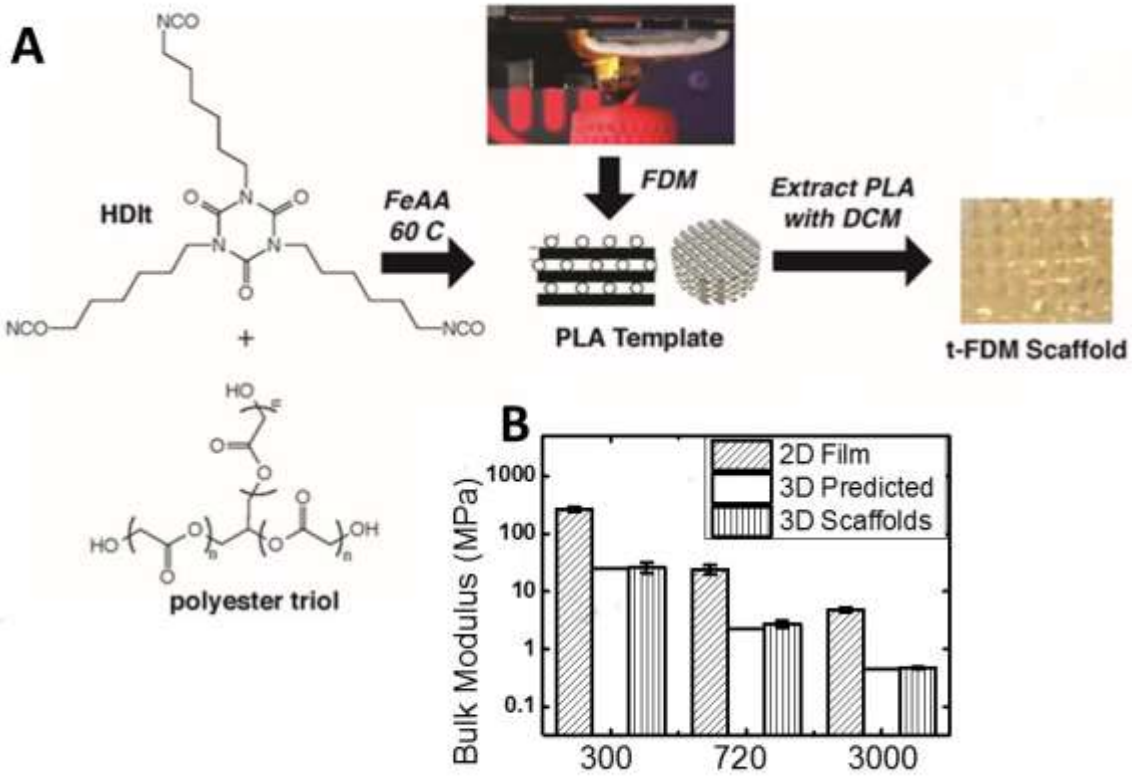

Figure 0.1 Fabrication and characterization of 3D PUR scaffolds.
(A) Process for fabrication of templated 3D PUR scaffolds. (B) Bulk modulus measured for 2D PUR films and 3D PUR scaffolds. Measured scaffold modulus is compared to the predicted value from Eq (1).

3.2 *Effects of scaffold modulus on cellular infiltration in a rat subcutaneous wound model*

In order to investigate the effects of scaffold rigidity on wound healing, scaffolds with varying

bulk moduli (3 groups, 3D-R, M, C) were implanted in subcutaneous wounds in adult male Sprague-Dawley rats. Scaffolds were explanted for histological analysis at D7, 14, and 21, and H&E staining was conducted to compare cellular infiltration between different groups. Infiltrating cells comprised both inflammatory cells (monocytes and neutrophils) and fibroblasts (Figure 5.2A), and the area % infiltrating cells was measured by histomorphometry (Figure 5.2B). Cellular infiltration was greatest in 3D-M scaffolds. Cell proliferation within the wound bed was analyzed by Ki67 immunohistological staining and quantified by the area % of Ki67+ cells. Similar to the trend observed for cellular infiltration, the population of Ki67+ cells remained significantly higher in the 3D-M scaffolds compared to the other two groups for up to 14 days (Figure 5.2C). After 14 days, Ki67+ cells decreased in all three groups and no significant difference was observed. These observations suggest that the 3D-M scaffolds stimulated cell proliferation and infiltration during the early stages of wound healing.

3.3 *Effects of scaffold modulus on matrix deposition and alignment in a rat subcutaneous wound model*

Collagen deposition in the wound bed was analyzed by trichrome green staining. High-magnification images of histological sections showed increased collagen deposition (stained green) in the 3D-M scaffolds on D7 (Figure 5.3A). In addition, expression of both type I and III collagen (*Col 1* and *Col 3*, respectively) measured by qPCR showed a consistent trend with the histology images, in which both *Col 1* and *Col 3* expression was greatest on 3D-M scaffolds (Fig. 3B-C). To compare differences in scarring between groups, the alignment of fibroblasts and deposited

collagen fibers was evaluated as previously described [26]. Figure 5.3D-E shows both quantitative (Figure 5.3D) and qualitative (Figure 5.3E) data illustrating alignment of the cells and extracellular matrix for each of the treatment groups.

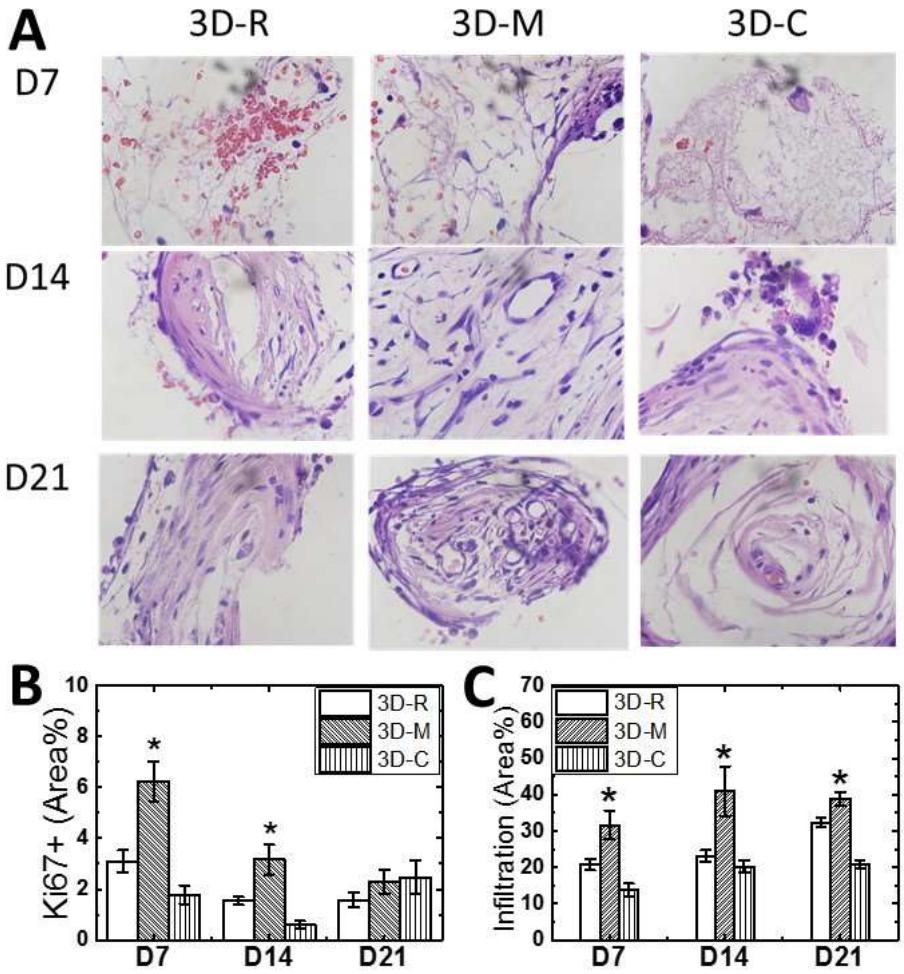

Figure 0.2 Effects of bulk modulus on cellular infiltration in rat subcutaneous wounds.
(A) High-magnification images of 3D scaffolds explanted on D7, D14, and D21 (100x). (B) Infiltration of cells into 3D scaffolds measured by histomorphometry. (C) Population of Ki67+ cells measured by immunohistochemical staining.

At each time point, directional variance values were significantly more disordered for the 3D-M scaffolds compared to the 3D-C and 3D-R scaffolds (Figure 5.3D). Figure 5.3E shows the

collagen angular distribution. Both 3D-C and 3D-R scaffolds showed a lower degree of random orientation (lack of variance as evidenced by a linear alignment of cells and collagen fibers) than 3D-M scaffolds, which displayed a higher degree of random orientation. Thus, directional variance of collagen fibers was the largest on 3D-M scaffolds, indicating promoted remodeling of collagens rather than scarring.

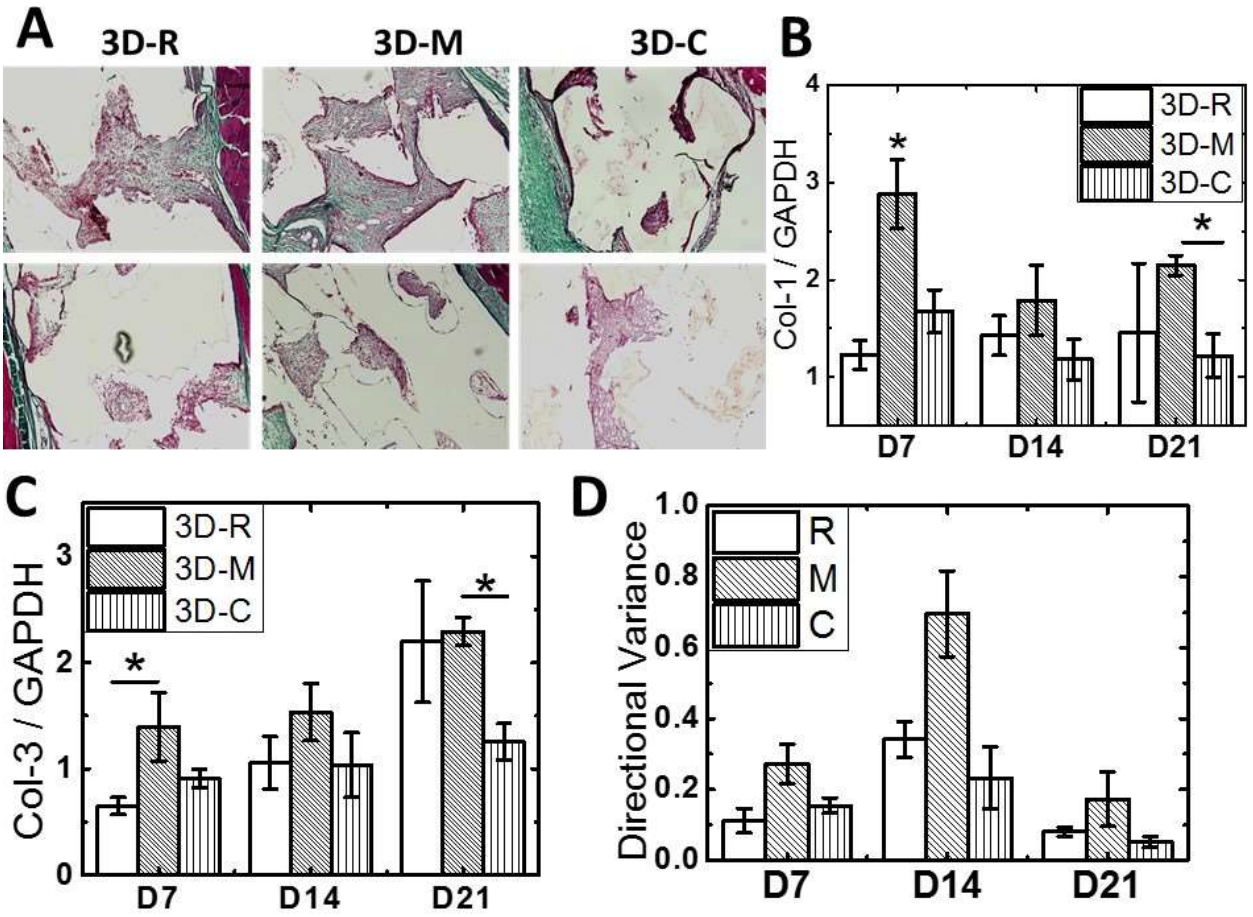

Figure 0.3 Effects of bulk modulus on collagen deposition in rat subcutaneous wounds.
(A) High-magnification images of histological sections of wounds on D7 stained with trichrome show increased collagen (green, C) deposition on 3D-M scaffolds (20x). (B-C) Expression of *Col-1* (B) and *Col-3* (C) measured by qPCR is highest on 3D-M scaffolds. (D) Directional variance of allignment of deposited collagen/fibroblast from low-maginification images (2x) of histological sections.

3.4 Effects of scaffold modulus on expression of growth factors associated with vascularization and wound healing

To understand the molecular mechanism of how scaffold modulus regulates wound healing, we measured expression of growth factors, including PDGF, TGF-β1, and VEGF, that are closely related to cutaneous wound repair *in vivo*. Considering previous studies highlighting the importance of PDGF in wound healing and that expression of PDGF was observed in an impaired animal model [27], we first evaluated the expression level of *PDGF* among all the scaffold groups. As shown in Figure 5.4A, *PDGF* gene expression in the granulation tissue was significantly higher on 3D-M scaffolds compared to the other groups for up to 21 days. Expression of *TGF-β1*, which is another key growth factor dominant wound healing and up-regulated during healing process, was also significantly higher on 3D-M scaffolds on D21 (Figure 5.4B), but was comparable to the other groups at earlier time points. In contrast, expression of *VEGF*, which is highly involved in vascularization during wound healing, showed an inverse trend characterized by minimal expression in the 3D-M scaffolds (Figure 5.4C).

The effects of bulk modulus on angiogenesis were also compared in this study. As a highly specific marker for vascular and endothelial cells [28], gene expression of *CD3*1 was evaluated as a marker of neovessel formation, which was greatest on 3D-M scaffolds on D14 and D21 (Figure 5.4D). Immunohistological staining for Collagen IV was also performed to confirm the CD31 gene expression findings, since CD31 staining was difficult to image in rat tissues. Collagen IV is a major basement membrane component that has been implicated in the regulation of angiogenesis

[29]. As shown in Figure 5.4E, by D21 angiogenesis in the wound bed was significantly higher in 3D-M scaffolds, which is consistent with *CD31* gene expression.

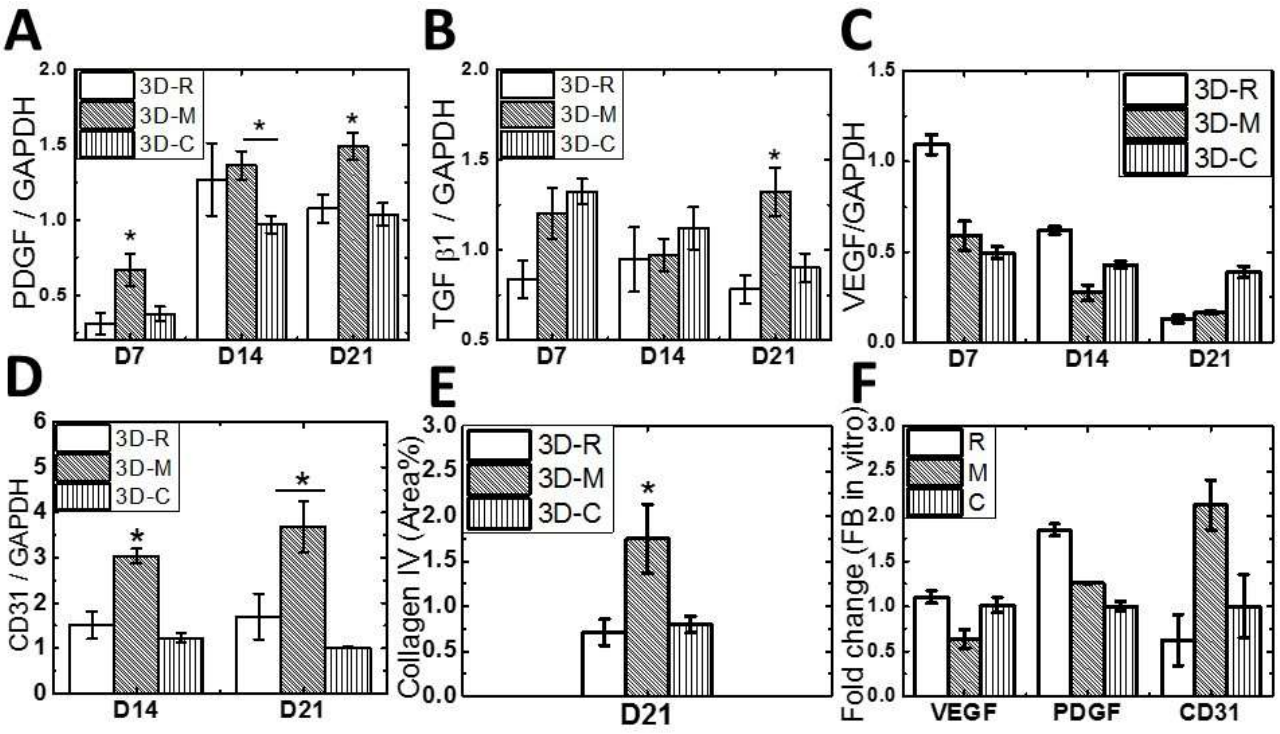

Figure 0.4 Effects of bulk modulus on wound vascularization and expression of growth factors associated with wound healing.

(A) Expression of *PDGF* (measured by qPCR) is greatest on 3D-M scaffolds at all time points. (B) Expression of *TGF-β1* is highest on 3D-M scaffolds on D21. (C) Expression of *VEGF* is minimal on 3D-M scaffolds at all time points. (D-E) Wound vascularization, as assessed by *CD31* gene expression (D) and Collagen IV immunohistochemical staining (E), is highest in 3D-M scaffolds. (F) Fibroblast gene expression cultured on 2D PUR films of the same rigidities.

3.5 Effects of scaffold modulus on expression of Wnt-related genes by fibroblasts infiltrating the wound bed

Differences in cellular infiltration, matrix deposition, and gene expression as a function of

scaffold bulk modulus point to a mechanotransduction mechanism regulating wound healing. Since fibroblasts have been reported to be highly mechano-sensitive [30] and infiltrate the scaffold during cutaneous wound repair, the effects of bulk modulus on fibroblasts isolated from the wound bed were investestigated. Wnt signaling has been recognized as a key mechanotransduction pathway in fibroblasts that regulates wound healing; therefore, the expression level of Wnt-related genes by fibroblasts in response to substrate rigidity was evaluated. Fibroblasts harvested from the implanted scaffolds at D7 were plated on 2D-C, 2D-M, and 2D-R films. Since these 2D films were synthesized from the same polyester triols as the 3D scaffolds, the bulk modulus of the PUR network in the 2D films and 3D scaffolds was comparable (Figure 5.1B). Expression of Wnt-related target genes *Cyclin D1* and *Axin 2* was minimized on 3D-M scaffolds, while expression of secreted Frizzled-Related Protein-2 (*sFRP2*, an inhibitor of Wnt signaling) was maximized on 3D-M scaffolds (Figure 5.5A). Secretion of β-catenin, an intracellular signal transducer in the Wnt signaling pathway, measured by Western blotting with total protein lysate was also minimized on 3D-M scaffolds (Figure 5.5B).

We performed conditioned medium experiments with rat dermal fibroblasts to test the hypothesis that changes in expressions of genes related to matrix deposition, angiogenesis, and Wnt signaling in response to the scaffold bulk modulus were due to paracrine signaling. Dermal fibroblasts were cultured on 2D-C, 2D-M, and 2D-R films for 48 h. Conditioned medium was recovered from the 2D films and used to treat dermal fibroblasts cultured in tissue culture well plates. Consistent with the results for fibroblasts harvested from the explanted scaffolds, expression of *Cyclin D1* was lowest and expression of *CD31* was highest for dermal fibroblasts

cultured in conditioned medium from 2D-M and 2D-R films (Figure 5.5C). Expression of *Col-1* and *Col-3* was highest for cells cultured in conditioned medium from 2D-M films (Figure 5.5C). Thus, the conditioned medium experiments are consistent with the notion that the observed effects of scaffold bulk modulus on fibroblast gene expression are mediated by paracrine signaling.

3.6 Effects of scaffold rigidity on macrophage polarization (M1/M2 ratio)

Considering that polarization of macrophages is critical for wound repair and regeneration [31], we investigated the effects of the scaffold bulk modulus on macrophage polarization. Expression of *iNOS* was selected as a marker for the M1 inflammatory phenotype, and *CD206* was selected as a marker for the M2 regenerative phenotype as previously reported [32]. Expression of *iNOS* was highest (Figure 5.6A) and expression of *CD206* lowest (Figure 5.6B) on 3D-R scaffolds. .Therefore, the ratio of macrophage polarization M1/M2, which determines the fibrotic versus regenerative potential during wound healing, was minimized in 3D-M scaffolds at D7 (Figure 5.6C). Similarly, expression of the inflammatory cytokine *TNF-α*, which is associated with the M1 phenotype, was down-regulated on 3D-C and 3D-M scaffolds (Figure 5.6D). Immunohistochemical staining was also performed for CD68, a pan-macrophage marker, to measure the total number macrophages between all groups (Figure 5.6E). Similar to the gene expression data, the total number of macrophages was lowest in 3D-M scaffolds. Thus, the macrophage polarization data suggest that the 3-M scaffolds polarize infiltrating macrophages toward the regenerative phenotype, which is consistent with the matrix deposition/alignment, angiogenesis, and Wnt signaling pathway data.

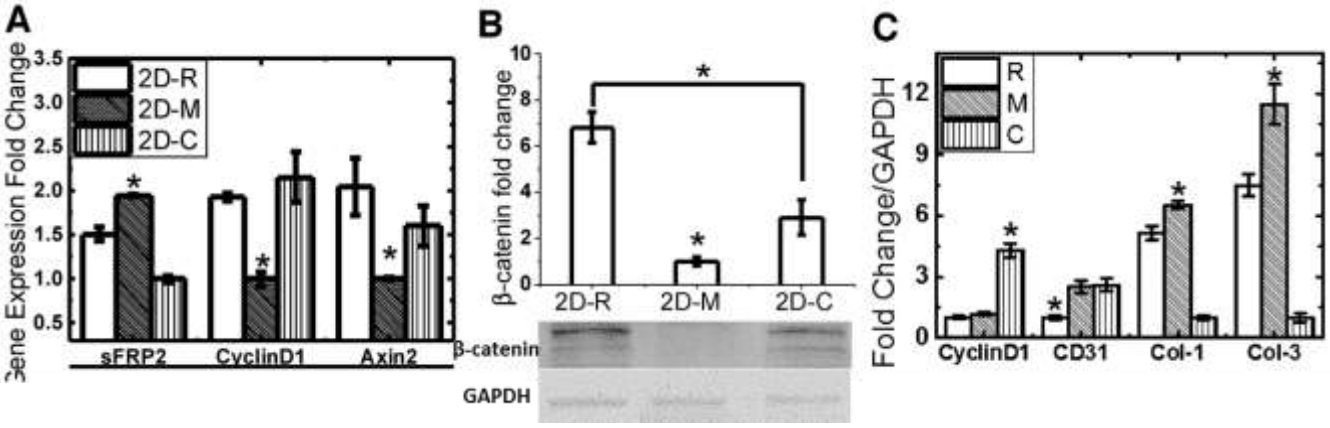

Figure 0.5 Effects of bulk modulus on Wnt signaling in fibroblasts.

(A) Expression of Wnt target genes *Cyclin D1* and *Axin 2* by harvested fibroblasts is down-regulated on 3D-M scaffolds, while expression of the Wnt regulator *sFRP-2* is up-regulated. (B) Translocation of β-catenin from the cytoplasm to the nucleus is down-regulated on 3D-M scaffolds in harvested fibroblasts. (C) Wound fibroblasts were cultured on 2D-R, 2D-M, and 2D-C substrates. Conditioned medium was harvested and used to treat wound fibroblasts cultured on tissue culture plastic. Fibroblasts cultured in conditioned medium from 2D-M and 2D-R expressed more Wnt inhibitors, resulting in reduced expression of the Wnt target gene Cyclin D1. Expression of CD31 was highest with 2D-M and 2D-C conditioned medium, and *Col 1* and *3* expression was highest with 2D-M conditioned medium.

4. Discussion:

Cutaneous tissue repair in adults is an imperfect compromise between regenerative repair and restoration of integrity [33]. Recent studies have highlighted the importance of pore size, morphology, and interconnectivity [34, 35] as well as the scaffold degradation rate [1, 36] toward preventing scar formation, but the effects of substrate modulus on matrix deposition and alignment, angiogenesis, and macrophage phenotype have not been extensively investigated. While

mechanical stress can have beneficial effects on epidermal regeneration via enhanced proliferation, angiogenesis and stem cell recruitment [37], it also increases infiltration of inflammatory cells and decreases apoptosis of local cells involved in wound remodification, and is therefore a major factor in tissue fibrosis and scarring [38]. These competing effects suggest that there is an optimizal substrate rigidity that promotes the regenerative versus the scarring phenotype. In order to isolate the effects of substrate modulus on wound healing, we applied the t-FDM technique to precisely control the properties of the scaffolds. High interconnectivity was achieved at 50% porosity, which enabled the fabrication of scaffolds with bulk moduli (E_B) exceeding that of dermal tissue, resulting in stenting of the wound and delayed contraction [21]. Furthermore, t-FDM scaffolds were prepared from polymers that persist throughout the remodeling phase [39], which has been reported to enhance regeneration versus scarring [1]. We designed scaffolds with substrate modulus ranging from 5 – 266 MPa to investigate the effects of substrate modulus on cutaneous wound healing. Scaffolds with an intermediate value of E_s = 24 MPa promoted increased deposition and random orientation of collagen, angiogenesis, and regenerative macrophage polarization compared to more compliant (E_s = 5 MPa) and rigid (E_s = 266 MPa) scaffolds. Furthermore, Wnt signaling was down-regulated on scaffolds with an intermediate substrate modulus. These observations point to substrate modulus as a key parameter regulating the regenerative versus the scarring phenotype.

Multiple growth factors, such as PDGF, TGF-β1, and VEGF, have been shown to be critical for cutaneous wound repair.(REF) Thus, to better understand the mechanism of how substrate modulus affects wound healing, we evaluated the expression level of these growth factors in the

total RNA extracted from infiltrated scaffolds at D7, 14, and 21. PDGF expression was up-regulated in the 3D-M scaffolds, which was consistent with the angiogenesis data. The addition of exogenous PDGF to wounds results in increased cell density of the loose subepithelial connective tissue layer but not the extracellular components or growth of the epithelial cell layer [40]. Thus, up-regulation of PDGF by infiltrating cells is essential for enhanced cutaneous wound healing (REF). In contrast, VEGF expression was minimal on 3D-M scaffolds and showed an inverse trend compared to vascularization (indicated by collagen IV IHC). Although VEGF is important for expedient closure in large excisional wounds [41], neutralization of VEGF throughout the healing process significantly reduced scar size and increased the quality of the collagen deposited in incisional wounds [37]. TGF-β1 is another important growth factor for wound regeneration, and has been reported to promote cellular infiltration and proliferation at wound sites [42]. However, activation of TGF-β1 signaling also elevates cell apoptosis, which is an important process initiating the wound remodeling phase to form scarless tissue [43]. In the present study, the expression level of TGF-β1 in 3D-M scaffolds was significantly up-regulated than the other two groups at D21, suggesting its lateral effects on wound remodification to promote skin tissue regeneration.

The consistency of these growth factor expression levels from total RNA directly harvested from wounds and wound bed-derived fibroblasts points to fibroblasts as a key cell population determining the effects of substrate rigidity on wound healing. Among the mechanotransduction pathways, the Wnt/β-catenin pathway has been reported to be crucial for cutaneous wound regeneration (REF) and was therefore evaluated for the fibroblast response to substrate rigidity.

An abnormally elevated β-catenin protein level of wound fibroblasts has been considered to contribute to excessive fibrosis and scar formation [44, 45]. In the present study, wound bed-derived fibroblasts showed down-regulated Wnt signaling on 2D-M films, as evidenced by decreased expression of the target genes *Cyclin D1* and *Axin 2* , decreased β-catenin protein production, and increased expression of the Wnt inhibitor *sFRP2*. Considering previous studies reporting that the behavior of wound fibroblasts may differ from dermal fibroblasts from non-wound sites [46], we harvested dermal fibroblasts from adult rat skin and verified β-catenin protein expression in response to substrate rigidities. Dermal fibroblasts exhibited the same minimization of Wnt/β-catenin signaling on 2D-M films as those harvested from the scaffolds (supplemental information). Wnt/β-catenin signaling has been reported to be abnormally up-regulated as a consequence of wounding in a cutaneous implant study and leadd to hyperplastic wounds [47]. Targeting the Wnt/β-catenin signaling pathway has been considered a potential strategy for the treatment of fibrosis [48], and previous studies have proved that a lower level of β-catenin resulted in smaller wound size [49]. Therefore, as an alternative to the delivery of inhibitor molecules of Wnt/β-catenin signaling, our observations highlight the possibility of modulating Wnt/β-catenin signaling in cutaneous wounds by tuning the substrate modulus.

Manipulating the inflammatory macrophage phenotype can also enhance regeneration, in part by altering the fibrotic response. Macrophage phenotype can be regulated by pharmacological treatment, macrophage-fibroblast interactions, and mechanical and topological properties of the scaffold (REF). Thus, we also investigated the effects of substrate modulus on macrophage polarization in the rat subcutaneous wound model. IHC staining of total macrophages (CD68)

showed fewer macrophages in the 3D-C and 3D-M scaffolds, which is consistent with expression of TNF-α, a pleiotropic molecule that plays a central role in inflammation and immune system development. A reduced inflammatory response is one of the factors required for scarless wound healing [50] and therefore the reduction in total macrophages in the 3D-M scaffolds potentially benefits the cutaneous wound healing in this study. Recent studies have pointed out that M1 (inflammatory) and M2 (regenerative) macrophage phenotypes and their relative ratio determines the stage of wound healing [16]. For cutaneous wound healing, M1 and M2 markers have been examined from the whole harvest cell population without specific cell type separation to detect their effects on wound healing [17, 18], and a similar evaluation was conducted in the present study. Expression of iNOS, an M1 marker, was lowest on 3D-M scaffolds (Figure 5.6A), while expression of CD206, an M2 marker, was highest on 3D-M scaffolds (Figure 5.6B). Consequently, the M1/M2 ratio was minimized for the 3D-M scaffolds, suggesting that these scaffolds drive the would healing response toward regeneration.

5. Conclusion

In this study, we designed t-FDM scaffolds with inter-connected pores and substrate moduli varying from 5 – 266 MPa to investigate the effects of substrate modulus on healing in a rat subcutaneous wound model. We found that cellular infiltration, collagen deposition and directional variance, and angiogenesis were maximized for wounds treated with 3D-M scaffolds having an intermediate (24 MPa) substrate modulus. Healing was enhanced by down-regulation of Wnt/β-catenin signaling in fibroblasts as well as increased polarization of macrophages toward

the regenerative phenotype on the 3D-M scaffolds. These observations highlight the substrate modulus of the implanted scaffold as a key parameter regulating the regenerative versus scarring phenotype in wound healing.

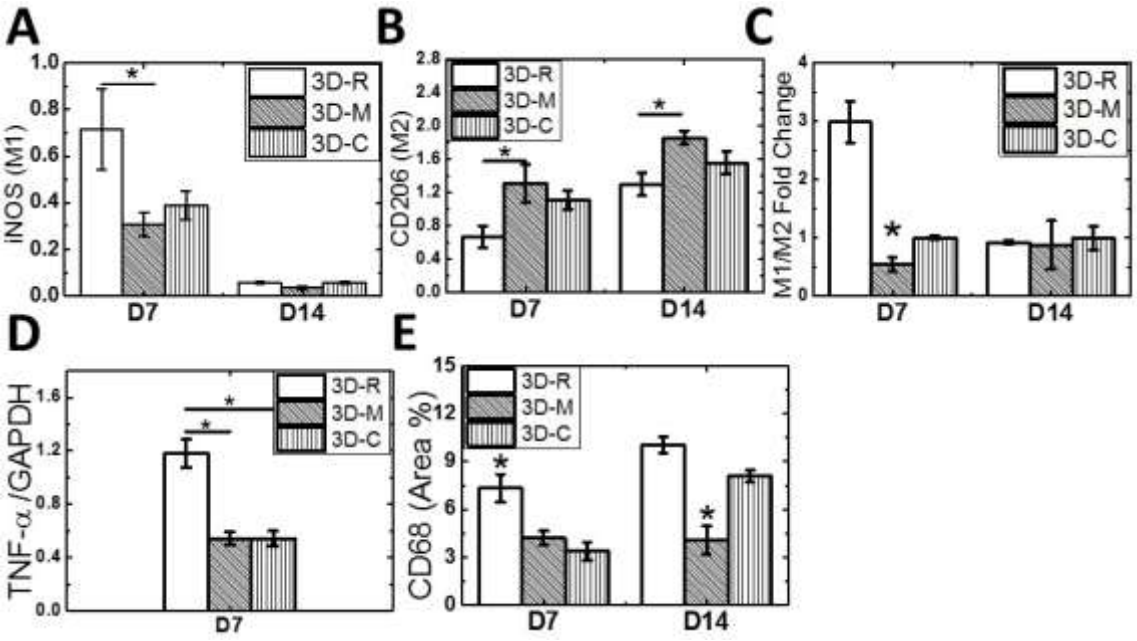

Figure 0.6 Effects of bulk modulus on macrophage polarization.

(A) Expression of the M1 phenotype marker *iNOS* was significantly lower on 3D-M scaffolds on D7. (B) Expression of the M2 phenotype marker CD206 was significantly higher on 3D-M scaffolds on D7 and D-14. (C) M1/M2 ratio was lowest on 3D-M scaffolds on D7. (D) Expression of the M1 marker TNF-α was lower on 3D-C and 3D-M scaffolds on D7. (E) The total number of macrophages, as assessed by CD68 immunohistochemical staining, was lowest on 3D-C and 3D-M scaffolds.

Acknowledgement

Research reported in this publication was supported by the National Institute of Arthritis and Musculoskeletal and Skin Diseases under Award Number AR056138, the National Cancer Institute under Award Number CA163499, and the Department of Veterans Affairs under Award Number

1I01BX001957. The content is solely the responsibility of the authors and does not necessarily represent the official views of the National Institutes of Health or the Department of Veterans Affairs.

Reference

[1] Lorden ER, Miller KJ, Bashirov L, Ibrahim MM, Hammett E, Jung Y, et al. Mitigation of hypertrophic scar contraction via an elastomeric biodegradable scaffold. Biomaterials 2015;43:61-70.
[2] Li B, Davidson JM, Guelcher SA. The effect of the local delivery of platelet-derived growth factor from reactive two-component polyurethane scaffolds on the healing in rat skin excisional wounds. Biomaterials 2009;30:3486-94.
[3] Ashraf A, Lee PH, Kim K, Zaporojan V, Bonassar L, Valentini R, et al. Effect of sustained-release PDGF and TGF-beta on cyclophosphamide-induced impaired wound healing. Plast Reconstr Surg 2009;124:1118-24.
[4] Pandit A, Ashar R, Feldman D. The effect of TGF-beta delivered through a collagen scaffold on wound healing. J Invest Surg 1999;12:89-100.
[5] Richardson TP, Peters MC, Ennett AB, Mooney DJ. Polymeric system for dual growth factor delivery. Nature Biotech 2001;19:1029 - 34.
[6] Singer AJ, Clark RA. Cutaneous wound healing. N Engl J Med 1999;341:738-46.
[7] Cao TV, Hicks MR, Standley PR. In vitro biomechanical strain regulation of fibroblast wound healing. The Journal of the American Osteopathic Association 2013;113:806-18.
[8] Smitha B, Donoghue M. Clinical and histopathological evaluation of collagen fiber orientation in patients with oral submucous fibrosis. Journal of oral and maxillofacial pathology : JOMFP 2011;15:154-60.
[9] McDougall S, Dallon J, Sherratt J, Maini P. Fibroblast migration and collagen deposition during dermal wound healing: mathematical modelling and clinical implications. Philosophical transactions Series A, Mathematical, physical, and engineering sciences 2006;364:1385-405.
[10] Zhang DL, Gu LJ, Liu L, Wang CY, Sun BS, Li Z, et al. Effect of Wnt signaling pathway on wound healing. Biochem Biophys Res Commun 2009;378:149-51.
[11] Hamburg EJ, Atit RP. Sustained beta-catenin activity in dermal fibroblasts is sufficient for skin fibrosis. J Invest Dermatol 2012;132:2469-72.
[12] Bielefeld KA, Amini-Nik S, Alman BA. Cutaneous wound healing: recruiting developmental pathways for regeneration. Cellular and molecular life sciences : CMLS 2013;70:2059-81.
[13] Januszyk M, Wong VW, Bhatt KA, Vial IN, Paterno J, Longaker MT, et al. Mechanical offloading of incisional wounds is associated with transcriptional downregulation of inflammatory pathways in a large animal model. Organogenesis 2014;10:186-93.
[14] Cheon SS, Cheah AY, Turley S, Nadesan P, Poon R, Clevers H, et al. beta-Catenin stabilization dysregulates mesenchymal cell proliferation, motility, and invasiveness and causes aggressive fibromatosis and hyperplastic cutaneous wounds. Proc Natl Acad Sci U S A 2002;99:6973-8.
[15] Novak ML, Koh TJ. Macrophage phenotypes during tissue repair. Journal of leukocyte biology 2013;93:875-81.
[16] Daley JM, Brancato SK, Thomay AA, Reichner JS, Albina JE. The phenotype of murine wound macrophages. Journal of leukocyte biology 2010;87:59-67.

[17] Nair MG, Gallagher IJ, Taylor MD, Loke P, Coulson PS, Wilson RA, et al. Chitinase and Fizz family members are a generalized feature of nematode infection with selective upregulation of Ym1 and Fizz1 by antigen-presenting cells. Infect Immun 2005;73:385-94.
[18] Loke P, Gallagher I, Nair MG, Zang X, Brombacher F, Mohrs M, et al. Alternative activation is an innate response to injury that requires CD4+ T cells to be sustained during chronic infection. Journal of immunology 2007;179:3926-36.
[19] Garg K, Pullen NA, Oskeritzian CA, Ryan JJ, Bowlin GL. Macrophage functional polarization (M1/M2) in response to varying fiber and pore dimensions of electrospun scaffolds. Biomaterials 2013;34:4439-51.
[20] Wong VW, Rustad KC, Akaishi S, Sorkin M, Glotzbach JP, Januszyk M, et al. Focal adhesion kinase links mechanical force to skin fibrosis via inflammatory signaling. Nat Med 2012;18:148-52.
[21] Adolph EJ, Hafeman AE, Davidson JM, Nanney LB, Guelcher SA. Injectable polyurethane composite scaffolds delay wound contraction and support cellular infiltration and remodeling in rat excisional wounds. J Biomed Mater Res A 2012;100A:450-61.
[22] Guelcher SA, Patel V, Gallagher KM, Connolly S, Didier JE, Doctor JS, et al. Synthesis and in vitro biocompatibility of injectable polyurethane foam scaffolds. Tissue Engineering 2006;12:1247-59.
[23] Fonck E, Feigl GG, Fasel J, Sage D, Unser M, Rufenacht DA, et al. Effect of aging on elastin functionality in human cerebral arteries. Stroke 2009;40:2552-6.
[24] Rezakhaniha R, Agianniotis A, Schrauwen JT, Griffa A, Sage D, Bouten CV, et al. Experimental investigation of collagen waviness and orientation in the arterial adventitia using confocal laser scanning microscopy. Biomechanics and modeling in mechanobiology 2012;11:461-73.
[25] Hafeman A, Li B, Yoshii T, Zienkiewicz K, Davidson J, Guelcher S. Injectable biodegradable polyurethane scaffolds with release of platelet-derived growth factor for tissue repair and regeneration. Pharm Res 2008;25:2387-99.
[26] Quinn KP, Golberg A, Broelsch GF, Khan S, Villiger M, Bouma B, et al. An automated image processing method to quantify collagen fibre organization within cutaneous scar tissue. Experimental dermatology 2015;24:78-80.
[27] Beer HD, Longaker MT, Werner S. Reduced expression of PDGF and PDGF receptors during impaired wound healing. J Invest Dermatol 1997;109:132-8.
[28] Galeano M, Altavilla D, Cucinotta D, Russo GT, Calo M, Bitto A, et al. Recombinant human erythropoietin stimulates angiogenesis and wound healing in the genetically diabetic mouse. Diabetes 2004;53:2509-17.
[29] Bonanno E, Iurlaro M, Madri JA, Nicosia RF. Type IV collagen modulates angiogenesis and neovessel survival in the rat aorta model. In vitro cellular & developmental biology Animal 2000;36:336-40.
[30] Rustad KC, Wong VW, Gurtner GC. The role of focal adhesion complexes in fibroblast mechanotransduction during scar formation. Differentiation; research in biological diversity 2013;86:87-91.

[31] Brancato SK, Albina JE. Wound macrophages as key regulators of repair: origin, phenotype, and function. Am J Pathol 2011;178:19-25.
[32] van Putten SM, Ploeger DT, Popa ER, Bank RA. Macrophage phenotypes in the collagen-induced foreign body reaction in rats. Acta Biomater 2013;9:6502-10.
[33] Sephel GC, Davidson JM. Repair, regeneration and fibrosis. In: Rubin R, Strayer DS, editors. Rubin's Pathology: Clinicopathologic Foundations of Medicine. 6th ed. Philadelphia, PA: Lippincott Williams and Wilkins; 2012. p. 83-114.
[34] Cao H, McHugh K, Chew SY, Anderson JM. The topographical effect of electrospun nanofibrous scaffolds on the in vivo and in vitro foreign body reaction. J Biomed Mater Res A 2010;93:1151-9.
[35] Chong EJ, Phan TT, Lim IJ, Zhang YZ, Bay BH, Ramakrishna S, et al. Evaluation of electrospun PCL/gelatin nanofibrous scaffold for wound healing and layered dermal reconstitution. Acta Biomater 2007;3:321-30.
[36] Adolph EJ, Hafeman AE, Davidson JM, Nanney LB, Guelcher SA. Injectable polyurethane composite scaffolds delay wound contraction and support cellular infiltration and remodeling in rat excisional wounds. Journal of biomedical materials research Part A 2012;A100A:450-61.
[37] Wilgus TA, DiPietro LA. Complex roles for VEGF in dermal wound healing. J Invest Dermatol 2012;132:493-4.
[38] Duscher D, Maan ZN, Wong VW, Rennert RC, Januszyk M, Rodrigues M, et al. Mechanotransduction and fibrosis. J Biomech 2014;47:1997-2005.
[39] Hafeman AE, Zienkiewicz KJ, Zachman AL, Sung HJ, Nanney LB, Davidson JM, et al. Characterization of the degradation mechanisms of lysine-derived aliphatic poly(ester urethane) scaffolds. Biomaterials 2011;32:419-29.
[40] Lynch SE, Nixon JC, Colvin RB, Antoniades HN. Role of platelet-derived growth factor in wound healing: Synergistic effects with other growth factors. Proc Natl Acad Sci USA 1987;84:7696-700.
[41] Stockmann C, Kirmse S, Helfrich I, Weidemann A, Takeda N, Doedens A, et al. A wound size-dependent effect of myeloid cell-derived vascular endothelial growth factor on wound healing. J Invest Dermatol 2011;131:797-801.
[42] El Gazaerly H, Elbardisey DM, Eltokhy HM, Teaama D. Effect of transforming growth factor Beta 1 on wound healing in induced diabetic rats. International journal of health sciences 2013;7:160-72.
[43] Akasaka Y, Ono I, Kamiya T, Ishikawa Y, Kinoshita T, Ishiguro S, et al. The mechanisms underlying fibroblast apoptosis regulated by growth factors during wound healing. The Journal of pathology 2010;221:285-99.
[44] Cheon S, Poon R, Yu C, Khoury M, Shenker R, Fish J, et al. Prolonged beta-catenin stabilization and tcf-dependent transcriptional activation in hyperplastic cutaneous wounds. Laboratory investigation; a journal of technical methods and pathology 2005;85:416-25.
[45] Amini-Nik S, Glancy D, Boimer C, Whetstone H, Keller C, Alman BA. Pax7 expressing cells contribute to dermal wound repair, regulating scar size through a beta-catenin mediated process. Stem Cells 2011;29:1371-9.

[46] Penn JW, Grobbelaar AO, Rolfe KJ. The role of the TGF-beta family in wound healing, burns and scarring: a review. International journal of burns and trauma 2012;2:18-28.
[47] Carre AL, James AW, MacLeod L, Kong W, Kawai K, Longaker MT, et al. Interaction of wingless protein (Wnt), transforming growth factor-beta1, and hyaluronan production in fetal and postnatal fibroblasts. Plast Reconstr Surg 2010;125:74-88.
[48] Lam AP, Gottardi CJ. beta-catenin signaling: a novel mediator of fibrosis and potential therapeutic target. Current opinion in rheumatology 2011;23:562-7.
[49] Cheon SS, Wei Q, Gurung A, Youn A, Bright T, Poon R, et al. Beta-catenin regulates wound size and mediates the effect of TGF-beta in cutaneous healing. FASEB J 2006;20:692-701.
[50] Sindrilaru A, Scharffetter-Kochanek K. Disclosure of the Culprits: Macrophages-Versatile Regulators of Wound Healing. Adv Wound Care (New Rochelle) 2013;2:357-68.

CHAPTER 6

CROSSTALK BETWEEN INTEGRIN-β1 AND BMPR1A MEDIATES MATRIX RIGIDITY REGULATED MSC OSTEOGENESIS

1. Introduction

The development of materials for bone replacement has attracted much attention, as extensive bone loss caused by trauma or tumor will result in failure of bone repair[1]. Both autograft and allograft have been used for treating bone defects, yet the limited supply and potential health risk have limited their use for bone tissue repair[2]. Because of their tunable chemical and physical properties[3], polymer scaffolds have been employed for bone defects treatment. In addition to providing temporary support for impaired bone tissues, researchers have been incorporating biological cues into scaffolds to enhance the host tissue response and improve healing[4]. Cell therapy has been considered a promising solution for improved bone regeneration due to the potential of self-renewal and enhancement of osteogenic differentiation, especially for patients who experience fracture nonunion and metabolic bone diseases, such as osteogenesis imperfecta and hypophosphatasia[5],[6]. However, questions remain regarding the relative contribution of transplanted mesenchymal stem cells (MSCs) to bone regeneration. Without specific biological signals, the delivered mesenchymal stem cells do not substantially improve bone repair by direct differentiation to osteoblasts. Although it has been reported and widely accepted that the delivered regenerative cells are able to enhance bone repair by the recruitment and differentiation of tissue-specific stem cells through secretion of soluble factors, the secreted soluble factors must be in

sufficient amounts to function at the wound site, which is a concern due to possible toxic effects of MSCs as well as migration to other anatomical sites[5].

In order to overcome these limitations, the application of bone morphogenetic proteins (BMPs) to treatment of open fractures has been investigated, since they have been shown to up-regulate the BMP signaling pathway that is crucial for bone regeneration and enhance osteogenesis[7]. BMPs are subfamily of transforming growth factor beta (TGF-β) that are closely associated with the growth, maturation, and regulation of bone tissues[8]. Studies have previously suggested that BMP signaling is required for endochondral ossification, maintenance of the adult skeleton, and regeneration of bone. Among BMPs, previous studies have shown that BMP2 plays essential roles in bone regeneration[9]. Moreover, the recombinant human BMP2 (rhBMP2) supplied delivered from a bovine collagen sponge carrier has been approved by the US Food and Drug Administration (FDA) for clinical application[10]. However, multiple adverse events, complications, and concerns associated with rhBMP2 usage has also been reported recently[11],[12]. Therefore, to improve the safety of rhBMP2 treatment, it is important to find out alternative methods to enhance osteoblast BMP signaling by reducing the dose of BMP2.

The osteoblastic differentiation of mesenchymal stem cells is regulated by mechanical signaling, and the mechanism of mechanotransduction in response to substrate stiffness has been partially clarified. However, previous studies investigating the cellular response to substrate rigidity have utilized substrates with elastic moduli less than 100 MPa[13], and only a limited number of studies have investigated the effects of modulus on osteogenic differentiation using rigid substrates approximating trabecular bone (100 – 400 MPa[14]). Expression of the osteogenic

transcription factor *Runx2* and the osteoblast marker alkaline phosphatase (*ALP*) increased with 2D substrate rigidity when MC3T3-E1 pre-osteoblasts were cultured on PEG-diacrylate hydrogels (600 kPa) or tissue culture polystyrene (2000 MPa)[15]. RhoA activity increased on stiffer substrates, thereby promoting increased cellular contractility through ROCK. A later study reported that for 2D acrylate films with moduli ranging from 5–850 MPa, the composition of the polymer had a more significant effect on differentiation than the modulus, prompting the authors to challenge the notion that cells can sense rigidity in the range of trabecular bone. In our previous study on MSC osteogenesis, we designed the 3D polyurethane scaffolds with substrate rigidity from the MPa to the GPa range, and demonstrated enhanced osteoblastic differentiation and mineralization on the rigid scaffolds. However, the mechanism was not investigated. Thus, clarification of the mechanism of enhanced osteoblast differentiation on rigid bone-like substrates will help guide the further optimization of rhBMP2 or cell delivery systems.

To initiate the activation of RhoA/ROCK signaling, integrin-mediated cell-matrix interactions generate an adhesion molecule-integrin-actomyosin complex that can be shifted between inactive and signaling states by activation of myosin II or matrix rigidity [22]. Cells appear to sense matrix rigidity based on whether a critical force is generated by displacing the matrix a distance of 100 – 150 nm [23-25]. However, it has been suggested that cells interacting with matrices with elastic moduli >100 kPa are in a state of isometric contraction [26] and cannot displace the matrix. Thus, the previously reported correlations of MSC proliferation and differentiation with rigidity over ranges comparable to mineralized bone (10^3 – 10^6 kPa) cannot be explained by uniform displacements of the matrix. These observations further raise questions regarding the

mechanisms by which matrix rigidity regulates MSCs gene expression during the mature of osteoblasts.

In this study, we investigated osteogenic differentiation and mineralization of rat bone marrow derived mesenchymal stem cells in response to polyurethane substrates with moduli exceeding 100 MPa. We hypothesized that enhanced osteogenesis on substrates with bone-like rigidity is mediated by integrins, but not by the uniform displacements of the matrix conventionally associated with mechanotransduction. During epithelial-mesenchymal transition (EMT), TGF-β Receptor type II (TGF-β RII) interacts physically with β3 integrin sub-unit (Iβ3) to enhance TGF-β-mediated stimulation of MAP-kinases (MAPKs) in mammary epithelial cells (MECs) [30]. However, the role of matrix rigidity in promoting interactions between these receptors has not been explored. We used a 2D polyurethane (PUR) film monoculture system to design matrices with rigidities ranging from that of the basement membrane to cortical bone. *In vitro* studies demonstrated that *Iβ1* expression correlated with bone-like rigidity, which led to co-localization of Iβ1 with type 1 BMP receptor (BMPRI) and increased expression of osteogenic genes. Genetic interference of MSC-expressed Iβ1 or inhibition of type 1 BMP receptor kinase significantly decreased the expression of osteogenic genes in vitro.. These observations provide evidence for a previously unexplored mechanism by which crosstalk between solid-state and soluble factor signaling switches on BMP signaling in rat bone marrow-derived MSCs.

2. Materials and Methods

2.1 Materials

DMEM (1.0 g/L glucose = 1.0 g/L) and fetal bovine serum (FBS) were purchased from Thermo Scientific. Penicillin/streptomycin (P/S), trypsin EDTA, and Amphotericin B were obtained from Corning Cellgro. Glycolide and D,L-lactide were purchased from Polysciences (Warrington, PA). Hexamethylene diisocyanate trimer (HDIt) was supplied by Bayer Material Science (Pittsburgh, PA). Iron acetylacetonate (FeAA) catalyst and Dorsomorphin was supplied by Sigma-Aldrich. ε-caprolactone (Sigma-Aldrich) was dried over anhydrous $MgSO_4$, and all other materials were used as received.

2.2 Fabrication and characterization of 2D PUR films

Polyester triols (300 g/mol, 450 g/mol, 720 g/mol or 3000 g/mol) were synthesized from a glycerol starter and a backbone comprising ε-caprolactone, glycolide, and D,L-lactide as described previously[16]. Polyurethane (PUR) films were synthesized by reactive liquid molding of HDIt with a hardener component comprising the polyester triol and iron catalyst (5% iron acetylacetonate (FeAA) in dipropylene glycol). The reactants were poured into tissue culture plate right after mixing and cured in oven under 60 ℃ overnight. The bulk moduli of all the synthesized 2D films were measured under compression by MTS.

2.3 Cell culture and osteoblastic induction

Primary rat bone marrow mesenchymal stem cells (BMSCs) were generated from pooled bone marrow from femurs of n = 4 Sprague-Dawley rats. BMSCs were maintained in DMEM with 10% FBS, 1% P/S, and 0.1% Amphotericin B (Sigma). Cells were detached at sub-confluency by

trypsin EDTA (0.25%) and re-suspended at 2×10^5/mL in complete medium and cultured on 2D PUR films. To facilitate cell attachment, all the PUR sheets were pre-soaked in fibronectin solution (4 μg/mL) in cell culture incubator for 24 h. After seeding, cells were cultured in complete medium in 12-well plates until confluent and then changed to osteoinductive medium for osteoblast differentiation (10 nM dexamethasone, 50 μg/mL ascorbic acid and 0.1 mM β-glycerophosphate) with or without rhBMPs. Cells were detached by trypsin EDTA (0.25%) at D4, D7, and D14, and total RNA was isolated from the harvested cell pellets by RNeasy mini Kit (Qiagen). cDNA synthesis was carried out from purified total RNA using iScript™ Reverse Transcription Supermix (Biorad). RT-PCR amplified for osteogenesis genes were measured to compare the differentiation of osteoblast. The primer used for RT-PCR amplification was listed in Table 6.1.

2.4 Western Blotting

PUR films of different rigidities were synthesized in 6-well tissue culture plates as described above and incubated in complete cell culture medium overnight to facilitate cell attachment. Rat bone marrow derived mesenchymal stem cells were plated on PUR-coated tissue culture plates and cultured with or without osteogenic induction. Cells were detached by trypsin EDTA (0.25%) and total protein extracted from cell pellets by RIPA buffer (Thermo scientific) containing protease inhibitors and phosphatase inhibitors (Thermo scientific) on ice for 15 min. Protein concentration was measured by Pierce BCA Protein Assay Kit (Thermo scientific). Cell lysates were then centrifuged at full speed for 15 min to remove cellular debris at 4℃. Equal amounts of total protein

were loaded onto SDS-PAGE gels, separated by Bio-rad 2-D Electrophoresis units, and transferred to PVDF membranes. The membrane was blocked in LI-COR preformed blocking buffer for 1h at room temperature and then incubated with primary antibodies in blocking buffer at 4℃ with gentle shaking overnight. Proper HRP-conjugated sencondary antibodies were then applied to the membranes after harshly wash and signals were detected by Western Lightning Chemiluminescent (PerkinElmer). Primary and secondary antibodies utilized in this study is listed in Table 6.2

Table 0.1 Primer sequence of osteoblastic genes

Marker	Forward 5' to 3'	Reverse 5' to 3'
Runx2	TCCAGACCAGCAGCACTCC	GTTATGAAAAACCAAGTAGCCAGGT
OSX	GGAGGTTTCACTCCATTCCA	TAGAAGGAGCAGGGGACAGA
OPN	AGTGGTTTGCCTTTGCCTGTT	TCAGCCAAGTGGCTACAGCAT
ITGB1	GAGAGAGATTACTTCAGAC	AGCAGTCGTGTTACATTC
ALP	AAGGACATCGCATATCAG	TCTCATCCAGTTCGTATTC
GAPDH	GACTTCAACAGCAACTCC	GCCATATTCATTGTCATACCA
BMPR1A	GGCCATTGCTTTGCCATTATAG	CTTTCGGTGAATCCTTGCATTG

Table 0.2 Antibodies applied

Antibody	Species	Supplier
pMAPK	Rabbit	Cell signaling
MAPK	Rabbit	Cell signaling
pSMAD1,5	Rabbit	Cell signaling
SMAD1,5	Rabbit	Santa cruz
pFAK	Rabbit	Cell signaling
FAK	Rabbit	Cell signaling
ITGB1	Rabbit	Santa cruz
GAPDH	Goat	Santa cruz
BMPR1	Rabbit	Santa cruz
Anti-rabbit	Goat	Santa cruz
Anti-goat	Donkey	Santa cruz

2.5 Immunoprecipitation

Cells were cultured and treated as described in Western blotting. Pierce Crosslink IP Kit was utilized to conduct the immunoprecipitation process and eliminate interference of IgG from the precipitation antibody. The procedure of immunoprecipitation was following the manual provided by the kit. Briefly, harvested cells were lysed with the mild lysis buffer under low temperature and equal amount of total proteins were incubated with BMPR1 antibody to precipitate type 1 BMP receptors and any other cell components that are physically linked to the receptors. The precipitated proteins were detached by mild elution buffer and the eluted proteins were then denatured and loaded onto SDS-PAGE gels, separated by Bio-rad 2-D Electrophoresis units, and transferred to PVDF membranes. Detection of type 1 BMP receptor bounded proteins were performed the same way as western blotting.

2.6 Nucleus fractionation

Cell were plated and cultured on PUR films for designated times and then detached by trypsin/EDTA, and cell number for each sample was counted and recorded. A NE-PER Nuclear and Cytoplasmic Extraction Reagents kit (Thermo) was utilized for the application of nucleus fractionation and the process was following the kit's manual. Briefly, after getting harvested cell pellets, cells were first lysed by Cytoplasmic Extraction Reagent to collect cytoplasmic proteins and then totally lysed by Nuclear Extraction Reagent to take out the nucleus protein compartment. After fractionation, measure protein concentrations for each sample by BCA protein kit and then conduct western blotting as described above.

2.7 Förster resonance energy transfer (FRET)

To investigate the association of type 1 BMP receptor and Iβ1, we performed Förster Resonance Energy Transfer (FRET). Briefly, the donor antibody (anti Iβ1 (SantaCruz)) was labeled with Alexa Fluor® 488 Carboxylic Acid, Succinimidyl Ester (Life Technologies) (Iβ1-488) and the acceptor antibody (anti TGF-β RII (SantaCruz)) was labeled with Alexa Fluor® 546 Carboxylic Acid, Succinimidyl Ester (Life Technologies) (BMPRI-546) in a 2.25:1 molar ratio of antibody:dye overnight at 4˚C. Labelled antibody was purified with size exclusion chromatography using PD-10 Desalting Columns (GE Healthcare). Rat MSCs were plated on pre-soaked films of rigid and compliant 2D PURs. After 24 hours of culture, cells were fixed with 10% Formaldehyde in PBS and stained overnight at 4˚ with Iβ1-488, and Iβ1-488 + BMPRI-546 (1ug/1x10^6 cells). FRET experiments were performed on a BioTek Synergy 2 plate reader using excitation filter 485/20 and emission filter 530/35.

2.8 Iβ1 Transduction and knockdown by siRNA treatment

The amplified ITGB1 coding sequence was cloned and transferred into the pGEM-T vector by *in vitro* recombination using Lipofectamine 3000 (Life Technology) following its manuscript manual. A siRNA encoding sequence for rat cells were purchase from Santa Cruz and Lipofectamine RNAiMAX was applied for knockdown treatment.

2.9 Statistics

The statistical significance between experimental groups was determined by Student's *t test* or by

a two-factor ANOVA. Graphs show mean ± S.D., and $p \leq p < 0.05$ is considered as statistically significant.

3. Result

3.1 Rat bone marrow derived mesenchymal stem cells osteogenic differentiation was correlated with substrate righty in the MPa to GPa range

PUR films were directly cast in tissue culture plates as substrates for MSC culture. We developed different formulations for PUR synthesis by modifying the molecular weight of the polyester triol component to synthesize films with moduli ranging from 10 MPa to 2 GPa (Fig. 6.1A) while maintaining a constant contact angle (data not shown). Rat bone marrow derived MSCs were plated on PUR films, which were pre-incubated in a solution of fibronectin (4 ug/mL) to facilitate cell attachment. Osteogenic induction medium was applied to MSC culture after the cells reached confluence in complete cell culture medium. Gene expression level of the transcription factor *Runx2* was evaluated 3 days after the initiation of osteoblastic induction and was shown to be dose-responsive to the modulus of the PUR film (Fig. 6.1B), suggesting that substrate rigidity regulates MSC differentiation beyond the MPa range. We then conducted a time-course osteogenic differentiation study for MSCs plated on the rigid and compliant PUR films, in which both ALP gene expression and its activity were measured from D4 to D14 and they were both significantly increased on the rigid films (Fig. 6.1C, D). After osteogenic induction for 21 days, cells cultured on the rigid and compliant PUR films were fixed on the films and Alizarin red S staining was performed on both groups. As shown in Fig. 6.1E, increased mineral deposition

was observed on the rigid PUR films and the mineral nodules were significantly larger, suggesting increased differentiation of mature osteoblasts.

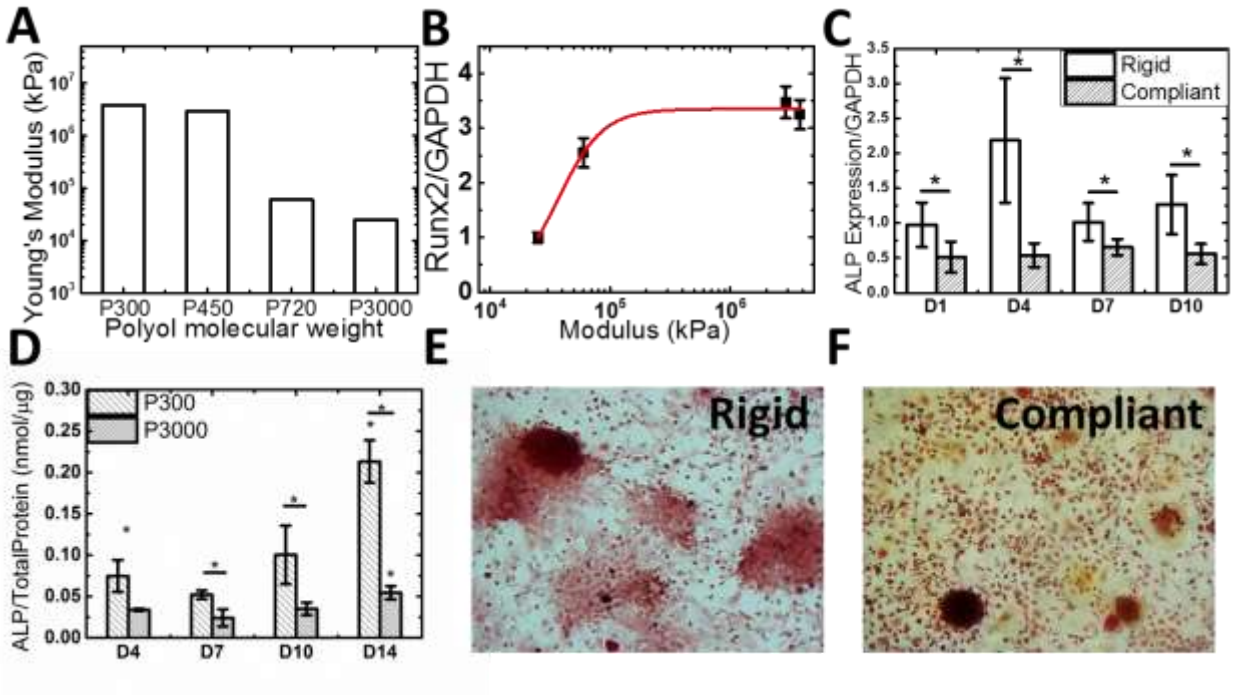

Figure 0.1 Rat bone marrow derived mesenchymal stem cell on PUR films of varied rigidities. (A) A series of varied rigidities of generated PUR films. (B) The expression level of transcriptional factor Runx2 in response to substrate rigidities. (C, D) The alkaline phosphatase gene expression and enzyme activity in response to rigid and compliant PUR substrate. (E, F) Alizarin S staining of formed mineral nodules of osteoblastic induced MSCs layers on rigid and compliant PUR films.

3.2 Kinase P44/42 and Smad 1/5 mediated MSCs rigidity responsive osteogenesis

Mechanotransduction effects on osteogenic differentiation of MSCs requires the activity of MAPK 44/42 when the substrate rigidity ranges from 1 – 100 kPa[17],[18],[19],[20]. Thus, we investigated the same kinase signaling pathway to see if MSCs were able to respond to the high substrate rigidities (10 MPa to 1 GPa) through the same signaling cascade. Activation of MAPK

44/42 was evaluated by the measurement of phosphorylated MAPK 44/42 protein by western blotting. As shown in Fig. 6.2A, as early as 16 hr after plating MSCs on PUR films, activation of the kinase was up regulated on the rigid films. After 4 days culture on films of different rigidities, the difference of phosphorylated MAPK 44/42 between two groups was further enlarged (Fig. 6.2A), indicating the continuing increased osteogenesis on the rigid PUR films. To further understand this outside-in pathway, we also evaluated SMAD 1/5 protein activation, which was previously shown to be highly interactive with MAPK pathways and activated by the BMP signaling pathway[21],[22],[23],[24]. After separating phosphorylated SMAD 1/5 trafficked to the nucleus from total protein lysate by nucleus fractionation, we observed that there were significantly increased phosphorylated-SMAD 1/5 proteins trafficked to the nucleus when cultured on the rigid PUR films (Fig. 6.2B, C), indicating the possibility that the osteogenic response of MSCs to substrate rigidity crosstalks with the BMP signaling pathway.

3.3 FAK expression increased with substrate rigidity but not for FAK phosphorylation

Since extracelluar mechanical stimuli can be transduced to intracellular signaling pathways by the activation of FAK[25] as well as MAPK 44/42 during osteogenesis[26], we determined the expression of FAK in rat MSCs in response to substrate rigidity to understand the mechanism of the outside-in signaling pathway. Rat MSCs were cultured on PUR films and total protein lysates were analyzed by western blotting to study the expression level of total FAK. As shown in Fig. 6.2D, the expression of FAK was significantly up-regulated on the rigid substrate. However, when

evaluating phosphorylated-FAK protein, comparable phosphorylated protein amounts between groups were determined. Combining these results together, rat MSCs plated on substrates more rigid than 100 MPa were still able to respond the mechanical stimuli, and gene expression in the cytoskeleton compartment was increased in response to the biomechanical cues. However, considering that the amount of phosphorylated FAK was the same on rigid and compliant substrates, the substrate rigidity was not able to further activate the kinase, suggesting that the cellular response to mechanical stimuli must be driven by other molecular cues other than the activation of FAK.

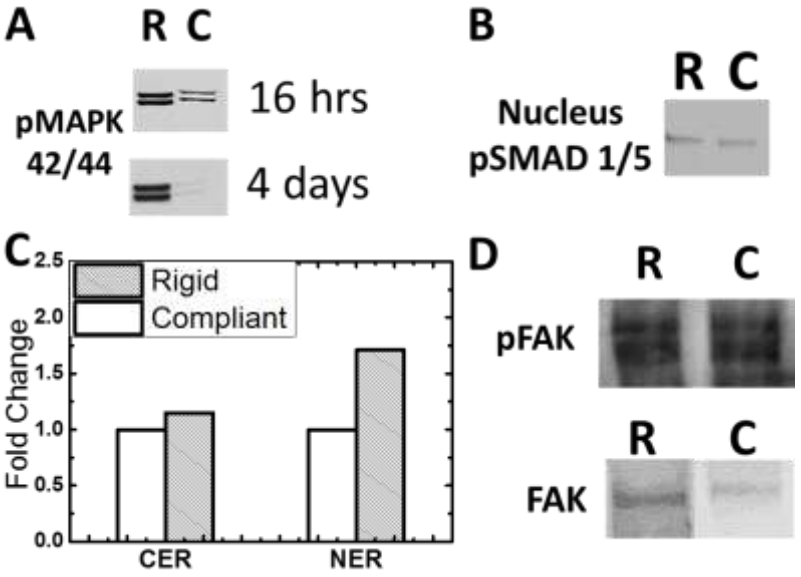

Figure 0.2 Expression and activities of mechanotransduction related kinase in response to rigid and compliant PUR films developed in this study.

(A) Time-course activation of phosphorylated MAPK 44/42 in response to PUR film rigidities. (B, C) Activated SMAD 1/5 at membrane (CER) and transferred to nucleus (NER) in response to PUR film rigidities. (D) Total and activated focal adhesion kinase (FAK) in response to substrate rigidities.

3.4 Iβ1 mediated MSCs osteogenesis by rigidity correlated physical interaction between Iβ1 and type 1 BMP receptor

Since integrins are an important anchor protein for MSC growth, we evaluated the role of *Iβ1* in mediating the cellular response to substrate rigidity, considering previous studies have reporting that *Iβ1* is required for MSC osteoblastic differentiation. As shown in Fig. 6.3A and 6.3B, the expression of *Iβ1* showed a sigmoidal dose response to substrate rigidity. Comparing the dose response of *Iβ1* expression (Fig. 6.3A, B) and the osteogenic transcription factor *Runx 2* (Fig. 6.1B) to substrate rigidity, the same response curve shape suggested the correlation of osteogenic differentiation with *Iβ1* expression. Considering that the response of phosphorylated SMAD 1/5 to substrate rigidity indicated the activation of the BMP signaling pathway, we then studied the involvement of BMP receptors. No significant difference was detected in expression of type 1 BMP receptor for MSCs plated on the rigid/compliant films (data not shown). Thus crosstalk between *Iβ1* and type 1 BMP receptor as a function of substrate rigidity was investigated in this study. With the application of immunoprecipitation (IP), we found that there is a physical interaction between *Iβ1* and type 1 BMP receptor (Fig. 6.3C), which increases with substrate rigidity over the range from 10 MPa to GPa. To further confirm the physical complexation as well as the rigidity dose response, förster resonance energy transfer (FRET) was also performed in this study. As shown in Fig. 6.3D, the labeled *Iβ1* (donor in the FRET system) and type 1 BMP receptor (receptor) complexes were significantly increased on the cell membrane of MSCs when plated on the rigid PUR films, which further substantiates the physical interactions between *Iβ1* and type 1 BMP receptor with increasing rigidity.

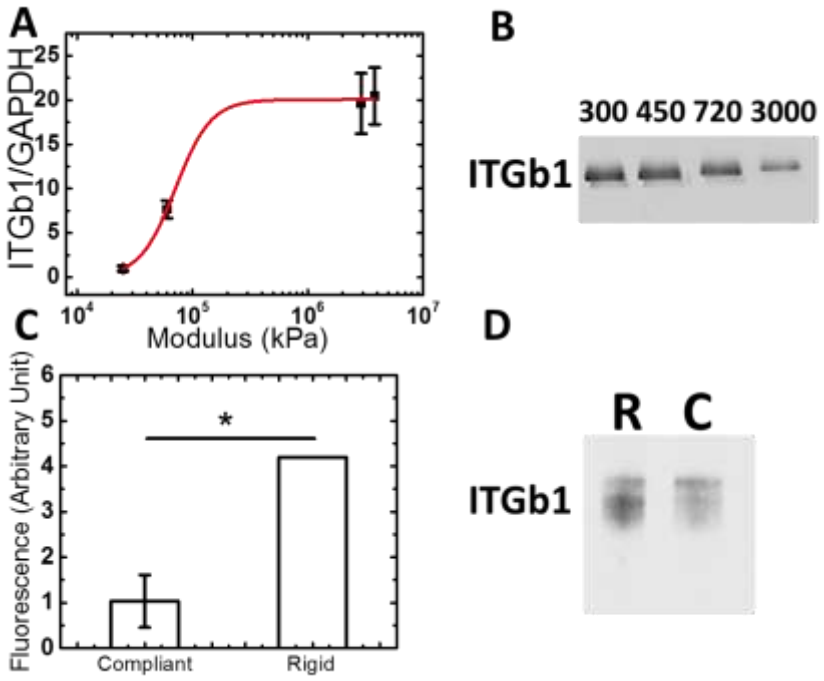

Figure 0.3 Substrate rigidity correlated physical interaction between Iβ1 and type 1 BMP receptor.

(A, B) Iβ1 gene and protein expression in response to substrate rigidities. (C) FRET readout of MSCs on the compliant and rigid PUR films. (D) Immunoprecipation of physically bonded Iβ1 and type 1 BMP receptor. The proteins were incubated and selected with BMPRI receptor bonded beads and the collected proteins were blotted with anti- Iβ1 antibody.

3.5 Iβ1 expression regulates osteogenic gene expression by MSCs

In order to isolate *Iβ1* protein level from the rigid substrates, we plated MSCs on tissue culture plates and inhibited *Iβ1* expression with siRNA (Fig. 6.4A). After *Iβ1* expression was knocked down >90%, MSCs were cultured to confluency and then treated to induce osteoblastic differentiation. The expression of *Runx 2* and *Osx* was evaluated after 5 days of induction, and was inhibited when *Iβ1* was knocked down (Fig. 6.4B). Similarly, phosphorylated SMAD 1/5 was also

compared with/without siRNA treatment and its trafficking to the nucleus was also significantly decreased (Fig. 6.4C, 6.4D), verifying the direct correlation between *Iβ1* expression and the BMP signaling pathway. Next, MSCs were then transduced with *Iβ1* plasmid and osteogenic induction was performed on the tissue culture plate. Increased *Runx 2* expression was detected with the up regulation of Integrin b1 (Fig. 6.4E). These results indicate that increased *Iβ1* enhances osteogenic differentiation of MSCs on substrates with rigidities over 100 MPa.

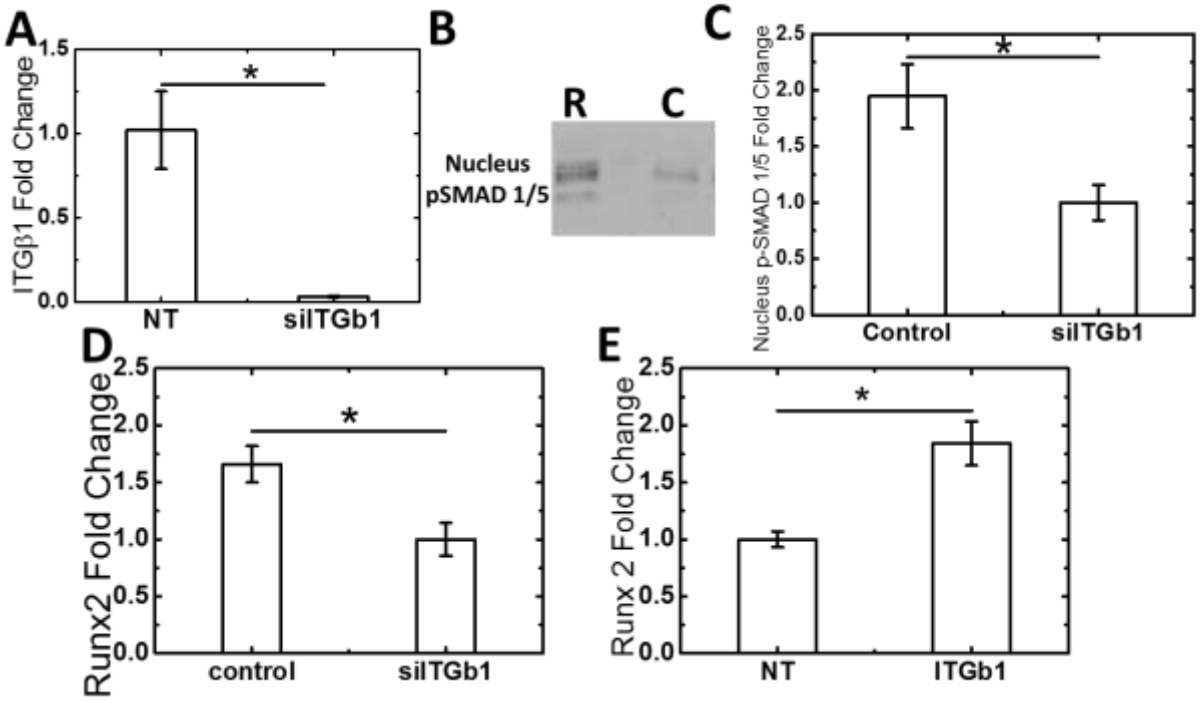

Figure 0.4 Rat bone marrow derived MSCs osteogenesis process is regulated by Iβ1 expression.

(A) siRNA knockdown of Iβ1 expression. (B, C) Decreased activated SMAD 1/5 toward nucleus after knocking down Iβ1. (D) Inhibited gene expression level of osteogenic transcriptional factor *Runx2* along with Iβ1 knockdown. (E) Increased gene expression level of osteogenic transcriptional factor *Runx2* along with Iβ1 overexpression.

3.6 Inhibiting the activity of type 1 BMP receptor hindered MSC osteogenesis and eliminated the rigidity response

Although we have shown in this study that osteogenic differentiation of rat MSCs was affected by *Iβ1* expression in a dose-responsive manner, in order to identify the direct involvement of type 1 BMP receptors in the mechanotransduced osteoblastic differentiation, we utilized a type 1 BMP receptor kinase inhibitor (dorsormorphin) to isolate the effects of substrate rigidity and osteogenic induction through BMP receptor stimuli. The expression of *Runx 2* and the osteoblast marker *OPN* were evaluated after dorsormorphin treatment, and as is shown in Fig. 6.5A both genes were significantly inhibited, indicating the requirement of type 1 BMP receptors in MSC osteogenesis even without addition of BMP ligands. To further evaluate the involvement of type 1 BMP receptor in *Iβ1* mediated osteogenesis, rat MSCs were plated on both rigid and compliant PUR films and treated with the receptor kinase inhibitor. After 7 days osteogenic induction, the difference between MSCs on rigid and compliant PUR films decreased with the inhibition of type1 BMP receptor kinase, further indicating the involvement of the receptor. To determine whether *Iβ1* contributes to osteogenesis through BMP signaling pathway, siRNA was utilized to knock down its expression and BMP2 ligand was added to cell culture. When *Iβ1* was silenced, the osteogenic stimuli of BMP2 was eliminated (Fig. 6.5B).

3.7 Effects of substrate rigidities and BMP2 ligands on MSCs osteogenesis are through the same cascade pathway

The involvement of BMP receptors in substrate rigidity dose responsive osteogenic

differentiation investigated in this study suggested the possibility of enhancing the effects of BMP2 delivery for bone regeneration by increasing the elastic modulus of BMP2 carriers. Therefore, rat MSCs were plated on rigid and compliant PUR films and treated with BMP2 ligands of varied concentration. Expression of *Runx2* was monitored and compared between groups to evaluate MSC osteoblastic differentiation. As shown in Fig. 6.5C, with the increase of exogenous BMP2 concentration, the difference between MSCs plated on the rigid and compliant PUR films was eliminated, further indicating that the effects of substrate rigidity and BMP ligand concentration are transduced in cells through the same signaling cascade and are additive to each other.

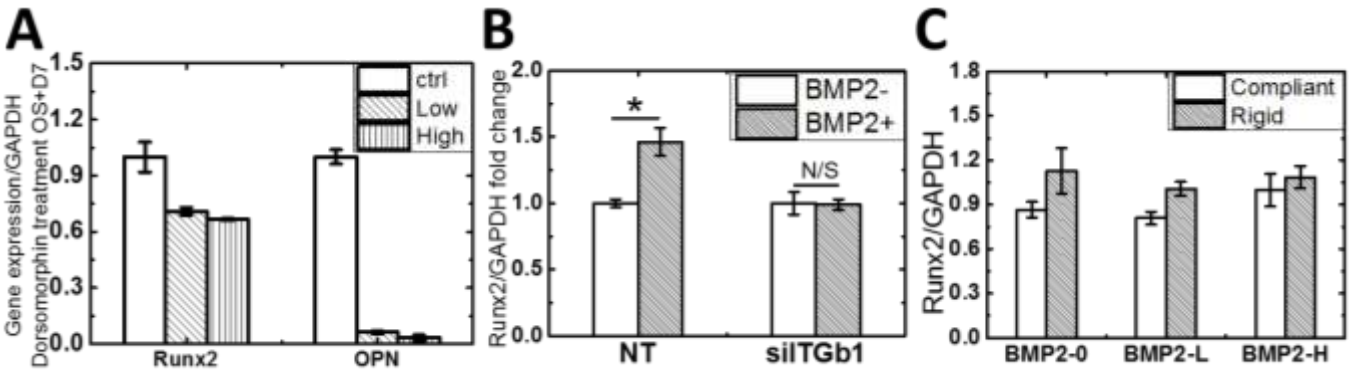

Figure 0.5 Involvement BMP signaling pathway in the substrate regulated osteogenesis.
(A) Decreased expression of osteogenesis related genes with the inhibition of BMPRI kinase phosphorylation. (B) Silencing Iβ1 eliminated the rhBMP2 osteogenic induction. (C) Osteogenic transcriptional factor *Runx2* expression is able to be enhanced by either substrate rigidity or additive BMP2 ligands and with higher rigidity, lower BMP2 dosed was required to achieve the same expression level.

4. Discussion

Although it has been reported that integrins are the key factors mediating

mechanotransduction in MSCs, the mechanism of how integrins modulate osteogenesis in response to substrate rigidity has remained unclear[27],[28]. Integrins crosstalk with multiple signaling pathways, including BMP signaling through FAK phosphorylation[29]. However, other than the conventional outside-in signaling cascade pathways through the activation of a series of an integrin-bound kinase, the physical interaction of BMP receptors with *Iβ1* sub-unit has never been reported. In this study, we formulated PUR substrates with rigidities exceeding 100 MPa and showed that while the expression of FAK increased with rigidity, its activation stayed constant, possibly as a result of the inability of the adherent MSCs to deform the substrate. This observation raises questions about how the cells actually transfer the biomechanical signals in without the deformation of extracellular matrix and points to direct crosstalk between integrins and BMP receptors, similar to the recently identified physical interaction of integrins with growth factor receptosr[30]. By the application of both immunoprecipitation and recently developed FRET methods, we discovered the physical interaction between Iβ1 and type 1 BMP receptors in rat MSCs. Moreover, on substrates with rigidity equal to or exceeding that of trabecular bone, both expression of Iβ1 as well as its co-localization with type 1 BMP receptor increased, resulting in up-regulation of BMP signaling through Smad 1/5 and p44/42 MAPK and consequently increased expression level of osteogenic genes.

To better understand each role of the two membrane receptors in substrate rigidity-mediated osteogenesis, we isolated the effects of Iβ1 and type 1 BMP receptor. Since the expression of Iβ1 was regulated correspondingly with the osteogenesis related genes on the PUR films, siITGb1 was added to MSCs cultured on tissue culture plate (with similar rigidity to that of the rigid PUR films)

to inhibit the expression of Iβ1. Concequently, as described above in Fig. 6.4B, the expression level of *Runx2* was significantly decreased. On the contrary, when stimulating the expression of Iβ1 by plasmid transfection, the *Runx2* level in Iβ1 over expressing MSCs significantly increased correspondingly. The expression of Iβ1 by MSCs enhanced their osteogenic differentiation, which is consistent with previously reported studies[31]. We also selected a type 1 BMP receptor kinase inhibitor to determine the involvement of the soluble ligand receptor during osteogenesis. Previous studies have reported that dorsomorphin selectively inhibits the BMP type I receptors ALK2, ALK3 and ALK6 and blocks BMP-mediated SMAD1/5 phosphorylation[32]. As no soluble ligand stimuli were fed to MSCs during the differentiation process, the decreased expression of osteoblastic genes caused by dorsomorphin treatment clearly indicated the direct involvement of type 1 BMP receptor in substrate mediated osteogenesis. Combining these results, the substrate rigidity dose responsive physical interaction between Iβ1 and type 1 BMP receptor was confirmed in this study.

Since the signaling crosstalk points to the involvement of BMP signaling pathway, to test the potential application of PUR scaffolds for bone repair we determined whether increased substrate rigidity can enhance BMP signaling in adherent cells and reduce the required dose of rhBMP2. Rat MSCs were plated on rigid and compliant PUR films and treated with rhBMP2 of different doses. With the increase of rhBMP2 dose, expression of Runx2 was increased on both groups, while the expression by MSCs on rigid films remained higher than on compliant films. Therefore, by increasing the substrate modulus of rhBMP2 delivery systems, it is possible to reduce the dose of locally delivered rhBMP2, which could potentially reduce the frequency of complications associated with rhBMP2.

Acknowledgement

Research reported in this publication was supported by the National Institute of Arthritis and Musculoskeletal and Skin Diseases (part of the National Institutes of Health, under Award Number 5R01AR056138-02), the National Science Foundation under Award Number DMR-0847711, and the Department of Veterans Affairs under Award Number 1I01BX001957. The content is solely the responsibility of the authors and does not necessarily represent the official views of the National Institutes of Health, the National Science Foundation, or the Department of Veterans Affairs.

Reference

[1] Rosset P, Deschaseaux F, Layrolle P, Cell therapy for bone repair, Orthop Traumatol Surg Res. 2014 Feb;100(1 Suppl):S107-12.
[2] Ahlmann, E., Patzakis, M., Roidis, N., Shepherd, L., Holtom, P. (2002). Comparison of anterior and posterior iliac crest bone grafts in terms of harvest-site morbidity and functional outcomes. The Journal of Bone & Joint Surgery, 84(5), 716-720.
[3] Giannoudis, P. V., Dinopoulos, H., & Tsiridis, E. (2005). Bone substitutes: an update. Injury, 36(3), S20-S27.
[4] Vo, T. N., Kasper, F. K., Mikos, A. G. (2012). Strategies for controlled delivery of growth factors and cells for bone regeneration. *Advanced drug delivery reviews*, *64*(12), 1292-1309.
[5] Undale, A. H., Westendorf, J. J., Yaszemski, M. J., Khosla, S. (2009, October). Mesenchymal stem cells for bone repair and metabolic bone diseases. In Mayo Clinic Proceedings (Vol. 84, No. 10, pp. 893-902). Elsevier.
[6] Wang, X. X., Allen Jr, R. J., Tutela, J. P., Sailon, A., Allori, A. C., Davidson, E. H., Paek G. K., Saadeh P. B., McCarthy J. G., Warren, S. M. (2011). Progenitor cell mobilization enhances bone healing by means of improved neovascularization and osteogenesis. Plastic and reconstructive surgery, 128(2), 395-405.

[8] Blackwood, K. A., Bock, N., Dargaville, T. R., Ann Woodruff, M. (2012). Scaffolds for growth factor delivery as applied to bone tissue engineering.*International Journal of Polymer Science*, *2012*.
[9] Rosen, V. (2009). BMP2 signaling in bone development and repair. *Cytokine & growth factor reviews*, *20*(5), 475-480.
[10] Valentin-Opran, A., Wozney, J., Csimma, C., Lilly, L., Riedel, G. E. (2002). Clinical evaluation of recombinant human bone morphogenetic protein-2. *Clinical orthopaedics and related research*, *395*, 110-120.
[11] Tannoury, C. A., An, H. S. (2014). Complications with the use of bone morphogenetic protein 2 (BMP-2) in spine surgery. *The Spine Journal*, *14*(3), 552-559.
[12] Boraiah, S., Paul, O., Hawkes, D., Wickham, M., Lorich, D. G. (2009). Complications of recombinant human BMP-2 for treating complex tibial plateau fractures: a preliminary report. Clinical Orthopaedics and Related Research®, 467(12), 3257-3262.
[13] Shih, Y. R. V., Tseng, K. F., Lai, H. Y., Lin, C. H., Lee, O. K. (2011). Matrix stiffness regulation of integrin‐mediated mechanotransduction during osteogenic differentiation of human mesenchymal stem cells. Journal of Bone and Mineral Research, 26(4), 730-738.
[14] Smith, K. E., Hyzy, S. L., Sunwoo, M., Gall, K. A., Schwartz, Z., Boyan, B. D. (2010). The dependence of MG63 osteoblast responses to (meth) acrylate-based networks on chemical structure and stiffness. Biomaterials, 31(24), 6131-6141.
[15] Moore, S. W., Roca-Cusachs, P., Sheetz, M. P. (2010). Stretchy proteins on stretchy substrates: the important elements of integrin-mediated rigidity sensing. Developmental cell, 19(2), 194-206.
[16] Guelcher SA, Patel V, Gallagher KM, Connolly S, Didier JE, Doctor JS, Hollinger JO. Synthesis and in vitro biocompatibility of injectable polyurethane foam scaffolds. Tissue Engineering. 2006;12(5):1247-59,[PCMID:2]
[17] CB Khatiwal, SR Peyton, M Metzke, AJ Putnam, The regulation of osteogenesis by ECM rigidity in MC3T3-E1 cells requires MAPK activation. J Cell Physiol. 2007; 211: 661–672

[18] C Huang, R Ogawa, Mechanotransduction in bone repair and regeneration, FASEB J, 2010; 24-10: 3625-32.
[19] Shih YR, Tseng KF, Lai HY, Lin CH, Lee OK, Matrix stiffness regulation of integrin-mediated mechanotransduction during osteogenic differentiation of human mesenchymal stem cells, J Bone Miner Res. 2011 Apr;26(4):730-8.
[20] Jaiswal RK, Jaiswal N, Bruder SP, Mbalaviele G, Marshak DR, Pittenger MF, Adult human mesenchymal stem cell differentiation to the osteogenic or adipogenic lineage is regulated by mitogen-activated protein kinase, J Biol Chem. 2000 Mar 31;275(13):9645-52.
[21] Wang YK, Yu X, Cohen DM, Wozniak MA, Yang MT, Gao L, Eyckmans J, Chen CS, Bone morphogenetic protein-2-induced signaling and osteogenesis is regulated by cell shape, RhoA/ROCK, and cytoskeletal tension, Stem Cells Dev. 2012 May 1;21(7):1176-86.
[22] Song B, Estrada KD, Lyons KM, Smad signaling in skeletal development and regeneration, Cytokine Growth Factor Rev. 2009 Oct-Dec;20(5-6):379-88.
[23] Rath B, Nam J, Deschner J, Schaumburger J, Tingart M, Grässel S, Grifka J, Agarwal S, Biomechanical forces exert anabolic effects on osteoblasts by activation of SMAD 1/5/8 through type 1 BMP receptor, Biorheology. 2011;48(1):37-48. doi: 10.3233/BIR-2011-0580.
[24] TC He, et, al., BMP signaling in mesenchymal stem cell differentiation and bone formation, J. Biomedical Science and Engineering, 2013, 6, 32-52.
[25] Katsumi, A., Orr, A. W., Tzima, E., Schwartz, M. A. (2004). Integrins in mechanotransduction. Journal of Biological Chemistry, 279(13), 12001-12004.
[26] Khatiwala, C. B., Kim, P. D., Peyton, S. R., Putnam, A. J. (2009). ECM compliance regulates osteogenesis by influencing MAPK signaling downstream of RhoA and ROCK. Journal of Bone and Mineral Research, 24(5), 886-898.
[27] DS Harburger and DA Calderwood, Integrin signalling at a glance. Journal of Cell Science 122, 1472 (2009)
[28] Eliceiri BP, Integrin and growth factor receptor crosstalk, Circ Res. 2001 Dec 7;89(12):1104-10.
[29] Salasznyk, R. M., Klees, R. F., Williams, W. A., Boskey, A., Plopper, G. E. (2007). Focal adhesion kinase signaling pathways regulate the osteogenic differentiation of human mesenchymal stem cells. Experimental cell research, 313(1), 22-37.
[30] Eliceiri, B. P. (2001). Integrin and growth factor receptor crosstalk. Circulation research, 89(12), 1104-1110.
[31] Hamidouche, Z., Fromigué, O., Ringe, J., Häupl, T., Vaudin, P., Pagès, J. C., Srouji, S., Livne, E., Marie, P., J., Marie, P. J. (2009). Priming integrin α5 promotes human mesenchymal stromal cell osteoblast differentiation and osteogenesis. Proceedings of the National Academy of Sciences, 106(44), 18587-18591.
[32] Paul B Y, Hong C C, Sachidanandan C, et al. Dorsomorphin inhibits BMP signals required for embryogenesis and iron metabolism [J]. Nature chemical biology, 2007, 4(1): 33-41.

CHAPTER 7

CONCLUSIONS AND FUTURE WORK

Summary of the dissertation

The research presented in this dissertation describes the design and development of polyurethane scaffolds with controllable physical properties as potential cell carriers for tissue regeneration. The results demonstrated here show that the regenerative mesenchymal stem cells are able to be viably incorporated in the reactive, injectable and settable polyurethane scaffolds and prompted excisional wounds healing. Moreover, cell fate of the incorporated MSCs are shown to be controlled by physical properties of the designed scaffolds and the subcutaneous wound healing results indicated the requirement and benefit of optimization of scaffolds mechanical properties for wound regeneration. Additionally, to better understand the effects of scaffolds physical properties for tissue regeneration and cell fate control, the studies conducted in the previous chapters also determined and partially clarified cell-polyurethane interaction mechanisms.

The first two chapters demonstrated the background that the studies are designed on and the detailed division and approach of the designed studies towards the final objective of this dissertation.

In Chapter 3, the injectable and settable polyurethane scaffolds, which are synthesized with reactive hydrophobic components and polymerize *in situ*, incorporating live MSCs are first designed for cell therapy and applied to an animal excisional wound model. MSCs were encapsulated in partially oxidized alginate hydrogel with fast degrading property *in vivo* before the polyurethane synthesis reaction to better conserve cell survivability. The incorporation of MSC

encapsulated beads was optimized by delaying the addition of o-Alg beads to reduce the generation of CO_2 by the water reaction, as well as reaction generated heat. By measuring MSCs viability and calculating generated CO_2 and heat[1], the correlation of cell death and hazardous products was set up and was able to direct further synthetic cell carrier design. In the optimized design, o-Alg beads subsequently degraded to form interconnected macro pores that support cellular migration, proliferation, and deposition of new matrix *in vitro* and *in vivo*. These advantages underscore the potential utility of polyurethane scaffolds as a versatile, clinically-translatable, and functionally-significant injectable cell delivery system for regenerative medicine application.

Then, in order to understand the effects of polyurethane physical properties on cell fate, we designed polyurethane scaffolds of properties under full control by applying the advanced 3D printing technique and this study is described in Chapter 4. Bone marrow derived mesenchymal stem cells (BMSCs) consist of a heterogeneous stem cell population that are able to differentiate to a wide range of cell types including osteoblasts and thus are considered to be good candidates as regenerative medicine for bone repair[2],[3],[4]. As the micro environment to support delivered cells, instead of biochemical signals, the 3D scaffolds are required to provide proper interactive mechanical and topographical cues to control cell fate[5]. By applying 3DP technique to generate scaffold templates, we formed PUR scaffolds, which is difficult to be directly printed due to the technical limitation of 3DP nowadays, of precisely controlled and uniformly distributed porosity in this study. We therefore synthesized PUR scaffolds of varied rigidities and pore diameters and studies BMSCs osteogenesis in response to scaffold properties. BMSCs were conducting osteoblastic faster on the rigid scaffolds under the same induction conditions than on the compliant.

Yet, although smaller pore size partially contributed to osteoblast mineralization which indicated its role in the mature process of osteoblast, it is the scaffold mechanical strength that dominating osteoblastic differentiation process.

Considering the general influence of scaffold physical properties on cellular behavior, we then evaluated their effects on skin wound healing process with the developed controllable PUR scaffolds. We applied PUR scaffolds of identical inner structures with varied rigidities to rat subcutaneous wound model to study the effects of mechanical strength on wound healing process. Surprisingly, with the applied scaffolds, we found that, instead of dose response to rigidities, the infiltration, collagen deposition, as well as angiogenesis were maximized in the middle rigid scaffolds. At the same time, Wnt/β-catenin signaling of fibroblasts, and macrophages in response to the implants, the maximization of wound healing in the middle rigid scaffolds were the balanced results of inhibited Wnt/β-catenin signaling and impressed inflammatory. Therefore, since there are multiple factors affecting cutaneous wound healing process through mechanotransduction pathways, for the clinical application, it is essential to find out the optimized mechanical properties of implanted scaffolds in different wound models.

As the former part of the study points out the importance of substrate rigidities on cell behavior, the same PUR materials were casted into 2D films to better understand its potential mechanism, especially for osteoblastic differentiation.

Suggestions for future work

Overall, the design and development of polyurethane scaffolds with controllable physical and

topographical properties as potential cell delivery carrier to facilitate tissue regeneration have been presented in this work. In order to transnationally apply the developed scaffolds in clinics, modifications of the scaffolds formulation and thoroughly understanding of cells and host tissues response are required to be further determined. Therefore, I would like to propose the following suggestions for future works to fill up the gap between the development of this polyurethane scaffold and its clinical translation.

Promoting porcine full-thickness excisional wound healing

Skin regeneration, especially in large or chronic wounds, is an important aspect of tissue regeneration to prevent scarring and promote healing. Nowadays, smaller mammalian animals are utilized a lot in wound healing studies. Yet considering anatomical and physiological properties of their skins, they differ from humans in multiple ways and thus is difficult to predict the real physiological response of human tissues from these models. Therefore, pig skin wound models have been developed to be a more representative model for translational wound healing study because of the similarities between human and pig skins (Fig. 7.1)[6],[7].

Chapter 3 presents the promoted wound healing results with the developed polyurethane cell carrier in rat excisional wound model, indicating its translational potentials as cell therapy in clinical application. In order to further determine its clinical potentials, it is necessary to test human-like tissue response and thus future studies would start with the application of this cell carrier in pig skin wound models. A preliminary study in pig excisional wound model was

conducted and going on for two weeks. Trichrome green histological staining was performed on the harvested tissue sections and the MSCs groups showed significantly increased collagen deposition which is consistent with the results of collagen gene expression from harvested wound tissues, indicating faster wound closure with the aid of polyurethane carrier (Fig. 7.2)

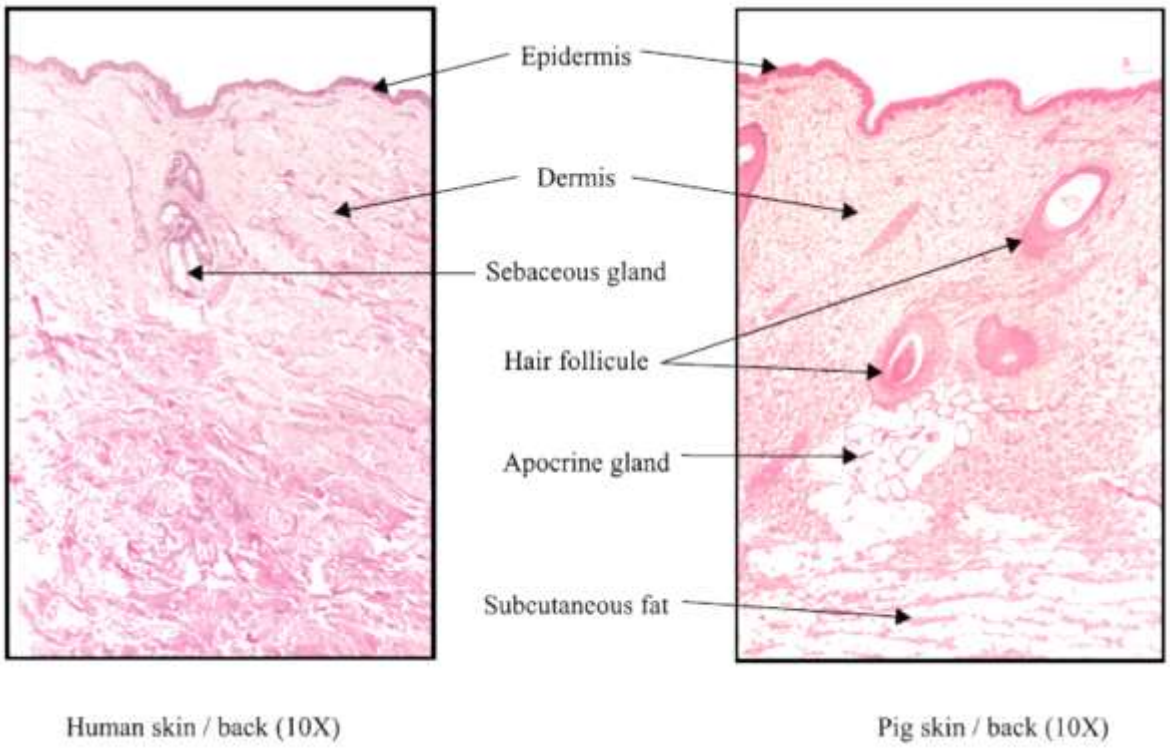

Figure 0.1 Comparison of histological features from pig and human skins (H&E staining) [6]

At the same time, another complicated problem generated by uncured wounds is lacking defense to infections, driving the needs to promote epithelialization for any applied therapy[8]. In the proof-of-concept rat or pig excisional wound healing experiment presented in this study, only early time response, including cellular infiltration, growth factor expression, and collagen deposition, has been evaluated. Considering the important re-epithelialization, I propose a longer (>30 days) skin wound healing study with the optimized polyurethane cell carrier to fully study

its effects on wound re-modeling, re-epithelialization, as well as early response to guide future modification of the developed cell carrier for clinical studies. Moreover, combining the results presented in Chapter 3 and Chapter 5, physical properties of this polyurethane cell carrier can also be manipulated to control cell fate of both delivered MSCs and contacted host tissues to further promote skin wound regeneration.

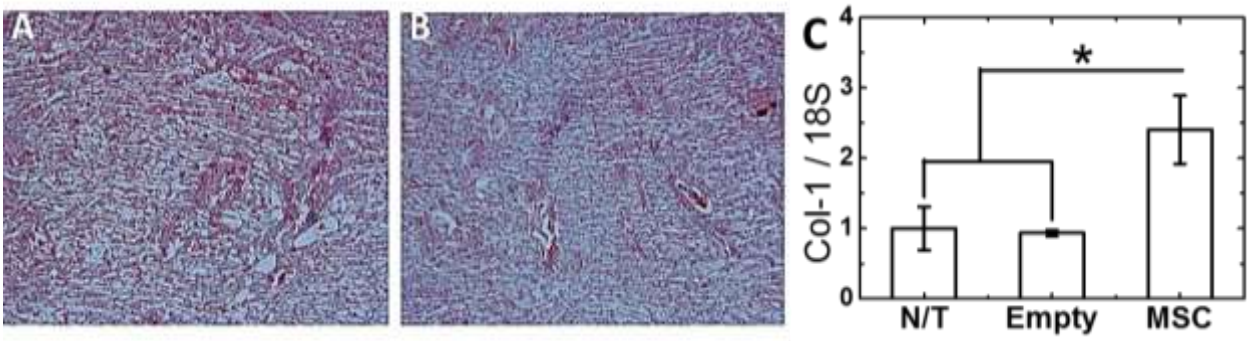

Figure 0.2 Collagen measurement of harvested wound tissues at D14

Trichrome green histological staining of harvested wounds after applying the injectable scaffolds without (A) or with MSCs (B) for 2 weeks, (C), Collagen 1 gene expression fold change of harvested wounds after 2 weeks of application of MSCs incorporated polyurethane scaffolds.

Mechanism of polyurethane scaffolds benefit and application for bone regeneration

Argument of regenerative cells functions in cell therapy has been going on for decades and still not thoroughly understood up to date. Therefore, it is necessary to illustrate the potential mechanism of how the developed polyurethane cell carrier improved wound healing. A cell dose response study of delivered MSCs has been conducted in rat excisional wound model as the follow up of the proof-of-concept *in vivo* application. Increased trend of cellular response has been obtained, including cellular infiltration, infiltrated cells proliferation, as well as early angiogenesis (Fig. 7.3 A-C). Moreover, gene expression level of essential growth factors for

wound healing process has also been evaluated in this preliminary animal experiment and the dosage response of these growth factors expression, especially the expression of Platelet-derived growth factor (PDGF) (Fig. 7.3 D), further indicated the crucial functionalities of delivered regenerative cells. At the same time, preliminary results from the short term pig study demonstrated the existence of delivered MSCs for up to two weeks (Fig. 7.4), which conflicts several previous understandings. Thus, longer term study with proper tracking of delivered cells will be necessary and critical to better clarify their functions *in vivo*.

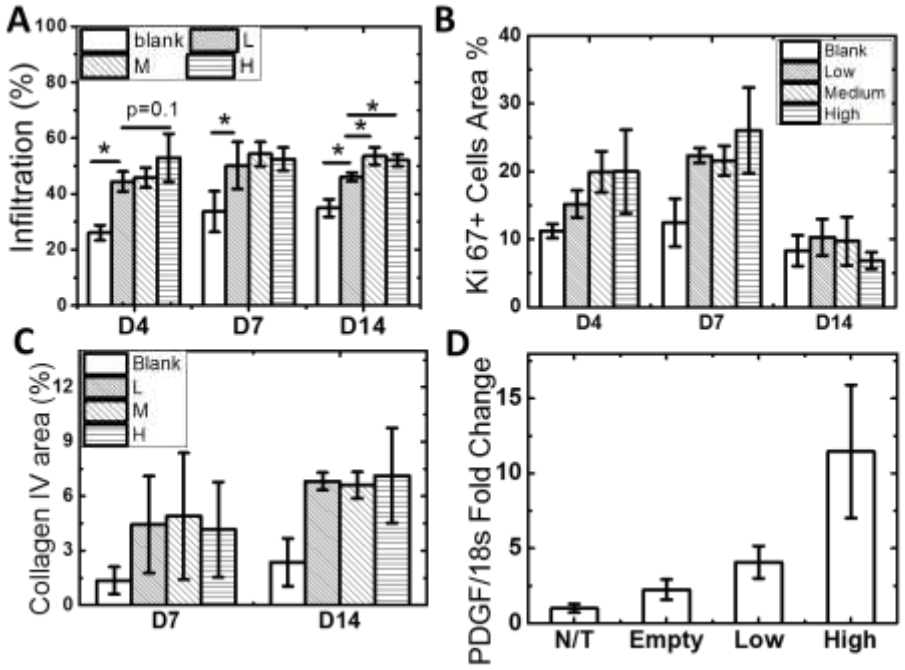

Figure 0.3 Cellular dose response to the delivered mesenchymal stem cells.

(A) Cellular infiltration of cells into scaffolds measured by histomorphometry. (B) Population of Ki67+ cells measured by immunohistochemical staining. (C) Wound vascularization assessed by Collagen IV immunohistochemical staining. (D) Expression of PDGF (measured by qPCR) increased with the increasing delivered cell number at D14.

On the other side, since the mechanical properties of polyurethane scaffolds are easily manipulated, thus other than tuning the rigidity for better skin wound regeneration as illustrated in Chapter 5, the developed cell carriers presented in this study are able to be formulated for the application of bone regeneration. As demonstrated in Chapter 4, mechanical properties of implanted polyurethane scaffolds are important for osteoblastic differentiation and the more rigid scaffolds are able to benefit osteogenesis and mineralization, as well as to provide weight bearing properties. Therefore, for the application of the developed injectable polyurethane scaffolds in bone regeneration to take the advantage of variable shapes and settable properties of the scafolds, polyurethane formulation needs to be modified with polyester triols of shorter chain and in order to overcome the associated faster degradation rate, functioning isocyanate molecules are subject to change accordingly and proper application of antioxidants would be necessary.

In the meanwhile, however, simply delivery of multipotent regenerative cells would not work properly for bone repair as lacking biological osteogenesis cues after injection *in vivo*. Thus, the development of a dual delivery system incorporating both MSCs and osteogenic induction molecules would be crucial for its successfully application in bone field. Considering the hydrophobic properties of several applicable osteogenic molecules, I propose the application of recently designed nanoparticle polymers in Guelcher's lab to incorporate the molecules and thus modify the polyurethane scaffolds into a dual delivery system. Preliminary experiment showed stable release of incorporated lovastatin from polyurethane scaffolds cultured *in vitro* (Fig. 7.5A) and its osteogeneic induction effects were proved by rat BMSCs long term culture *in viro* (Fig. 7.5B).

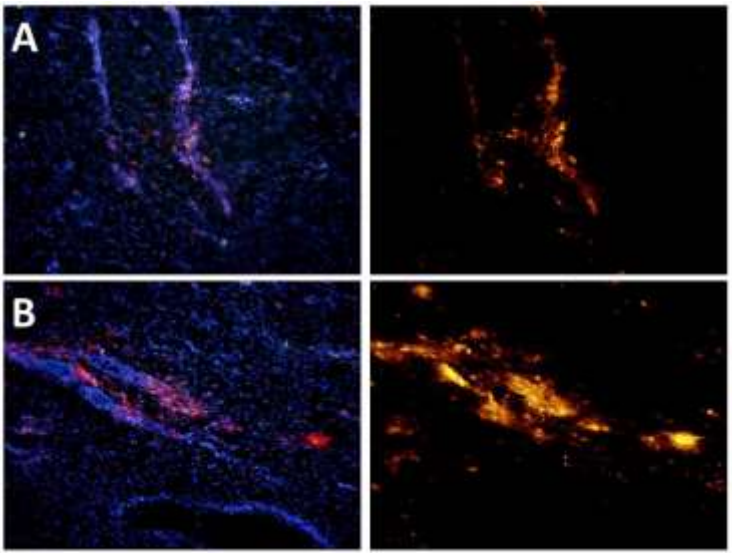

Figure 0.4 Fluorescence images of delivered porcine MSCs (Red) surrounded by filtrated host tissues (Blue) from harvested wounds after 2 weeks.

Real bone structure derived scaffolds and co-culture with osteoclasts

In this presented study, we have designed the bone-like polyurethane scaffolds by applying the 3D printing technique with the PLA templates of rod structures. Although both the inner structure and physical properties can be precisely controlled and the scale of designed fiber diameters are reported to enhance bone formation and vascularization[9], the uniform distribution of pores and fibers inside the scaffolds makes it discrepancy from the real bone structure. Natural bone has higher porosity in the core with a strong and dense outer shell[10], indicating the requirement of scaffolds design consisting of gradient distribution of pore structure. Moreover, comparing the real bone micro-CT images and SEM images of the rod scaffolds, it is obvious that natural bone has significantly higher bulk porosity (Fig. 7.6). Therefore, the next step for the translational application of the designed polyurethane scaffolds would be mimicking natural

bone by designing the 3D printing templates as the inverted natural bone structure derived from micro-CT scanning.

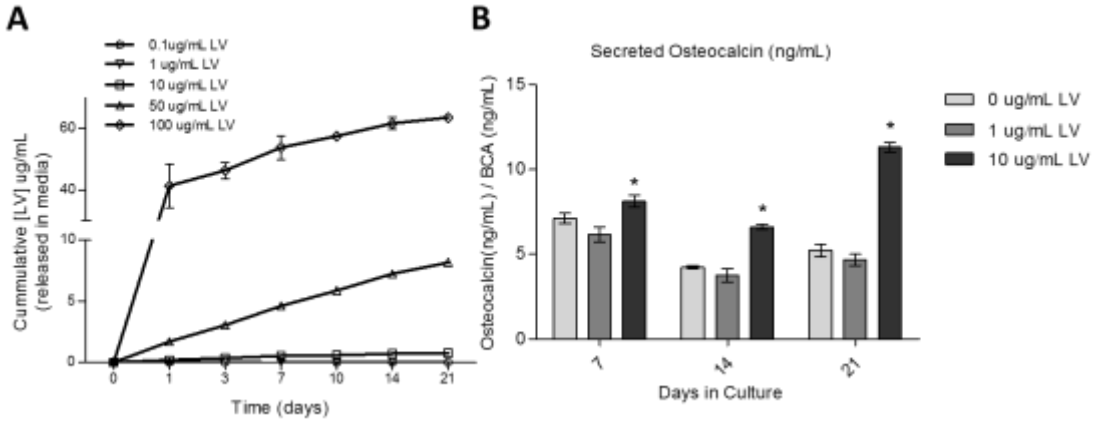

Figure 0.5 In vitro delivery of nanoparticle encapsulated lovastatin.

(A) Lovastatin *in vitro* release from scaffolds quantified by HPLC. (B) In vitro osteogenic differentiation of rat BMSCs in the presence of LV. The concentration with the most osteogenic activity (10 μg/mL) would be selected for *in vivo* studies due to its non-toxicity and osteogenic induction.

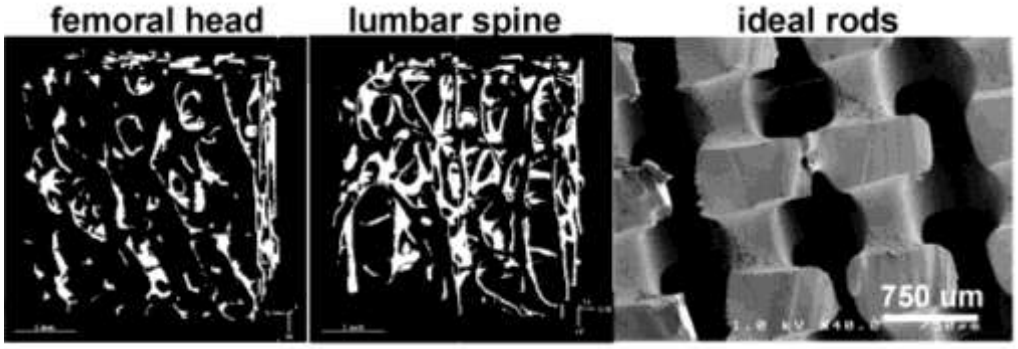

Figure 0.6 Structural comparison between natural bone tissue and the designed biomimetic tissue engineered 3D-PUR scaffolds.

Compared to natural bone tissues, the developed 3D rod scaffolds provided comparable pore sizes but polymer materials occupied more space.

At the same time, since tissue repair is a highly dynamic process, not only the promoted growth of osteoblasts but also the removal of bone debris/remaining scaffolds by osteoclasts are important for bone tissue modification in order to maintain and improve the structural strength of bone tissue[11]. Chapter 4 presented MSC osteoblastic differentiation control with the application of the developed t-FDM polyurethane scaffolds. Therefore, for better bone tissue regeneration, it would be essential to study the effects of scaffolds physical properties on both osteoblasts and osteoclasts differentiation and activity to achieve the balance of bone formation/resorption[12].

Macrophage polarization in response to substrate rigidities

After the existence of wounds, monocytes are the first cell population recruited to the wound bed and they promoted wound healing by differentiating into macrophages. The existence and function of macrophage are essential in all stages of wound healing, while their functional phenotype is dependent on the wound bed microenvironment and is thus altered correspondingly during healing[13].

In Chapter 5, macrophage markers from the wound beds treated with different rigid scaffolds showed significant difference between groups, leading to the suspect of substrate rigidity mediated macrophage polarization. It has been widely understood that membrane receptor ligation being the central mechanism that regulates macrophage function in wound healing process. Yet recent studies have unveiled that macrophage function is also regulated by the elasticity of cells. A previous study has reported that macrophage elasticity is modulated by substrate rigidity and substrate stretch that is dependent upon actin polymerization and small

rhoGTPase activation[14]. Therefore, it is necessary to study the macrophage polarization and activation on the developed polyurethane materials with varied rigidities to evaluate its contribution in the manipulated wound regeneration process and further to clarify the molecular mechanism of substrate rigidity effects on macrophage phenotype differentiation.

Reference

[1] Page, J. M., Prieto, E. M., Dumas, J. E., Zienkiewicz, K. J., Wenke, J. C., Brown-Baer, P., Guelcher, S. A. (2012). Biocompatibility and chemical reaction kinetics of injectable, settable polyurethane/allograft bone biocomposites. Acta biomaterialia, 8(12), 4405-4416.
[2] Sponer P1, Kučera T, Diaz-Garcia D, Filip S, The role of mesenchymal stem cells in bone repair and regeneration, Eur J Orthop Surg Traumatol. 2014 Apr;24(3):257-62.
[3] Bianco P, Robey PG, Stem cells in tissue engineering, Nature. 2001 Nov 1;414(6859):118-21.
[4] Bruder SP, Fink DJ, Caplan AI, Mesenchymal stem cells in bone development, bone repair, and skeletal regeneration therapy, J Cell Biochem. 1994 Nov;56(3):283-94.
[5] Han LH, Tong X, Yang F, Photo-crosslinkable PEG-based microribbons for forming 3D macroporous scaffolds with decoupled niche properties, Adv Mater. 2014 Mar 19;26(11):1757-62.
[6] Sullivan, T. P., Eaglstein, W. H., Davis, S. C., Mertz, P. (2001). The pig as a model for human wound healing. Wound repair and regeneration, 9(2), 66-76.
[7] Terris, J. M. (1986). Swine as a model in renal physiology and nephrology: an overview. In Swine in biomedical research, Vol. 3.
[8] Wang, J. F., Olson, M. E., Reno, C. R., Wright, J. B., Hart, D. A. (2001). The pig as a model for excisional skin wound healing: characterization of the molecular and cellular biology, and bacteriology of the healing process. Comparative medicine, 51(4), 341-348.
[9] F. Rossi, M. Santoro, G. Perale, J Tissue Eng Regen Med 2013, DOI: 10.1002/term.1827; L. A. Cyster, D. M. Grant, S. M. Howdle, F. R. Rose, D. J. Irvine, D. Freeman, C. A. Scotchford, K. M. Shakesheff, Biomaterials 2005, 26, 697; A. Penk, Y. Forster, H. A. Scheidt, A. Nimptsch, M. C. Hacker, M. Schulz-Siegmund, P. Ahnert, J. Schiller, S. Rammelt, D. Huster, Magnetic resonance in medicine : official journal of the Society of Magnetic Resonance in Medicine / Society of Magnetic Resonance in Medicine 2013, 70, 925.
[10] Bose S, Roy M, Bandyopadhyay A. Recent advances in bone tissue engineering scaffolds[J]. Trends in biotechnology, 2012, 30(10): 546-554.
[11] Schell, H., Lienau, J., Epari, D. R., Seebeck, P., Exner, C., Muchow, S., Bragulla H., Haas N. P., Duda, G. N. (2006). Osteoclastic activity begins early and increases over the course of bone healing. Bone, 38(4), 547-554.
[12] Bab, I. A., Sela, J. J. (2012). Cellular and molecular aspects of bone repair. In Principles of Bone Regeneration (pp. 11-41). Springer US.
[13] Delavary, B. M., van der Veer, W. M., van Egmond, M., Niessen, F. B., Beelen, R. H. (2011). Macrophages in skin injury and repair. Immunobiology, 216(7), 753-762.
[14] Patel, N. R., Bole, M., Chen, C., Hardin, C. C., Kho, A. T., Mih, J., Deng, L., Butler, J., Tschumperlin, D., Fredberg, J.J., Krishnan, R., Koziel, H. (2012). Cell elasticity determines macrophage function. PloS one, 7(9), e41024.

APPENDIX

Experimental Protocols

Guelcher Lab

Formation of alginate beads with electronic bead maker

Principle:

Formation of alginate beads: To encapsulate cells/other particles desired for delivering.

Before starting:

- Read and understand the MSDS of the reagents listed below
- Personal Protective and Safety Equipment required:
  - Disposable nitrile gloves
  - Lab coat

Reagents:

- *Distilled water*
- *Sodium alginate acid (Aldrich Chemistry, viscosity = 20-40 cps)*
- *Calcium chloride (Acros Organics)*
- *Ethanol*

Materials and Equipment:

- *Electronic bead maker (Nisco, VAR V1)*
- *Syringe (10mL)*
- *Beaker*
- *Magnetic stirring bar*
- *Syringe pump*

Procedure:

1. *Dissolve sodium alginate acid in distilled water (usually 1-2w/v% for cell encapsulation) and then suspend cells/other particles in alginate acid solution*
2. *Dissolve calcium chloride in distilled water (usually 100-200mM for cell encapsulation)*
3. *Add alginate acid solution in syringe and inject into the bead maker with syringe pump (rate = 10mL/h); Add calcium chloride solution in collection beaker and stir with magnetic stirring bar*
4. *Adjust applied voltage to control bead size (higher voltage = smaller bead diameter)*
5. *Collect alginate beads from calcium chloride solution*
6. *Clean all the equipment with distilled water first and then clean with ethanol to sterilize*

Notes:

1. *If the tubes or nozzles are blocked during formation process, change the syringe of distilled water and pump water through tubes/nozzles with pressure*
2. *When cleaning up, must first clean with water and then with ethanol. Sodium alginate acid will gel with ethanol.*

Clean-up:

1. Collect all glass waste (pipettes, vials, or broken glass) and dispose in the broken glass container (box)
2. Collect all liquid waste and dispose in the appropriate liquid waste container (acetone or halogenated)
3. Clean all the equipment with distilled water first and then clean with ethanol to sterilize
4. Clean glassware:
    a. Wash with soap and water
    b. If it is necessary, rinse with acetone and introduce into the base bath for 24 hrs. Rinse with a lot of cold running water after removing from the base bath.
    c. Rinse with acetone and dry in the oven

Guelcher Lab

Partially Oxidation of Sodium Alginic Acids

Principle:

Partially oxidation of sodium alginic acid: To accelerate degradation of alginate hydrogel.

Reagents:

- *Distilled water*
- *Sodium alginate acid (Aldrich Chemistry, viscosity = 20-40 cps)*
- *Sodium periodate (Acros Organics)*
- *Ethanol*

Materials and Equipment:

- *Beaker*
- *Magnetic stirring bar*
- *Vacuum oven with pump*

Procedure:

1. *Dissolve sodium alginate acid in distilled water to make 1 wt% sodium alginate solution (Dissolve 0.8 g sodium alginate in 80 mL Di-water)*
2. *Dissolve sodium periodate in distilled water to make 0.25 M solution*
3. *Add 645 μL sodium periodate solution (0.25 M) and react in dark bottle with stirring for 24 hrs and then add 1-2 drops of ethylene glycol to end the reaction*
4. *Add 2 g dodium chloride (6.25 g/L) and stir to dissolve*
5. *Add 160 mL ethyl alcohol to precipitate and collect the precipitates with centrifuge*
6. *Redissolve the precipitates in 80 mL Di-water and add 160 mL ethyl alcohol to precipitate again*
7. *Collect the precipitates and dry under vacuum*

Notes:

1. *Drying process could also be done in hood at room temperature*
2. *To further purify the oxidized alginate, redissolve the dried films, filter with filter paper and then lyophilize overnight.*

Guelcher Lab

Cell membrane fluorescence staining

Principle:

Fluorescence staining of mammalian cell membrane: for cell tracking in 3D culture/in vivo.

Reagents:

- *PBS*
- *Vybrant® DiI Cell-Labeling Solution (**Catalog Number V-22885**)*
- *Complete cell culture medium*
- *Serum free cell culture medium*

Materials and Equipment:

- *Centrifuge*
- *15 mL sterile centrifuge tube*

Procedure:

1. *Suspend cells at a density of 1 ×10^6/mL in any chosen serum-free culture medium*
2. *Add 5 μL of the cell labeling solution supplied per mL of cell suspension. Mix well by gentle pipetting.*
3. *Incubate for 15 min at 37 ℃.*
4. *Centrifuge the labeled suspension tubes at 1500 rpm for 5 min, preferably at 37 ℃.*
5. *Remove the supernatant and gently resuspend the cells in warm (37 C) medium.*
6. *Repeat the wash procedure (4 & 5) two more times.*
7. *Allow 10 min recovery time before proceeding with fluorescence measurements. (Or seeding cells in tissue culture flasks).*

Notes:

1. *Incubation time needs to be optimized for different cells to form uniform fluorescence staining*
2. *Membrane staining will be diluted with cell proliferation*

Guelcher Lab

Actin fluorescence staining

Principle:

Fluorescence staining of mammalian cell actin structure

Reagents:

- *PBS*
- *Methanol*
- *rhodamine phalloidin (Invitrogen R415)*
- *Methanol-free formaldehyde*
- *Triton X-100*
- *Bovine Serum Albumin (BSA)*

Procedure:

1. *Wash cells twice with prewarmed phosphate-buffered saline, pH 7.4 (PBS).*
2. *Fix the sample in 3.7% formaldehyde solution in PBS for 10 minutes at room temperature.*
3. *Wash two or more times with PBS..*
4. *Cover fixed cells with 0.1% Triton X-100 in PBS for 3 to 5 minutes.*
5. *Wash two or more times with PBS.*
6. *Pre-incubate fixed cells with PBS containing 1% BSA for 30 min.*
7. *Dilute 5 µL methanolic stock solution into 200 µL PBS containing 1% BSA to cover fixed cells and stain for 20 min.*
8. *Wash two or more times with PBS and check with fluorescence microscopy.*

Notes:

1. *The vial contents should be dissolved in 1.5 mL methanol to yield a final concentration of 200 units/mL, which is equivalent to approximately 6.6 µM.*
2. *Staining solution volume can be adjusted for different tissue culture plates*
3. *For long-term storage, the cells should be air dried and then mounted in a permanent mountant such as ProLong® Gold reagent or Cytoseal. Specimens prepared in this manner retain actin staining for at least six months when stored in the dark at 2–6 ℃.*

Principle:

Encapsulate ROS degradable nanoparticles in degradable oxidized alginate hydrogel beads for local hydrophobic drug delivery. The nanoparticles are synthesized from a poly(propylene) sulphide (PPS) and branched polyethylene glycol (PEG). The particles can be loaded with any hydrophobic compound. The particles are soluble in hydrophobic organic solvents and spontaneously form nanostructured micelles upon introduction to aqueous media.

Reagents:

- *PEG-PPS polymer*
- *Organic solvent, miscible with water (THF, MeOH, EtOH)*
- *Hydrophobic drug or compound (if loading nanoparticles)*
- *DI Water*
- *Oxidized sodium alginate*
- *Calcium chloride*

Materials and Equipment:

- *Balance*
- *Syringe pump*
- *Tubes*
- *Disposable syringes*
- *0.2 µm filters*
- *Kim wipes*

Procedure:

1. *Dissolve polymer and hydrophobic drug separately in **equal volumes** of the organic solvent (THF, MeOH, EtOH) (**polymer concentration = 10 mg/mL**) in small tube*

   ***Note**: Prepare drug solution concentration based on **polymer : drug** ratio*

   ***Example**: If Polymer : Drug ration = 100:1 (this is a good starting point), prepare drug concentration of 0.1mg/mL*

2. *Mix polymer and drug solutions together by pipetting*
3. *Slowly add oxidized sodium alginate solution into the polymer/drug mixture (final **water : organic solvent = ~50 : 1**)*

   Note: this step could be done with a syringe pump or manually pipette in small amounts

4. *Leave solution exposed to allow evaporation of the majority of the organic solvent*
5. *Re-suspend cells in the alginate solution with nanoparticles with mild stirring and perform alginate beads formation as usual.*

Note: In order to form a denser hydrogel crosslink to trap nanoparticles, increase the concentration of calcium chloride to 200 mM to 300 mM.

Notes:

- *If the polymer makes a cloudy solution upon adding the full amount of water try additional vortexing to dissolve the remaining polymer. If this still does not work increase the initial amount of organic solvent to 20 mg/mL*
- *The exact concentration of the hydrophobic drug loaded into the nanoparticles is difficult to ascertain directly. However you can assume nearly complete loading at small ratios of drug/polymer (>6 µg/mg). Additionally, if the organic solvent is fully evaporated any un-encapsulated drug should form particles that would be filtered out before use.*

Clean-up:

1. *Collect all glass waste (pipettes, vials, or broken glass) and dispose in the broken glass container (box)*
2. *Collect all sharps and dispose in the sharps waste container (red sharps box)*
3. *Collect all solid waste and dispose in the solid waste container*
4. *Collect all liquid waste and dispose in the appropriate liquid waste container (acetone or halogenated)*

Principle:

Separate and quantify expressed protein level by electrophoresis and blotting.

Reagents:

- *PBS*
- *RIPA buffer (Peirce)*
- *Protease and phosphatase inhibitor cocktail (Thermo 87786)*
- *EDTA (0.5 M, Thermo)*
- *BCA Protein Assay Kit (Pierce 23225)*
- *Millipore purified water*
- *10x Tris/Glycine/SDS (Biorad)*
- *10x Tris/Glycine (Biorad)*
- *Methanol*
- *Precision Plus Protein™ Dual Color Standards (Biorad)*
- *Sample buffer (2x, Biorad)*
- *β-ME ()*
- *LI-COR premade blocking buffer (in TBS)*
- *Stripping buffer (Thermo)*

Materials and Equipment:

- *PowerPac™ Basic Power Supply (Biorad)*
- *Mini-PROTEAN® Tetra Cell Systems (Biorad)*
- *0.2 um filter paper (Biorad)*
- *Mini-PROTEAN® TGX™ Gel, 10 well, 50 µl (Biorad)*
- *PVDF Membrane*

Procedure:

- *Protein harvest*
  1. *Prepare lysis buffer by adding 100x protease and phosphatase inhibitor to calculated volume of RIPA and keep all on ice.*
  2. *Aspirate culture medium and wash cells twice with cold PBS*

3. *Either detach cells from tissue culture plates by Trypsin/EDTA, pellet cells and add lysis buffer or directly add lysis buffer to cell layers (50 uL/one well in 6-well plate).*
4. *Transfer lysates into micro centrifuge tubes and repeat freeze-thaw cycle twice.*
5. *Spin at 13,200 rpm for 15 min at 4℃ and transfer supernatant to a new micro centrifuge tube and discard pelleted cell debris.*
6. *Measure protein concentration by BCA protein assay kit following the manual. Prepare reaction solution by mixing 50 parts BCA reagent A with 1 part BCA reagent B. Add 200 uL of the solution to each well and mix well by mildly shaking, cover with foil and incubate for 30 min at 37℃. Cool the plate to room temperature and read absorbance at 562 nm.*

- *Protein Electrophoresis:*

1. *Pick concentration for protein analysis (usually between 5 to 50 ug), calculate its volume and add to new micro centrifuge tubes.*
2. *Prepare 2x sample buffer by adding 50 uL β-ME into 950 uL sample buffer. Add equal volume of sample buffer to tubes containing calculated volume of protein sample.*
3. *Boil samples for 5-10 min at 95℃, cool down to RT and briefly spin down.*
4. *Prepare the pre-cast gel as described in manual and fill inside cartridge with running buffer. Pipet ~1.5x volume of running buffer into each well of the gel and pipet up and down to equilibrate loading wells.*
5. *Load 5 uL protein standard ladder and all the prepared protein samples to the gel.*
6. *Run for 15 minutes at 115V, then bump it up to 150V until sample buffer come to the edge of the gel.*
7. *Take the gel out of running buffer and soak in transfer buffer for 15 min.*

- *Protein Transfer:*

1. *Pre-soak PVDF membrane in methanol and then soak in transfer buffer. Soak filter paper and sponge pads in transfer buffer.*
2. *Make the sandwich with filter paper, membrane and gel as following:*

Clear-> pad-> filter paper-> membrane-> gel-> filter paper-> pad-> black

3. *Put the sandwich in transfer rig with transfer buffer, put the Tetra cell in small tank filled with ice and run for 60-90 min at constant currency 300 mA.*
4. *Remove membrane, soak in methanol, and then wash membrane for about 1 min in TBS buffer.*
5. *Block in 10 mL blocking buffer (dilute LI-COR blocking buffer 1:1 with TBS buffer) for 30-60 min with slightly shaking.*
6. *Cover the membrane with 5 mL blocking buffer and primary antibody at correct dilution (usually 1:500 for santa cruz (4 ℃) and 1: 1000 (-20 ℃) for cell signaling).*
7. *Put the blotting case on rotator in fridge at 4 ℃ overnight (usually > 16h).*

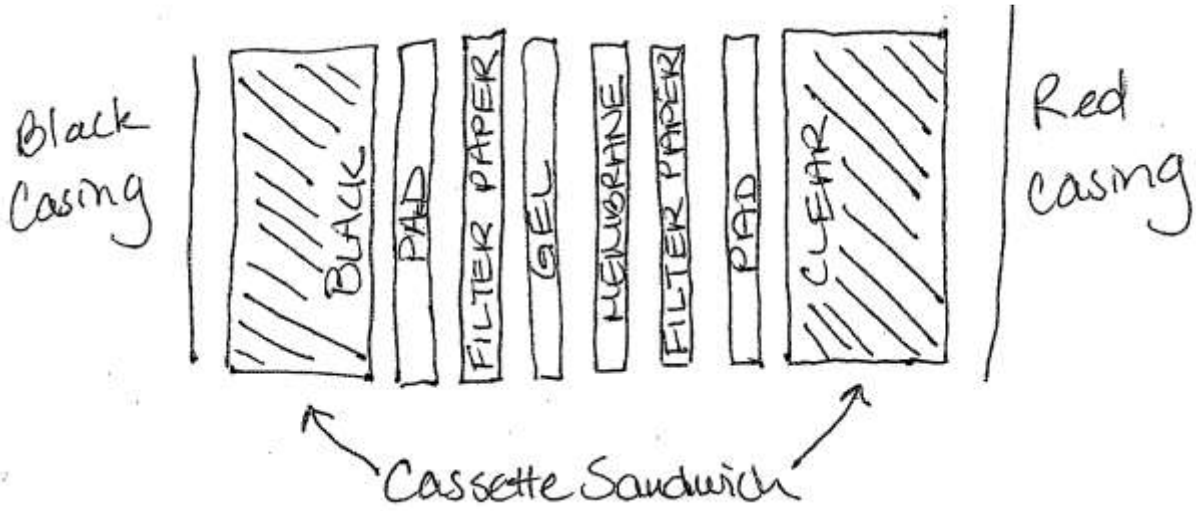

- *Western Blotting:*

1. *Remove membranes from primary solution and wash with TBST on shaker for 3 * 10 min.*
2. *Dilute secondary antibody in blocking buffer and incubate membrane for 1 h in 10 mL secondary antibody solution with slightly shaking at room temperature.*
3. *Wash membrane 5 * 5 min.*
4. *Mix 1:1 chemiluminescent reagents (2 mL/blot)*
5. *Drip dry the blot and put on food wrap with protein side facing up.*
6. *Dropwisely add chemiluminsescent mixture directly on membrane and incubate in dark for 1 min.*

7. *Drip dry the blot to get rid of excess chemiluminescent misture and move membrane to clean wrap and smooth out. Stick the membrane in cassette with protein side up.*
8. *Take to dark room and develop with film. Start with 30 s to 1 min exposing time.*

- *Stripping a blot:*

1. *Remove blot from wrap and wash for 5 min in TBST.*
2. *Add 10 mL stripping solution and incubate at RT for 30 min with shaking.*
3. *Remove the blot and wash 5 * 5 min with TBST buffer.*
4. *Block for 30-60 min in blocking buffer and then apply primary antibody as normal.*

Notes:

1. *Harvested proteins can be stored at -20/-80℃ till ready to use.*
2. *Precast gel concentration is selected based on the molecular weight of target protein:*

Protein Size (kDa)	Gel Percentage %
4-40	20
12-45	15
10-70	12.5
15-100	10
25-200	8

3. *Longer wash time or more washes will yield cleaner blotting bands but possibly decrease the intensity of developed bands. Optimize the procedure on demand.*
4. *If limited by samples and checking multiple proteins, membrane can be cut and incubate with different primary antibody separately.*
5. *If checking both phosphorylated and total protein on the same blot, apply the phosphorylated primary antibody first.*

Principle:

Isolation of fibroblasts from implanted scaffolds or dermis for in vitro culture.

Reagents:

- *PBS*
- *70% Ethanol*
- *Sterile blades*
- *Complete cell culture medium: DMEM supplemented with 10% FBS and 1% Anti-Anti*

Materials and Equipment:

- *6-well tissue culture plate*

Procedure:

1. *Scaffolds implanted in subcutaneous wounds (or skins from forearm) were harvested and kept in sterile PBS until ready for cell plating.*
2. *Transfer scaffolds (or skin) to sterile hood, air dry for minutes and cut into small pieces*
3. *Place 3-5 pieces in one well of 6-well plate and add drops of cell culture medium.*
4. *Incubate plates in cell culture incubator of 5% CO_2 at 37℃ until fibroblasts attached to the plate and grow out.*
5. *Remove the pieces, wash with PBS and feed cells with complete cell culture medium.*
6. *Passage fibroblasts after reaching 90% confluency.*

Notes:

1. *When first place the pieces into tissue culture plate, add minimal amount of cell culture medium to keep moisture but avoid floating of the chopped pieces.*

Principle:

Quantify collagen fibres/fibroblasts alignment directional variance to evaluate scar formation in cutaneous wound model

Materials and Equipment:

- *Thrichrome staining histological slides*
- *Olympus white light microscopy*
- *Image J (free online)*
- *Orientation J plug in (free online)*

Procedure:

1. *Take images of the thrichrome histological slides at 2x magnification.*
2. *Install OrientationJ plugin in Image J and open saved images with Image J.*
3. *Select ROI, measure pixel area and clear outside.*
4. *Change the picked picture to 32 bit image (image-type-32 bit)*
5. *Run OrientationJ Distribution: Plugin-OrientationJ-OrientationJ Distribution.*
6. *Click "Copy" and paste in excel for further analysis or remake the distribution curve.*
7. *To generate false-color coherence figures, select Hue-orientation, Saturation-coherency, and Brightness-original-image under color survey.*

Notes:

1. *Higher magnification can also be used for analysis.*
2. *In the coherence color survey, more uniform color suggested more aligned fibres.*

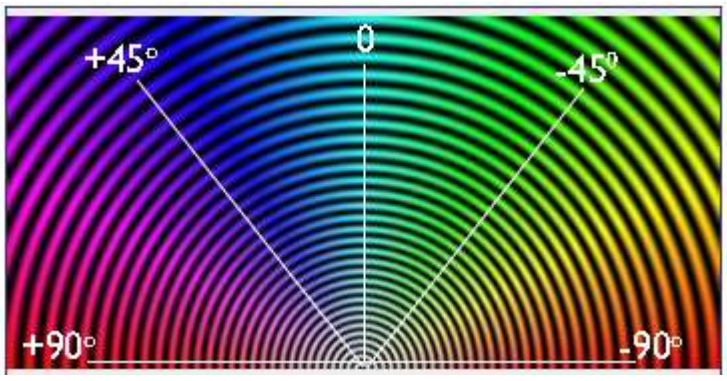


Structure Tensor
Gaussian window σ
1
[pix]
Features
Energy
Hide
Show
Orientation
Hide
Show
Coherency
Hide
Show
Color-survey
Hide
Show
Selection
Min. Coherency
70
%
Min. Energy
2
%
Mask
Hide
Show
Orientation
Hide
Show
Color-survey
Hide
Show
Distribution
Hide
Show
Color survey
Hue
Orientation
Saturation
Coherency
Brightness
Original-Image
Run
About
Terminated [1776.0ms]
Close

Principle:

Isolation of fibroblasts from implanted scaffolds or dermis for in vitro culture.

Reagents:

- *PBS*
- *NHS ester Alexafluors from Life Technologies: Donor (A-20000); Receptor (A-20002)*
- *primary antibodies (monoclonal are best, IF)*
- *Formaldehyde solution*
- *BSA*

Materials and Equipment:

- *24-well tissue culture plate*

Procedure:

1. *Label Antibodies with Fluorescent dye:*
   1) *Calculate volumes of dye and antibody needed for labeling at a ratio of 2.25 mol dye : 1 mol antibody (ug dye / concentration of dye = volume of dye neededug of antibody / concentration of antibody = volume of antibody needed)*

$$\frac{2.25 \text{ mol dye}}{1 \text{ mol Antibody}} = \frac{(\text{g/mol of dye})(2.25 \text{ mol})}{(\text{g/mol of antibody})(1 \text{ mol})} = \frac{\text{amount of dye}}{1 \text{ antibody}} \times \text{ug of antibody} = \text{ug of dye}$$

   2) *Pipette appropriate volumes of dye and antibody (calculated in step 1) into a 0.5 mL tube*
   3) *Protect samples from light and incubate at 4℃ overnight.*
2. *Immunofluorescence Staining:*
   1) *Aspirate media from cells and wash with PBS*
   2) *Make up fixation solution of 10% Formaldehyde in PBS and fix cells in 500uL fixation solution for 10-15 min at RT.*
   3) *Aspirate fixation solution and wash 3 times with PBS.*
   4) *Briefly penetrate cell membrane for 1 min with 0.1% Triton X.*
   5) *Wash cells 3x in PBS and block in 1% BSA for 1 h at RT.*
   6) *Dilute antibody (according to manufacturer's instructions) in blocking solution and incubate in dark at 4℃ overnight:*

Staining for two parallel groups: GROUP A with only donor antibody and GROUP

B with both donor and receptor antibody.

7) Aspirate antibody solution and wash 3 times with PBS

3. Read samples on the plate reader:

1) Use the fluorescence plate reader and read plates at bottom

2) Record readout from donor channel (excite: 480nm; emission: 530 nm)

4. Calculate FRET readout:

1) Take the average readout of GROUP A

2) Calculate FRET (Fluorophore units) as:

FRET=average of GROUPA – each replicate readout in GROUP B.

Notes:

What measured here is the decreased emission signal caused by energy transfer. When there is an acceptor to take the energy, the emission of donor will be decreased.